

University of Nebraska - Lincoln

DigitalCommons@University of Nebraska - Lincoln

Theses, Dissertations, and Student Research from
Electrical & Computer Engineering

Electrical & Computer Engineering, Department of

7-2012

The Role of Rare Earth Dopants in Semiconducting Host System for Spin Electronic Devices

Juan A. Colon Santana

University of Nebraska-Lincoln, juan.colon.santana@gmail.com

Follow this and additional works at: <http://digitalcommons.unl.edu/elecengtheses>



Part of the [Electronic Devices and Semiconductor Manufacturing Commons](#)

Colon Santana, Juan A., "The Role of Rare Earth Dopants in Semiconducting Host System for Spin Electronic Devices" (2012). *Theses, Dissertations, and Student Research from Electrical & Computer Engineering*. 40.

<http://digitalcommons.unl.edu/elecengtheses/40>

This Article is brought to you for free and open access by the Electrical & Computer Engineering, Department of at DigitalCommons@University of Nebraska - Lincoln. It has been accepted for inclusion in Theses, Dissertations, and Student Research from Electrical & Computer Engineering by an authorized administrator of DigitalCommons@University of Nebraska - Lincoln.

THE ROLE OF RARE EARTH DOPANTS IN SEMICONDUCTING HOST SYSTEMS
FOR SPIN ELECTRONICS DEVICES

by

Juan A. Colón Santana

A DISSERTATION

Presented to the Faculty of
The Graduate College at the University of Nebraska
In Partial Fulfillment of Requirements
For the Degree of Doctor of Philosophy

Major: Engineering
(Electrical Engineering)

Under the Supervision of Professor Jerry L. Hudgins

Lincoln, Nebraska

July, 2012

The Role of Rare Earth Dopants in Semiconducting Host System for Spin Electronic
Devices

Juan A. Colón Santana, Ph.D.

University of Nebraska, 2012

Adviser: Jerry L. Hudgins

The doping of a wide band gap insulator offers an opportunity to increase the coupling between free carriers and magnetic impurities under the magnetic polaron model, leading to an enhanced in the Curie temperature of the host compound, critical for the fabrication of devices with magnetic properties. Some rare earth elements have large intrinsic magnetic moments due to unfilled 4d orbitals, and have been readily incorporated in materials for optical applications. Here the rare earths gadolinium and cerium were explored either as dopants or as part of the high-K semiconducting compound for the fabrication of magnetic heterojunction devices with magnetic properties.

This thesis work explores the effects of rare earth gadolinium and cerium as dopants in high-K compounds such as EuO , HfO_2 and Gd_2O_3 . The thesis begins with an exemplary tale of a local moment wide band gap system (although not rare earth based), and a success in achieving negative magneto-resistance in a heterojunction structure with chromium-doped hydrogenated diamond-like carbon (Cr-DLC). In the quest for similar results, we explored the rare earth compounds by means of their electronic band structure using photoemission spectroscopy (PES) and inverse photoemission spectroscopy (IPES) to provide insight into the material functionality and applicability as an electronic device. Rectifying (diode-like) properties were observed in all the heterostructure and each heterojunction device exhibited unique properties that make them suitable for different

applications such as neutron detection or spin electronics applications. Remarkable results were observed on the EuO compound with the inclusion of 4% Gd content. The system undergoes a non-metal to metal transition as suggested by the appearance of filled electron pockets. The device properties resemble those of a tunnel junction diode, which might be related to a band bending at the interface of the film, likely due to surface overoxidation.

Acknowledgement

The outcome of this work has strongly depended upon a collective group of people, who have spent their time and trust on an individual who happens to love what he does. The following list has no order.

To God, for all the events that have led to this day. Thank you...!

To my beloved wife Olha Ketsman, who has been extremely patient and caring during the realization of this work. Thank you so much for your love, understanding and support.

To my father Juan, my sister Sheila and her husband Jose, my aunts Carmen and Maria, my grandpa Juan and my grandmother Carmen and the rest of my family. Thank you for your support from day zero and for always being there for me.

To my group members Yaroslav Ketsman, Lingmei Kong, Xin Zhang, Tao Weng, Shicao, George Peterson and Thomas Scott, who each in their own way has contributed toward my intellectual gain. To Ning Wu for his kindness and good will, for always finding the time to help me no matter how busy he was. To Keisuke Fukutani, for his great support, friendship and all the philosophical conversations that made this journey even more interesting and fruitful.

To my dear friend Shawn Langan, one of the kindest person I have ever met... thank you for all your support throughout these years and thank you for treating me like family.

To my dear friend Thomas A. George, thank you for all your support and the numerous days of Mountain Dew breaks that were accompanied by physics lessons and self-improvement hints so that I could improve my skills every day.

To Dr. Snow Balaz and Catherine Haley for all their help and attentions when I moved in.

To my friend James Glassbrener, a talented scientist who always found the time to entertain my questions, and always managed to answer them in a simple way. Thank you for everything.

To Professor Luis G. Rosa for his encouragement, time and support before and during my graduate studies. Thank you for teaching me so many valuable lessons

To Professor Nicholas Pinto for all of his help and enthusiasm regarding my graduate and undergraduate carriers.

To Professor Claudio Guerra Vela, who inspired me to go beyond by his excellent style of portraying science. You really made a difference!

To Professor Ivelisse Rubio Canabal, who took an infinite amount of her time to provide me with the necessary tools so I could succeed. Thank you so much!

To Yaroslav Lsovojy, whose great expertise in UHV system, made this work successful, you are the master of the UHV systems... you really are!

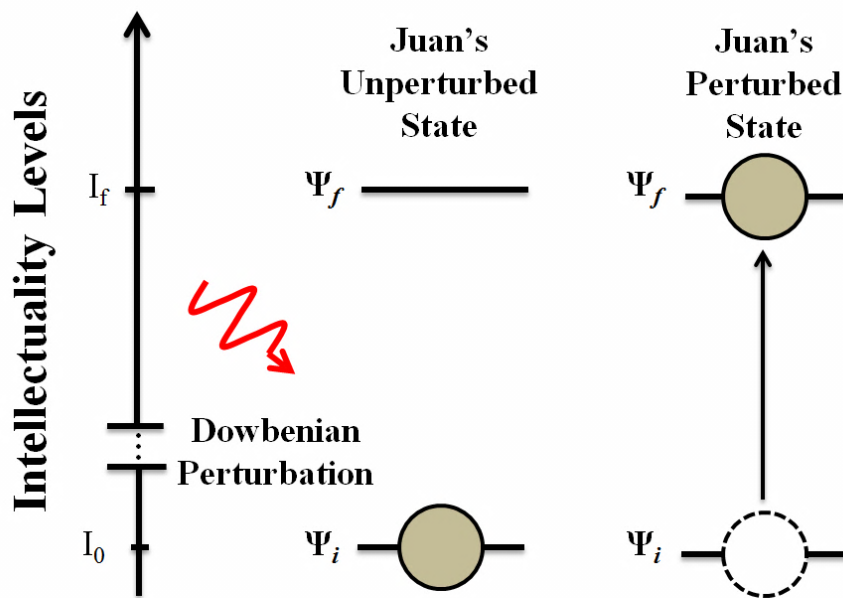
To Ihor Ketsman, for all his help and technical support in the laboratory. His devotion to detailed and careful experimentation taught me a lot.

To Professor Carolina Illie, for all her support, kindness and cheerfulness. You always had the right words, thank you for that.

To my Committee Members Profesor Natale Ianno and Professor Eva Schubert for their time invested in this work. Your interest and detailed critique improved my work.

To Jerry L. Hudgins, who have taught me the qualities of a true leader. His kindness, support and time invested in me will be forever appreciated. Thank you for always providing me with the 110%.

And last, but no least, Peter Dowben, from whom if I were to describe his incredible character, another thesis project must be written. Thank you for your unconditional trust and optimism. For extending your lessons beyond those related to science and for teaching me that I can make a difference even when sitting at my desk. Hope the following schematic summarizes your contributions at this stage of my career. Thank you so much for everything!



***Note: Ψ_f is known to describe a very stable state

Table of Contents

List of Acronyms	iv
List of Figures	vi
List of Tables	xiii

Chapter 1 Introduction

1.1 Introduction	1
1.1.1 Magnetic Semiconductors	2
References	7

Chapter 2 Experimental Techniques: The Electronic Band Structure

2.1 Photoemission Spectroscopy	10
2.1.1 Photoemission Spectroscopy as an Energy Probe Technique	10
2.1.2 The Photoemission Process	13
2.1.3 Ultraviolet Photoemission Spectroscopy (UPS)	21
2.1.4 X-ray Photoemission Spectroscopy	24
2.1.5 Resonant Photoemission Spectroscopy	22
2.1.6 Matching the Photoemission and the Theoretical Density of States.	30
2.1.7 Connection between Photoemission and Reciprocal Space	32
2.1.8 Charging Considerations in PES	36
2.2 Inverse Photoemission Spectroscopy (IPES)	38
2.3 Neutron Detectors	39
2.4 X-ray Absorption Fine Structure	44
References	50

Chapter 3 Sample preparation, Crystallographic Structure and Composition

3.1 Sample Growth Method	53
3.1.1 Hybrid plasma-assisted PVD/CVD process	53
3.1.2 Pulsed Laser Deposition	55
3.2 Crystallographic and Local Structure Studies using X-ray Absorption Fine Structure and X-ray Diffraction	58
3.2.1 The Local Structure of Amorphous Diamond like Carbon doped with Chromium	59
3.2.2 Gadolinium Occupancy in Semiconducting Hafnium Oxide	64
3.2.3 Structural Phase Transition in Gd:HfO ₂	66
3.2.4 Comparison of Gd:HfO ₂ and Gd ₂ O ₃ Monoclinic Crystal Structure.	67
3.2.5 The (111) Polar Surface in Gd:EuO	68
References	72

Chapter 4 Magnetoresistive Effects in Chromium doped Diamond-like Carbon Heterostructure

4.1 Why Study Chromium doped Diamond-like Carbon?	76
4.2 The Role of Chromium and Chromium Carbide Precipitates	77
4.3 Heterojunctions with Silicon Substrates	82
References	90

Chapter 5 Electronic Band Structure and Transport Characterization for Magnetic Dilute Semiconductors using High k Dielectric Materials

5.1 A Comparison of Gd ₂ O ₃ and HfO ₂ : Gd Electronic Band Structure	94
5.1.1 The Experimental and Theoretical Band Structure	94
5.1.2 Heterojunctions using Silicon as a p-type or n-type Substrate	106
5.2 The Effect of Rare Earth Doping (Gd and Ce) in the Electronic Band Structure of EuO Films	108

5.2.1 The Valence Band, Conduction Band and Filling of Electron Pockets	108
5.2.2 Band Bending at the EuO:Gd (111) Polar Surface	117
5.2.3 Magnetic Dependence in Heterojunction Structure	122
References	124
Chapter 6 The Local Metallicity of Gadolinium doped Compound Semiconductors	
6.1 Resonant Photoemission as a Probe for Local Metallicity	130
6.2 Resonant Photoemission in EuO films	132
6.3 Comparing the Gd 4d to 4f Photoemission Resonance for Gd in Various Host Semiconductors	138
6.4 Across the Nonmetal to Metal Transition in $Gd_{0.04}Eu_{0.96}O$	141
References	143
Chapter 7 Gadolinium Based Neutron Detectors	
7.1 Why Building Neutron Detectors?	146
7.2 Neutron Detection via Auger Electrons	146
7.3 Single Neutron Capture Detection	149
7.4 Fine Structure in the Neutron Capture Pulse Height Spectra	153
References	158
Chapter 8 Conclusions and Pending Future	
8.1 What have we learned?	161
8.2 What is Next?	163

List of Acronyms

ARPES	Angle Resolved Photoemission
BZE	Brillouin Zone Edge
CAMD	Center for Advanced Microstructures & Devices
CB	Conduction Band
CBM	Conduction Band Minimum
CIS	Constant Initial State Spectroscopy
CVD	Chemical Vapor Deposition
DFT	Density Functional Theory
DLC	Diamond-like Carbon
DMO	Dilute Magnetic Oxides
DMS	Dilute Magnetic Semiconductor
DOS	Density of States
EXAFS	Extended x-ray Absorption Fine Structure
FCC	Face Centered Cubic
FM	Ferromagnetic
FL	Fermi Level
FT	Fourier Transform
GMR	Giant Magneto Resistance
IPES	Inverse photoemission Spectroscopy
MBE	Molecular Beam Epitaxy
NIM	Normal Incidence Monochromator
PES	Photoemission Electron Spectroscopy

PLD	Pulsed Laser Deposition
PVD	Physical Vapor Deposition
RPES	Resonant Photoemission Spectroscopy
TGM	Toroidal Grating Monochromator
UHV	Ultra High Vacuum
UPS	Ultraviolet Photoemission
VB	Valence Band
VBM	Valence Band Maximum
VUV	Vacuum Ultraviolet
XAFS	X-ray Absorption Fine Structure
XANE	X-ray Absorption near Edge Structure.
XAS	X-ray Absorption
XPS	X-ray Photoemission
XRD	X-ray Diffraction

List of Figures

- Figure 1.1.1** A two-dimensional lattice for (a) an undoped nonmagnetic semiconductor crystal, and a dilute magnetic semiconductor with a random distribution of magnetic dopants ions in the lattice with (b) a paramagnetic behavior and (c) a ferromagnetic coupling due to the introduction of donor defects. The dashed circle represents the Bohr radius of the electron due to the defect 2
- Figure 1.1.2** Schematic of the physical geometry from which the GMR is observed along with a R vs B plot showing the effect of the magnetic field on the resistance of the structure 4
- Figure 2.1.1** Schematic of a perturbed system due to an electromagnetic wave from the point of view of energy levels 11
- Figure 2.1.2** The main elements of the photoemission process. The picture representing the light source is a dual anode x-ray lamp and the detector is a hemispherical angle resolved electron analyzer, both elements are inside a ultra-high vacuum chamber as denoted by the dashed lines 18
- Figure 2.1.3** (a) The ultra-high vacuum chamber employed for the PES process at the spectroscopy laboratory in the University of Nebraska and the geometrical set up of the PES elements both (b) into and (c) out of the chamber 20
- Figure 2.1.4** Picture of the ultraviolet source employed in our studies. Taken from the Thermo Electron Corporation website 21
- Figure 2.1.5** A typical valence band spectra obtain from UPS. The dashed line indicates the secondary electron tail and is due to inelastic scattering of the electrons before reaching the analyzer. Subsequent steps are shown on the top right portion of the figure 22
- Figure 2.1.6** Energy level diagram describing the ultraviolet photoemission process ... 23
- Figure 2.1.7** Energy level diagram describing the X-ray photoemission process 24
- Figure 2.1.8** (a) The physical geometry of the X-rays source and (b) a schematic of the of the X-ray source. Figure (a) was taken from the Thermo Scientifics application note 31057 25
- Figure 2.1.9** A (a) schematic and (b) picture of the storage ring in CAMD 27
- Figure 2.1.10** (a) The 3m TGM beamline and (b) a picture of the TGM 28
- Figure 2.1.11** (a) The UHV chamber used for the high resolution angle resolved photoemission spectroscopy and (b) the resonant photoemission experiments 29

Figure 2.1.12 The relation between the density of state from a (a) theoretical and (b) experimental point of view. (c) The reference energy between the two DOS distribution	31
Figure 2.1.13 Schematic of the electron propagation along the solid vacuum interface	33
Figure 2.1.14 (a) The first Brillouin zone for a face centered cubic (FCC) lattice and (b) the wavevectors along the direction perpendicular to the surface of a film and the wavevector along the direction parallel to the surface of the film	36
Figure 2.2.1 Energy level diagram summarizing the IPES process	38
Figure 2.2.2 Schematic of the inverse photoemission process	39
Figure 2.3.1. A schematic showing (a) the p-n junction geometry and (b) the depletion region and neutral region of a diode	40
Figure 2.3.2. A p-n junction diode in (a) forward and (b) reverse bias operation	40
Figure 2.3.3 The neutron detection mechanism for a diode detector. The neutrons are incident into a moderator (usually a hydrocarbon plastic) to slow them down. Cadmium foil is used to test for Gamma sensibility although a thin foil of lead is sometime used	42
Figure 2.3.4 Single-chip pulse counting and binning electronics block diagram. The design occupies a total silicon area of 10mm ² fabricated in a 0.35 μ m CMOS technology (see text). The charge sensitive amplifier (CSA) and analog-to-digital converter (ADC) are indicated schematically	43
Figure 2.4.1 A hypothetical x-ray absorption spectra	45
Figure 2.4.2 Schematic of x-ray absorption in terms of an energy diagram and the absorption probability spectra for the case where (a) there are no neighbors and (b) the photo-electron can scatter from a neighboring atom.	47
Figure 2.4.3 Schematics of experimental setup for XAFS measurement in fluorescence mode from CAMD	48
Figure 3.1.1 Survey of vacuum deposition techniques	54
Figure 3.1.2 (a) Schematic of the pulsed laser deposition process and (b) geometrical set up inside the UHV chamber	56
Figure 3.2.1 The X-ray absorption near-edge structure (XANES) spectra for the Cr-DLC films along with pure Cr and Cr carbide (Cr ₃ C ₂). The spectra are normalized and translated along the y-axis (intensity) for clarity	62

Figure 3.2.2 The Fourier transform of the extended X-ray absorption fine structure spectra (EXAFS) for the Cr-DLC films along with pure Cr carbide (Cr_3C_2). The spectra are translated along the y-axis (intensity) for clarity 63

Figure 3.2.3 (a) The $k\chi(k)$ of 3% Gd doped HfO_2 extracted from the Gd L_3 -edge EXAFS spectra 65

Figure 3.2.4. The Fourier transform (FT) of 3% Gd-doped HfO_2 EXAFS data. The oscillating curve (dashed lines) is the imaginary part of the Fourier transform of the data. The envelope (solid lines) are the magnitudes of the Fourier transform. The 3% data are transformed with a square window between 2.8 and 9.4 \AA^{-1} . The peak assignment is based on HfO_2 65

Figure 3.2.5 Part of the XRD pattern for 3%, 10%, and 15% Gd doped HfO_2 . The 3% Gd doped films are consistent with that of the HfO_2 in a simple monoclinic structure. The 10% doped samples are mixed monoclinic and majority cubic phases, as indicated, while 15% Gd-doped samples are in a fluorite phase. In the fluorite fcc phase, the lattice constant increases with increased Gd doping 66

Figure 3.2.6 (a) Part of the XRD pattern of the film is shown in figure. X-ray diffraction patterns of PLD grown Gd_2O_3 (upper panel) and 3% Gd doped HfO_2 (lower panel). The bar diagrams included in each panel are the standards of monoclinic Gd_2O_3 and HfO_2 , respectively. For 3% Gd doped HfO_2 (lower panel), the XRD is consistent with that of HfO_2 in a simple monoclinic structure. (b) Structure of Gd_2O_3 , with the packing of the ions in Gd_2O_3 as viewed along the b -axis. The green and red spheres represent gadolinium and oxygen atoms respectively. The Gd .. Gd interactions are not shown 68

Figure 3.2.7 X-ray-diffraction pattern for PLD-grown (a) EuO , (b) Gd-doped EuO films on $\text{Si}(100)$ and (c) Ce:EuO 69

Figure 4.2.1 Cr_3C_2 precipitates only at high doping levels, with the precipitates at higher concentration at the interfaces 78

Figure 4.2.2 Photoemission from a 25% chromium doped DLC film (*black*) deposited on silicon, compared to undoped DLC film (*red*). The photon energy was 70 eV and the photoelectrons were collected along the surface normal 79

Figure 4.2.3 The photoemission spectra of the 11.0 % Cr-doped DLC film on silicon as a function of photon energy. The photoelectrons were collected along the surface normal 80

Figure 4.2.4 Hysteresis loops and virgin magnetization curves of Cr-DLC with 3 % Cr at (a) 20 Kelvins and (b) 10 Kelvins 81

Figure 4.3.1 The I–V curves from Cr-DLC films in a heterojunction with n-type silicon, as a function of temperature, for different chromium doping levels (a) 5.0 %, (b) 11.0 %, (c) 15 % and (d) 20 % 83

Figure 4.3.2 The I–V curves from the 11 % Cr (a) and 15 % Cr (b) Cr-DLC film to n-type silicon heterojunction devices with changing applied magnetic field. The change in forward current, as a function of the magnetic field, for Cr-DLC film to n-type silicon heterojunction devices at 11.0 % Cr (c), and 15.0 % Cr (d). Forward bias voltage was 2.0 V in panels (c) and (d). All data were acquired at room temperature. In the first trial (blue) negative magnetoresistance was observed, but in subsequent trials (red) little or no magnetoresistance was found without application of a large field 84

Figure 4.3.3 The I–V curves from a 11 % Cr Cr-DLC film to n-type silicon heterojunction device after magnetization of the sample in a field of 1.0 T. The increase of the negative magnetoresistance is quite evident, and plotted in the *inset* for 2 V forward bias 85

Figure 4.3.4 The resistance of the 11% Cr-doped DLC/silicon heterojunction diode is dependent on voltage in the reverse bias, as indicated in model calculations. The forward bias does not have the same dependence, because the function $R(H)$ is constant with $V > 0$. The schematic is the ideal of the effective circuit for the model calculations 86

Figure 4.3.5 In the forward bias, in simple model calculations, the resistance of the 11% Cr-doped DLC/silicon heterojunction diode decreases as the applied magnetic field increases 89

Figure 5.1.1 Different bands intensities for pristine and Gd-doped films of HfO₂. The photon energy used was 100 eV and the light incidence angle is 45°. All photoelectrons were collected along the surface normal at $T = 320$ °C 95

Figure 5.1.2 The photoemission spectrum of the valence band Gd₂O₃ $\langle \bar{4}02 \rangle$. The various components contributing to the valence band structure are indicated and major contributions to the photoemission features indicated. The photon energy is 117 eV and the light incidence angle is 45°. All photoelectrons were collected along the surface normal at $T = 240$ °C 96

Figure 5.1.3 Resonant photoemission spectra for photon energies through the 4d → 4f resonance for Gd doped films of HfO₂. Light incidence angle is 45°. All photoelectrons were collected along the surface normal 97

Figure 5.1.4 The resonant photoemission spectra for photon energies through the 4d → 4f resonance for Gd₂O₃. Light incidence angle is 45°. All photoelectrons were collected along the surface normal 98

Figure 5.1.5 The resonant photoemission intensities through the $4d \rightarrow 4f$ resonance for Gd_2O_3 (a) and Gd doped films of HfO_2 (b). For Gd_2O_3 , there are seen to be two Gd 4f components at a binding energy of about 8.7–9.5 eV below the Fermi level and the ‘shoulder’ at a binding energy of 11–12 eV, which are assigned as bulk (*black*) and surface (*red*) components respectively 99

Figure 5.1.6. The calculated density of states for monoclinic (type B) Gd_2O_3 . The monoclinic Gd_2O_3 density of states (DOS) has been broadened with a Gaussian width 0.2 eV. The total density of states has been projected onto each atomic species (gadolinium and oxygen) showing the strong Gd 4f character at the DOS peak around $E = -6.3$ eV and the major oxygen 2p character hybridized with Gd 5d orbitals over the energy range of -5 to 0 eV 102

Figure 5.1.7 The dispersion of the Gd 4f component, with changing photon energy. The critical points are indicated, assuming no inner potential and the predicted lattice spacing of 23.7 \AA along $\langle \bar{4}02 \rangle$ 104

Figure 5.1.8 A heterojunction diode constructed from Gd-doped HfO_2 on silicon, for various Gd-doping concentrations. With oxygen vacancies, the Gd doping generated acceptor states, in 3% Gd-doped HfO_2 , are over compensated and doped hafnium oxide forms a rectifying diode on *p*-type silicon (a). The 10% Gd-doped HfO_2 is not overcompensated by oxygen vacancies and does not form a rectifying diode on *p*-type silicon (b) but does do so on *n*-type silicon (c) 107

Figure 5.2.1. The simulated (solid line) and experimental (dashed line) photoemission spectra for undoped EuO, with corrections for the combined excited-state density of states. The DFT/GGA calculations of density of states (DOS) were performed with fixed occupancies for treating the excited states 109

Figure 5.2.2 Combined ARPES and IPES spectra for (a) undoped EuO film, (b) $\text{Eu}_{0.96}\text{Gd}_{0.04}\text{O}$ (111) film, and (c) same as (b) but after sputtering. A photon energy of 60 eV was used, with light incident at 45° and photoelectrons collected along the surface normal. For the IPES spectra the electrons are incident along the surface normal 113

Figure 5.2.3 The photoemission spectra obtained for $\text{Eu}_{0.96}\text{Gd}_{0.04}\text{O}$ (111) films as a function of the photon energy. The angle of incidence was 45° and all photoelectrons were collected along the surface normal at $T = 300 \text{ K}$ 115

Figure 5.2.4 (a) The Fermi level intensity (*blue*) plotted as a function of k_\perp , along the [111] direction. (b) The dispersion of the Eu 4f weighted band at the valence-band maximum, along the (111) direction or wave vector normal to the surface, k_\perp . Both results were extracted from the photon energy dependent ARPES spectra. BZE indicates the Brillouin-zone edge. The intensity of the Eu 4f weighted band (+), at the valence-band maximum, along the k_\perp (111) direction, is also plotted in (a) 115

Figure 5.2.5 The Fermi-level intensity plotted as a function of the parallel momentum k_{\parallel} along the ΓM direction, for photon energies of (a) 40 eV and (b) 25 eV. For k_{\parallel} along the ΓM direction, the relative intensity has been also plotted 300–400 meV below the Fermi level (green) and at the Fermi level (red), to illustrate the roughly parabolic shape of the electron pocket about the surface Brillouin-zone edge at 40 eV 117

Figure 5.2.6 Calculated structure of the O-terminated EuO(111) surface. Only half of the slab is shown, the other half being symmetric. For interlayer spacings see Table 5.2.1. In the figure, large spheres are Eu atoms; small spheres: O atoms..... 120

Figure 5.2.7 Site-projected DOS for all Eu and O atoms of the 27-monolayer slab of Gd-doped-EuO with (111) surfaces. A model with empirical adjustments is used (see text). (a) Eu site-projected DOS where the unoccupied DOS is multiplied by 5 (as indicated). (b) O site-projected DOS; unoccupied DOS is multiplied by 10 (as indicated). The numbering of the sites starts at the surface 121

Figure 5.2.8 I - V curves for (a) undoped EuO(100) film as a function of temperature, (b) $\text{Eu}_{0.96}\text{Gd}_{0.04}\text{O}$ (111) film at room temperature. The curve marked (i) is for zero field; the curve marked (ii) is for an external magnetic field of 1000 Oe 123

Figure 6.2.1 Valence band spectra obtained from the photoemission density of state for (a) EuO and (b) $\text{Eu}_{0.96}\text{Gd}_{0.04}\text{O}$ films grown on p-type Si (100). The composition of the spectra was determined by the Gaussian distributions and the photoemission feature were classified as arising from largely the (A) Eu $4d_{5/2}$ and electron pockets of the conduction band minimum, (B) Eu $4d_{3/2}$ (C) O 2s, (D) O 2s and (E) Gd 4f and Eu 4f final state (satellite) contributions. Photoelectrons were collected along the surface normal. Measurements for both films were taken using synchrotron light with photon energy of 60 eV and incidence angle of 45° . Binding energy is denoted in terms of $E-E_F$ 133

Figure 6.2.2 (a) The photoemission spectra for photon energies through the Gd and Eu 4d to 4f super koster Kronig photoemission resonance for $\text{Eu}_{0.96}\text{Gd}_{0.04}\text{O}$ films. (b) The resonant photoemission intensities, as a function of photon energy i.e. constant initial state spectra, for the valence feature at (i) 0.5 eV, (ii) 2.3 eV, (iii) 6.1 eV and (iv) 9.2 eV below the Fermi level. Light was incident at 45° . Photoelectrons were collected along the surface normal. Binding energy is denoted in terms of $E-E_F$ 135

Figure 6.3.1 Valence band photoemission spectra “on” (photon energy of 147 eV) and “off” (photon energy of “off” with $h\nu = 140, 139.7$ and 132 eV for $\text{Eu}_{0.96}\text{Gd}_{0.04}\text{O}$, $\text{Gd}_{0.03}\text{Ga}_{0.97}\text{N}$, $\text{Gd}_{0.03}\text{Hf}_{0.97}\text{O}_2$ respectively) the Gd 4d to 4f resonant photoemission feature obtained for (a) $\text{Eu}_{0.96}\text{Gd}_{0.04}\text{O}$, (b) $\text{Gd}_{0.03}\text{Ga}_{0.97}\text{N}$ and (c) $\text{Gd}_{0.03}\text{Hf}_{0.97}\text{O}_2$. All photoelectrons were collected along the normal to the film surface. Binding energy is denoted in terms of $E-E_F$ 139

Figure 6.3.2 Constant initial state valence intensity as a function of photon energy in the region of Gd 4f contributions to the valence band (-9 eV binding energy, $E-E_F$) in Gd doped (a) GaN (3%), (b) HfO_2 (3%) and (c) EuO (4%) host systems 141

Figure 6.4.1 Resonant photoemission intensity as a function of photon energy for the Eu 4f weighted features in the valence band at about -2 eV binding energy ($E-E_F$) in (a) EuO and (b) $\text{Eu}_{0.96}\text{Gd}_{0.04}\text{O}$ films. The decrease in intensity suggests a major change in metallicity with the inclusion of 4% percent Gd 141

Figure 7.2.1. A summary of the major decay routes for ^{158}Gd in the excited state through emission of high energy gamma rays, low-energy gamma rays, x-rays, internal (IC) and Auger Coster–Kronig (ACK) conversion electrons as $^{157}\text{Gd}(n,\gamma) \rightarrow 158\text{Gd} + \gamma + \text{x-rays} + \text{IC } e^- + \text{ACK } e^-$ 148

Figure 7.3.1 A heterojunction diodes constructed from $\text{Hf}_{0.85}\text{Gd}_{0.15}\text{O}_{1.92}$ on n-type silicon. The $\text{Hf}_{0.85}\text{Gd}_{0.15}\text{O}_{1.92}$ is not overcompensated by oxygen vacancies and does not form a rectifying diode on p-type silicon but does do so on n-type silicon 150

Figure 7.3.2 Pulse height spectra obtained using $\text{Hf}_{1-x}\text{Gd}_x\text{O}_{2-0.5x}$ combined contributions of Gd–O, and Gd–Hf single-scattering paths as well as several multiple-scattering (+MS) paths 151

Figure 7.3.3. The pulse height spectra of $\text{Hf}_{0.85}\text{Gd}_{0.15}\text{O}_{1.92}$ on n-type Si(100) samples with thermalized neutrons from a PuBe source with a flux of 600 neutrons s^{-1} incident on the diode, compared with an MCNP 5.0 simulation, modified to account for suppression of the pulses of pulse height less than 200 mV in experiment 152

Figure 7.4.1. A sampling of a time domain pulse height spectra using $\text{Hf}_{0.85}\text{Gd}_{0.15}\text{O}_{1.92}$ on n-type Si(100) samples irradiated with thermalized neutron from a PuBe with a flux of 600 neutrons $\text{cm}^{-2}\text{s}^{-1}$. The offset of the baseline from 0 V is not meaningful, and a consequence of the display routine 156

List of Tables

Table 3.2.1 Structural parameters for Cr-DLCs and Cr ₃ C ₂ obtained from curve fitting Sample Model fit	64
Table 5.2.1 The interlayer spacing calculated for EuO(111) as indicated in Figure 5.2.6 . The layer spacings are oscillatory in the region of the surface, as indicated. The layers spacing are giving in units of Å	120
Table 6.3.1. Summary the photon energy for resonant photoemission intensity maximum, the width of the Gd 4d to 4f photoemission resonance, in photon energy and the intensity ration of “on” resonance at a photon energy of 147 eV to the “off” resonant intensity at a photon energy of eV	140

Chapter 1 Introduction

This thesis explores how the inclusion of a small percent of magnetic impurity affects the magnetization properties and electronic band structure of a set of different host semiconducting compound materials. Much of the emphasis will be on gadolinium which we employed, both as a dopant and as a member of the compound itself, given its valuable intrinsic properties (particularly the large magnetic moment of $7.3 \mu_B$ per atom). Key questions towards the ensemble of this work are: Can we make heterojunction devices out of these materials? If we do fabricate devices, do they exhibit magnetic dependence? What is the role of gadolinium in highly correlated semiconductor systems, given the large on-site energy due to the half-filled 4f orbital ($4f^7$).

In fact addressing the latest question is quite complex. Gadolinium is usually treated as having a stable 3+ valence state when inserted into host semiconductors. The electrons in the 4f orbitals remain fairly localized to the ion vicinity, likely due to the partial screening provided from the outermost closed subshells. This leads to the situation in which the electrons with the lowest energy does not correspond to the outermost shell of the atom, but a shell located underneath, hence, the 4f electrons are somewhat restricted from interacting directly with the neighbor atoms surrounding the ion. Yet, we found that the effect of increasing the gadolinium concentration is very different in each particular semiconductor. In most cases, the 4f electrons form part of the valence band and directly contribute to strong hybridization between the ion and neighboring atoms.

Nonetheless, before diving into the complexity of these issues, let's not deviate from our major goal (i.e. devices with magnetic properties). On this behalf, let's point out the road that led to the foundations of this work from a historical point of view.

1.1 Magnetic Semiconductors

A magnetic semiconductor is a material that exhibit both, ferromagnetic behavior and semiconducting properties simultaneously. Ferromagnetism refers to a material with the ability to remain magnetized after the application of an external magnetic field and a semiconductor is a material with a small electronic band gap and the ability to partly conduce current. In contrast, a dilute magnetic semiconductor (DMS) refers to the same type of material with the difference that is doped with atoms that possess an intrinsic magnetic moment (such as Gd). The idea behind these devices relies on increasing the Curie temperatures of our compounds via the interaction of magnetic impurities and free carriers form via defect in the compound structure as shown in [Figure 1.1.1](#).

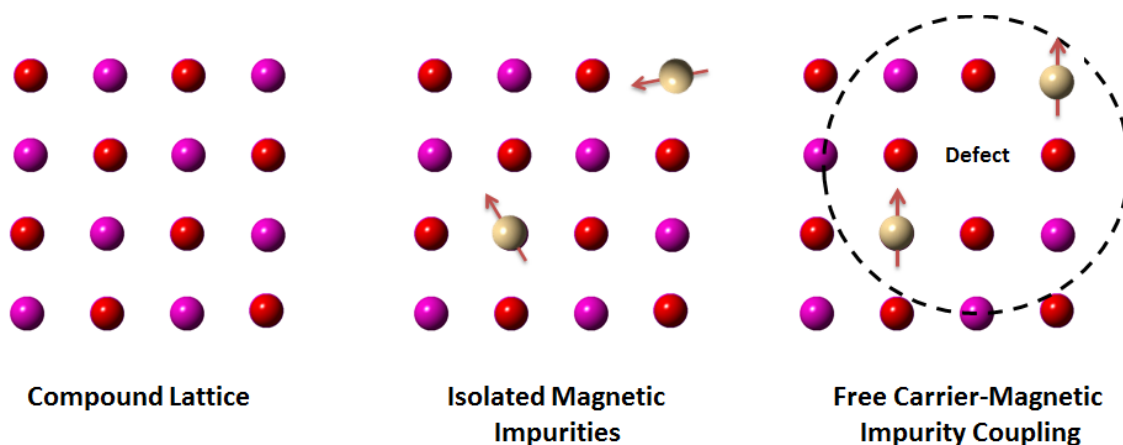


Figure 1.1.1 A two-dimensional lattice for (a) an undoped nonmagnetic semiconductor crystal, and a dilute magnetic semiconductor with a random distribution of magnetic dopants ions in the lattice with (b) a paramagnetic behavior and (c) a ferromagnetic coupling due to the introduction of donor defects. The dashed circle represents the Bohr radius of the electron due to the defect.

As simple as the concept behind DMS materials sounds, it turns out that the physics of these materials is fairly complex. To understand their true value we must gain insight on the importance of DMSs. To this end, a brief history of spintronics research must be reviewed. The portmanteau “spintronics” is a combination of both spin (an intrinsic property of electrons) and electronics (field concerned with circuitry design). The name fits quite well to this technology as it exploits the spin of the electron in addition to the electron charge as seen in conventional devices such as diodes and transistors. In 2007, Albert Fert and Peter Grønberg won the Nobel Prize in physics for their independent work in the discovery of the giant magnetoresistance (GMR) back in 1988 [1, 2], an event which some considered as the birth of spintronics. The GMR effect is observed when two metallic ferromagnetic layers are separated by a nonmagnetic material (usually a few nm thick). Depending on the net magnetization of the two ferromagnetic materials the electrical resistance will change as shown in [Figure 1.1.2](#). For parallel alignment the resistance is low whether for antiparallel alignment the resistance is high.

This phenomenon has led to applications such as read heads for modern hard drives, magnetic sensors and tunnel magnetoresistance. There are several reviews of GMR [3] and spintronics applications [4-6] available, with a more detailed description of this field and the application mentioned above. For the purpose of this work it suffice to understand that a magnetic field can influence the resistance of a material, and hence the current through it.

Unfortunately, there is a downside with all the applications mentioned above as their implementation is limited to the use of ferromagnetic metals. Ferromagnetic materials are not susceptible to an applied electric field, resulting in difficulties if one

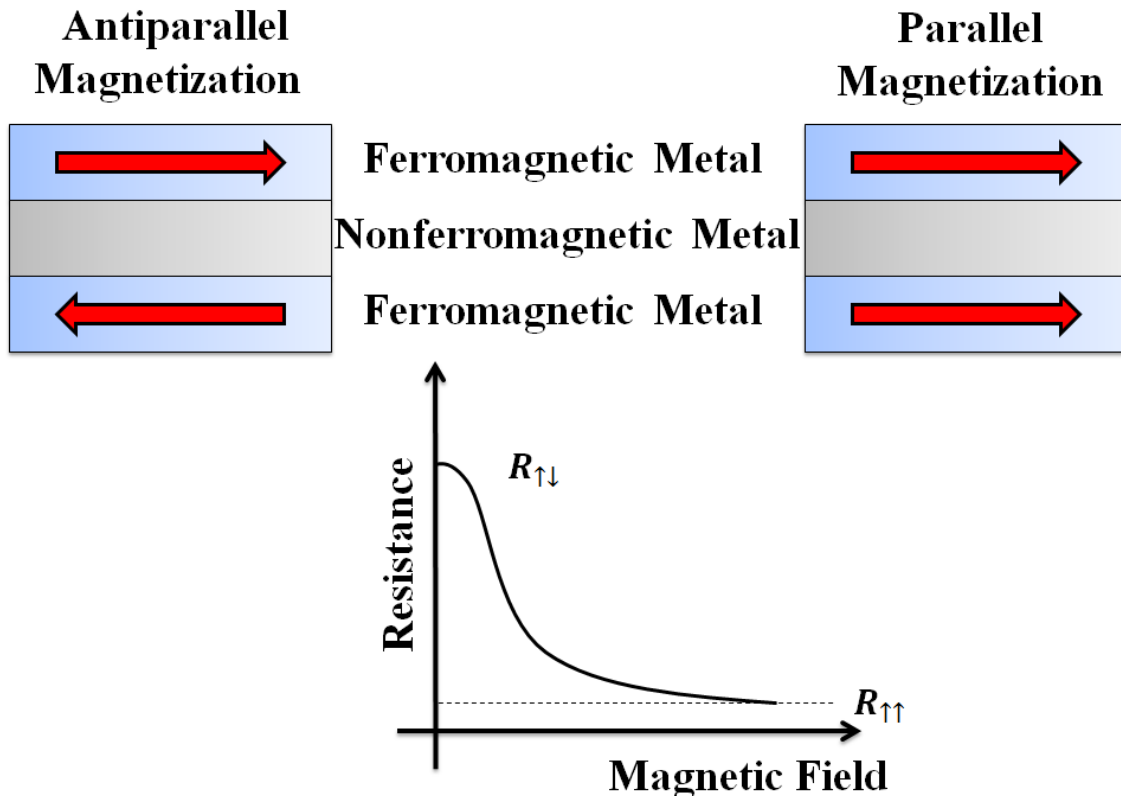


Figure 1.1.2 Schematic of the physical geometry from which the GMR is observed along with a R vs B plot showing the effect of the magnetic field on the resistance of the device structure.

wants to exploit the charge of the carrier. Semiconductor materials are much more sensitive to electric field dependence [7] and are indeed one of the reasons for many dilute magnetic semiconductor (DMS) studies. Imagine a world in which you can merge the current semiconducting technology with magnetism (memory) in a single material... great things will come from it! The first DMS studies were performed in the late 70's

and were heavily considered in the 80's. Among these, II-IV and III-V based DMSs such as (Zn, Mn)Se and (Ga, Mn)As were popular. Special efforts were invested in (Ga, Mn)As [8] and (In, Mn)As [9] as ferromagnetic order was achieved by Hideo Ohno's and co-workers with a Curie temperature of 140 K at the time [8], although T_C of 180 K were later achieved by careful growth of the material. In 2000, Dietl's [10] came up with a model (based on that by Zener [11]) to explain the ferromagnetic behavior in these materials and triggered a search for room temperature magnetism. This model does provide good insights in the description of the experimental data, but some fundamental aspects of these complex materials are still controversial. There is still an ongoing debate as whether or not one can identify an impurity band in materials with high T_C and whether the charge transport and magnetic interaction are mediated by localized or extended states, as these states are close to the Fermi level. High doping concentrations result in a wider impurity band and can lead to a mixing with the valence band [12].

There is another type of potential ferromagnetic semiconductor material, the dilute magnetic oxides (DMOs) which are more pertinent to this work. Perhaps, the most popular model today is that proposed by Coey [13] in which ferromagnetic exchange is mediated by shallow donor electrons that form bound magnetic polarons. If overlap of these occurs, a spin-split impurity band can be created. Since the carriers are expected to couple strongly to the magnetic moments, DMOs might be a route for interesting spintronics applications. Ferromagnetism above room temperature has been reported, but the results are irreproducible and observed only in non-crystal films (and bulk material), in which case, the effects can be attributable to magnetic secondary phases. This opens up

a more philosophical question regarding the definition of a DMOs material [14], despite of how the material is define, we show here that interesting spintronics applications are indeed possible.

It must be noted that these materials are still in the testing phase and one should see them as a source for new and interesting physics, as device implementation is by no means routine at this stage. Even though the word “application” is commonly and repetitively used, only few devices are clearly possible at least with functionalities at room temperature. In order to reach more applications, a better understanding of the physics must be attained first.

As a closing note and although not the core topic of this thesis work, the implementation of gadolinium on our compounds might lead to interesting applications unrelated to magnetism or magnetic properties. Neutron detection applications may be possible due to the gadolinium high neutron capture cross section. This is indeed promising as there is now a large demand and an increase in usage of radiation detection technologies for applications in homeland security, nonproliferation, and national defense. This concept was put to test with a Gd:HfO₂ films on Si(100) heterostructures in which a successful pulsed height spectra was obtained as shown later in this work.

References

- [1] G. Binasch, P. Grunberg, F. Saurenbach and W. Zinn, “Enhanced magnetoresistance in layered magnetic structures with antiferromagnetic interlayer exchange”, *Phys. Rev. B* 39, 4828–4830 (1989)
- [2] M.N. Baibich, J.M. Broto, A. Fert, F. Van Dau, F. Nguyen, F. Petroff, P. Etienne, G. Creuzet, A. Friederich and J. Chazelas, “Giant Magnetoresistance of (001)Fe/(001)Cr Magnetic Superlattices”, *Phys. Rev. Lett.* 61, 2472–2475 (1988)
- [3] E.Y. Tsymbal, D.G. Pettifor, “Perspectives of giant magnetoresistance”, *Solid State Physics*, Academic Press, 2001, Volume 56, Pages 113-237, ISSN 0081-1947, ISBN 9780126077568
- [4] S. A. Wolf, D. D. Awschalom, R. A. Buhrman, J. M. Daughton, S. von Molnár, M. L. Roukes, A. Y. Chtchelkanova, and D. M. Treger, “Spintronics: A Spin-Based Electronics Vision for the Future”, *Science* 16 November 2001: 294
- [5] Igor Zutic, Jaroslav Fabian and S. Das Sarma, “Spintronics: Fundamentals and applications”, *Rev. Mod. Phys.* 76, 323–410 (2004)
- [6] S.J. Pearton, C.R. Abernathy, D.P. Norton, A.F. Hebard, Y.D. Park, L.A. Boatner, J.D. Budai, “Advances in wide bandgap materials for semiconductor Spintronics”, *Materials Science and Engineering R* 40 (2003) 137–168
- [7] Z. Wilamowski and A. M. Werpachowska, “Spintronics in semiconductors”, *Materials Science-Poland*, Vol. 24, No. 3, 2006
- [8] H. Ohno, A. Shen, F. Matsukura, A. Oiwa, A. Endo, S. Katsumoto, and Y. Iye, “(Ga,Mn)As: A new diluted magnetic semiconductor based on GaAs”, *Appl. Phys. Lett.* **69**, 363 (1996)
- [9] Ohno, H. and Munekata, H. and Penney, T. and von Moln'ar, S. and Chang, L. L., “Magnetotransport properties p -type (In,Mn)As diluted magnetic III-V semiconductors”, *Phys. Rev. Lett.* 68, 2664–2667 (1992)
- [10] T. Dietl, H. Ohno, F. Matsukura, J. Cibert and D. Ferrand, “Zener Model Description of Ferromagnetism in Zinc-Blende Magnetic Semiconductors”, *Science* 11 February 2000: 287 (5455), 1019-1022.
- [11] C. Zener, “Interaction between the d Shells in the Transition Metals”, *Phys. Rev.* 81, 440 (1950)

- [12] Krstaji, P. M., Peeters, F. M. and Ivanov, V. A. and Fleurov, V. and Kikoin, K., “Double-exchange mechanisms for Mn-doped III-V ferromagnetic semiconductors”, *Phys. Rev. B* 70, 195215 (2004)
- [13] J.M.D. Coey, M. Venkatesan & C.B. Fitzgerald, “Donor impurity band exchange in dilute ferromagnetic oxides”, *Nature Materials* 4, 173 - 179 (2005)
- [14] J.M.D. Coey and S.A. Chambers, “Oxide Dilute Magnetic Semiconductors—Fact or Fiction?”, *MRS Bulletin*, 33, pp 1053-1058 (2008)

Chapter 2

Experimental Techniques

“It doesn't matter how beautiful your theory is, it doesn't matter how smart you are. If it doesn't agree with experiment, it's wrong”

-Richard P. Feynman -

At the beginning of this work we undertook to the quest of constructing devices with magnetic properties. But in order to construct heterojunction devices one must be very cautious of the quality of the films that are implemented, as the quality factors are correlated to the electronic properties of the materials. This chapter seeks to introduce the experimental techniques adopted throughout this study to characterize the crystallographic structure of the materials and their electronic properties. Most of the emphasis will be on photoemission spectroscopy, as this method provides a more comprehensive insight regarding the electronic band structures of solid materials, which we consider key in the development of this work.

2.1 Photoemission Spectroscopy

Photoemission (also known as photoelectron) spectroscopy (PES) refers to the process in which an electron is removed from a solid material after the absorption of a photon. The first evidence of this phenomenon dates back to 1887 where Heinrich Hertz detect electrons emitted from a secondary arc due to irradiation of ultra violet light [1]. It was not until 1905 that Einstein offered an explanation of this effect [2], which is now referred to as “the photoelectric effect”. This is as far as I go regarding the history of photoemission spectroscopy. For a historical perspective regarding PES, the papers written by Bonzel (et al.) and Reitner (et al.) are strongly recommended [3, 4]. For better understanding of the content offered throughout this work, I rather focus on the analytical part of the PES process and how to connect it to the electronic structure of a material.

2.1.1 Photoemission Spectroscopy as an Energy Probe Technique

On this modern age, if ones feel the urge to “probe” the location of an individual, one only needs to call to their cellphone and ask “where are you?” This process will automatically give the location of the individual by exploiting “a property” that the individual had... a cellphone. If ones want to know the height of a tall building, just place a meter stick (or any long object) next to the building and perpendicular to the floor and measure its height and the length of the shadow it casts on the floor. Then, measure the length of the shadow cast by the building and you are set to go. Due to a geometrical condition called similarity, one can determine the height of the building using the recorded parameter. In the atomic level there is no difference and one must exploit the

atomic properties of the particles in order to gain information regard it. In the case of the photoemission process, we can exploit our knowledge of the kinetic energy of the electron (a “property “the electron have by just being in motion with some speed) at the moment is detected, then by conservation of energy (see equation 2.1.5) one can gain information from which orbital the electron came from when it was inside the sample.

Let’s use the following example to validate my claim and as an attempt to capture the essence of the PES process. Imagine that an electron is in an initial state described by the wavefunction ψ_i and with energy E_i . Suddenly, the atom absorb a photon of energy $h\nu$ and the electron undergo a transition from that initial state into a final state described by a wavefunction ψ_f with energy E_f as shown in [Figure 2.1.1](#).

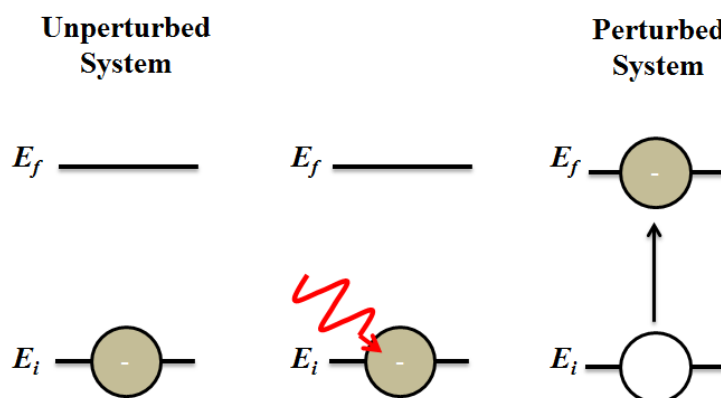


Figure 2.1.1 Schematic of a perturbed system due to an electromagnetic wave from the point of view of energy levels.

Throughout this process energy must be conserve providing us with the expression

$$h\nu = E_f - E_i \quad (2.1.1)$$

which means that the energy of an electron in the final state is the same as the energy the electron had in the initial state plus the energy provided by the photon. If we assume that the electron can have different final states, each with certain probability but all with the same energy E_f (generally called degenerate states), we can represent the final state of the electron as an expansion in terms of its eigenstates as

$$\psi_f = \sum_n c_n \psi_n \quad (2.1.2)$$

where c_n can be thought as a probability coefficient (when taking the modulus square) and ψ_n as the wavefunction describing a specific final state. Under this assumption we can assign an eigen energy E_n to each eigenstate ψ_n . This will allow us to write the degenerate final state energy as

$$E_f = E_n + E_K \quad (2.1.3)$$

where E_n is the energy of the electron by just being in the n state (or orbital energy in the case of a real solid) and E_K is the kinetic energy of the electron once is ejected outside the solid. Substituting equation 2.1.3 into 2.1.1 one obtain

$$\boxed{h\nu = E_B + E_K} \quad (2.1.4)$$

where $E_B = E_n - E_i$ and is referred to as the binding energy of the electron. Equation 2.1.4 elegantly summarizes the idea behind photoemission, that is, if one knows the photon energy that causes the electron excitation and the kinetic energy once the electron is removed from the solid, one can acquire information about which state the electron was inside the solid. In the laboratory one knows the value of the photon energy and using an electron energy analyzer one can determine the kinetic energy of the electron. I must remind you that equation 2.1.4 is incomplete as I just discuss an idealized and simplistic case. In a real solid one must account for the “experimental” work function which is slightly more complicated than that discussed in modern physics books (i.e. energy required to remove an electron from a metallic surface).

2.1.2 The Photoemission Process

In essence, the photoemission process is based on the ejection of electrons from the surface of a material immediately after light absorption. It is this loose definition that has led to the short “photon goes in and electron goes out”. Generally speaking, there is nothing wrong with its definition, except that it hides the real complexity of the process.

From the microscopic point of view, the photoemission process refers to an electron in an initial bound state ψ_i transitioning to a final state ψ_f immediately upon light absorption as seen in [Section 2.1.1](#). However, in this attempt allow me to upgrade the derivation with a slightly more rigorous approach. One must keep in mind that the following calculation lies within the one-electron approximation (electrons interactions among themselves are neglected) and that the derivation has been purposely written to

avoid mathematical details. For a detailed mathematical description, I suggest the book by Hufner [5]. A more elegant (but more complex) approach within the Green's functions formalism can be found in [6].

Regressing to the system depicted in Figure 2.1.1 for clarity, before the absorption takes place, one can solve the time dependent Schrödinger equation

$$i\hbar \frac{d\Psi(t)}{dt} = \hat{H} \Psi(t) \quad (2.1.6)$$

where \hat{H} represent the Hamiltonian operator and $\Psi(t)$ the wavefunction of the electron.

The Hamiltonian operator for this scenario takes the form

$$\hat{H} = H_0 = -\frac{\hbar^2}{2m_e} \nabla^2 + V(r) \quad (2.1.7)$$

with ∇^2 being the Laplacian and $V(r)$ the potential energy of electron. An arbitrary state satisfying (2.1.6) have the form

$$\Psi(t) = \sum_n c_n \psi_n e^{i\frac{E_n}{\hbar}t} \quad (2.1.8)$$

as long as the system is unperturbed (electron does not interact with the photon). To describe the system when the perturbation is on, one must modify equation 2.1.7 given

that the system is no longer described by stationary states. The perturbation effects can be taken into account by modifying the Hamiltonian of the system as

$$\hat{H} = H_0 + U(t) \quad (2.1.9)$$

where $U(t)$ describe the form of the perturbation and H_0 is the Hamiltonian describing the unperturbed system. Substituting equation 2.1.8 into 2.1.6 (keeping in mind that now the Hamiltonian is described by equation 2.1.9) one obtain

$$i\hbar \frac{dc_k(t)}{dt} = \sum_n c_n(t) \langle \psi_k | U | \psi_n \rangle e^{i\frac{E_n}{\hbar}t} \quad (2.1.10)$$

where $\langle \psi_k | U | \psi_n \rangle$ is the matrix element that relate the perturbation to the initial and final state of the electron. The matrix element can be read as “a perturbation of the form U acting on the state ψ_n , leave the system in a final state ψ_k ”, which is what is depicted in [Figure 2.1.1](#). If integration of equation 2.1.10 is performed one can obtain the value of $c_k(t)$. Moreover, knowledge of $c_k(t)$ leads to knowledge of the transition probability (probability that a transition from an initial state to a final state will occur) through the relation

$$P_{if} = |c_k(t)|^2 \quad (2.1.11)$$

Unfortunately, the result obtained once (2.1.11) is solved, suggest P_{if} is infinite as $t \rightarrow \infty$. If instead one chooses to work with the transition probability per unit time ($W_{if} = \frac{P_{if}}{t}$) one can eliminate that complication and obtain

$$W_{if} = \frac{2\pi}{\hbar} |\langle \psi_f | U | \psi_i \rangle|^2 \delta(E_f - E_i + h\nu) \quad (2.1.12)$$

This equation is known as the Fermi Golden Rule and it gives the transition rate between an excitation from an initial state to a final state due to a perturbation U . Notice that the delta function $\delta(E_f - E_i + h\nu)$ ensures that energy is conserved during the transition.

I have been talking about a “perturbation” since the beginning of the section, but what is a perturbation? In this case a perturbation is the effect caused in the system due to the interaction of the electromagnetic field with the atom in which the electron is bound to. Mathematically, the electromagnetic perturbation is of the form

$$U = -\frac{i\hbar e}{2mc} \nabla \cdot \mathbf{A} - \frac{i\hbar e}{mc} \mathbf{A} \cdot \nabla + \frac{e^2}{2mc^2} |A|^2 - e\phi \quad (2.1.13)$$

where \mathbf{A} is the vector potential and ϕ is a scalar potential. Since we have the freedom to choose the potential that define the electromagnetic field of the light wave, we can choose

$$\nabla \cdot \mathbf{A} = 0 \quad (2.1.14)$$

$$\phi = 0 \quad (2.1.15)$$

so the perturbation can be simplified to

$$U = -\frac{i\hbar e}{m_e c} \mathbf{A} \cdot \nabla + \frac{e^2}{2m_e c^2} |A|^2 \quad (2.1.16)$$

Under the assumption that the field is weak $|A|^2$ is negligible and that the momentum operator of the electromagnetic wave is $\mathbf{p} = -i\hbar\nabla$, we can further simplify equation 2.1.16 as

$$U = \frac{e}{m_e c} \mathbf{A} \cdot \mathbf{p} \quad (2.1.17)$$

Therefore, the transition rate can be rewritten as

$$W_{if} = \frac{2\pi}{\hbar} \frac{e}{m_e c} |\langle \psi_f | \mathbf{A} \cdot \mathbf{p} | \psi_i \rangle|^2 \delta(E_f - E_i + h\nu) \quad (2.1.18)$$

Once the states ψ_i and ψ_f are specified we can describe the transition rate due to an electromagnetic perturbation (absorption of a photon). I must insist that this approach assumes that electrons do not interact with each other, which is usually in good agreement with experiments if correlation effects are negligible (not the case in this thesis work). A more realistic approach must take into account the interaction between the $N - 1$

electrons around (many body approach). Nonetheless, this example provides good insight regarding the dynamics of the photoemission process.

From the macroscopic point of view, the photoemission process mainly consists on the elements shown in [Figure 2.1.2](#). A light source is used to provide an incident beam of photons and an electron analyzer to detect the ejected electrons by means of their kinetic energy.

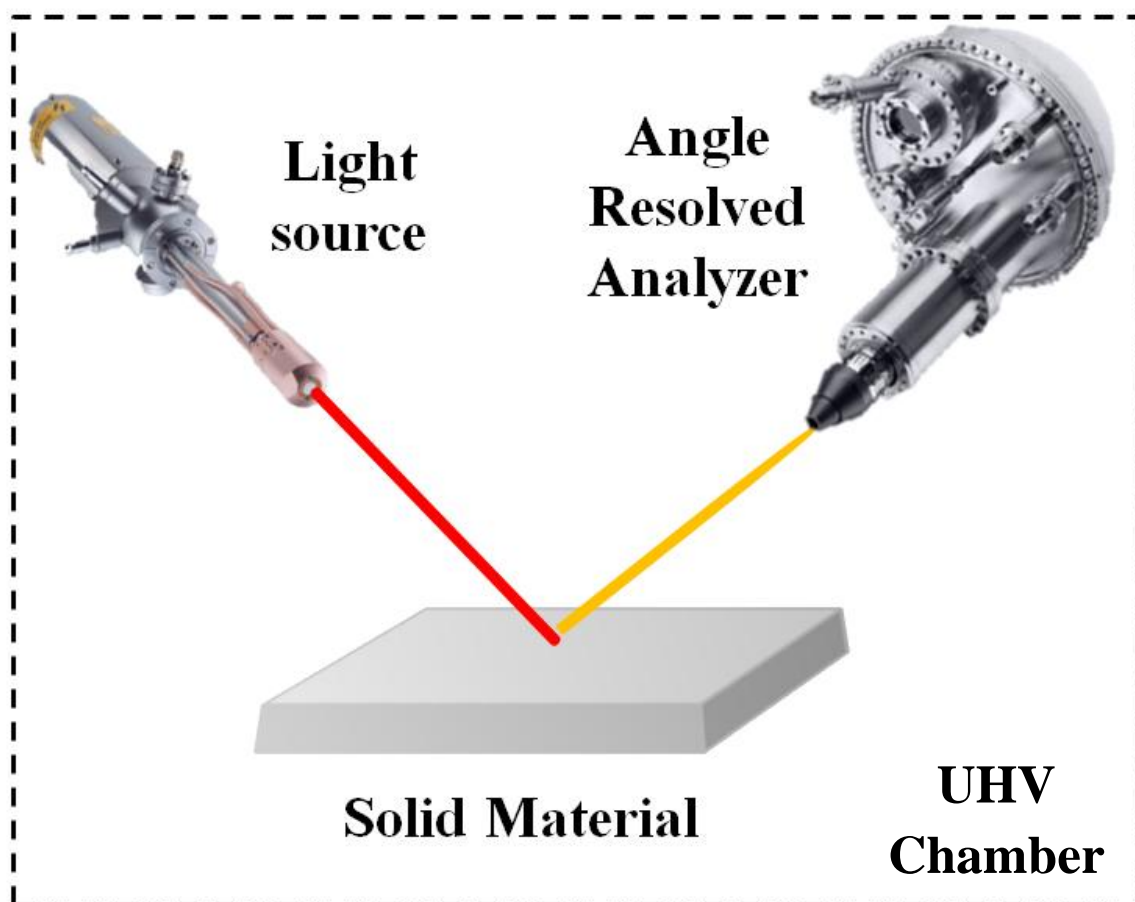


Figure 2.1.2 The main elements of the photoemission process. The picture representing the light source is a dual anode x-ray lamp and the detector is a hemispherical angle resolved electron analyzer, both elements are inside a ultra-high vacuum chamber as denoted by the dashed lines.

Upon photon absorption, electrons are excited from an initial state (also referred as an occupied state) into a final state as discussed above. If the electron gains enough energy

such as to overcome the work function of the system, it will be ejected from the material carrying along a kinetic energy E_K which is then detected by the angle resolved electron analyzer. This process obeys conservation of energy through the relation

$$h\nu = E_K + E_B + \phi \quad (2.1.5)$$

where $h\nu$ is the energy of the photon, E_K is the kinetic energy of the emitted electron, $|E_B|$ is the binding energy of the bounded electron and ϕ is the work function. Equation 2.1.5 is reminiscent of the energy conservation during the Einstein photoelectric process (1905) and is commonly referred to as the photoemission equation. It should be emphasized that the effective work function in this equation is not a property of the solid material per se but of the system configuration itself (i.e. solid material and electron analyzer setup [7]). This process requires ultra-high vacuum conditions (ideally in the order of 10^{-10} Torr) which are achieved by the implementation of the PES elements into a UHV chamber pumped with a roughing pump and a turbo molecular pump connected in series. [Figure 2.1.3 \(a\)](#) shows one of the PES systems used to collect our data.

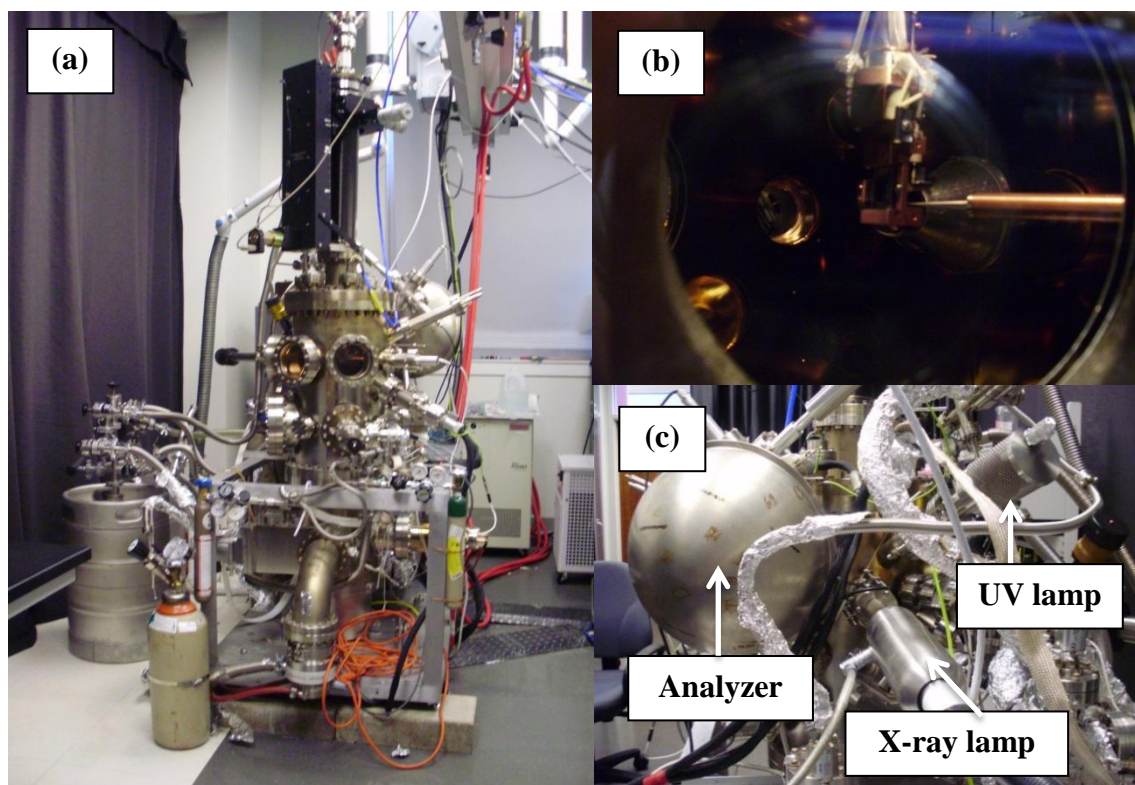


Figure 2.1.3 (a) The ultra-high vacuum chamber employed for the PES process at the spectroscopy laboratory in the University of Nebraska and the geometrical set up of the PES elements both (b) into and (c) out of the chamber.

For this study it was customary to have the beam of photons at an incident angle close to 45° and to collect electrons normal to the surface (except for the data taken with angle resolved photoemission). Also, a typical practice (implemented in our work) is to reference the PES data to the Fermi level of a metal (either clean gold or clean copper), this is particularly useful when dealing with semiconducting material and insulator in which the Fermi level is not clearly defined.

Photoemission spectroscopy find most of its applications in studies of the electronic properties of the electrons in a solid, molecules and surfaces and in the determination of relative elemental composition at the surface of the film. The

experimental measurement of band structure has depended upon two key approaches: de Hass-van Alphen, and angle-resolved photoemission and inverse photoemission. Indeed PES was originally proposed as a method for extracting the experimental band structure by Sir Nevil Mott [8].

2.1.3 Ultraviolet Photoemission Spectroscopy

Ultraviolet photoemission spectroscopy, usually abbreviated UPS, follows the same mechanism as discussed above except that the energy of the incident photons lies in the range of 10 eV to 1000 eV. The name ultra violet is adopted because the wavelength of these photons lies in the ultraviolet region of the light spectra. The first measured valance band photoemission spectra date back to 1964 and is attributable to Spicer, who measured the d band from copper [9]. It is customary to use vacuum ultraviolet (VUV) discharge lamps in the laboratory, with photon energies ranging from 10 eV to 45 eV. For our experiment we use an ultraviolet source from Thermo Electron Corporation, which provide a photon energy of 21.23 eV via a He I α line. The physical geometry of the lamp is shown in [Figure 2.1.4](#).



Figure 2.1.4 Picture of the ultraviolet source employed in our studies. Taken from the Thermo Electron Corporation website.

A typical valence band photoemission spectrum is shown in [Figure 2.1.5](#). Before extracting information of the spectra it is common practice to subtract the background noise of this spectrum which is due to electrons that went through inelastic scattering.

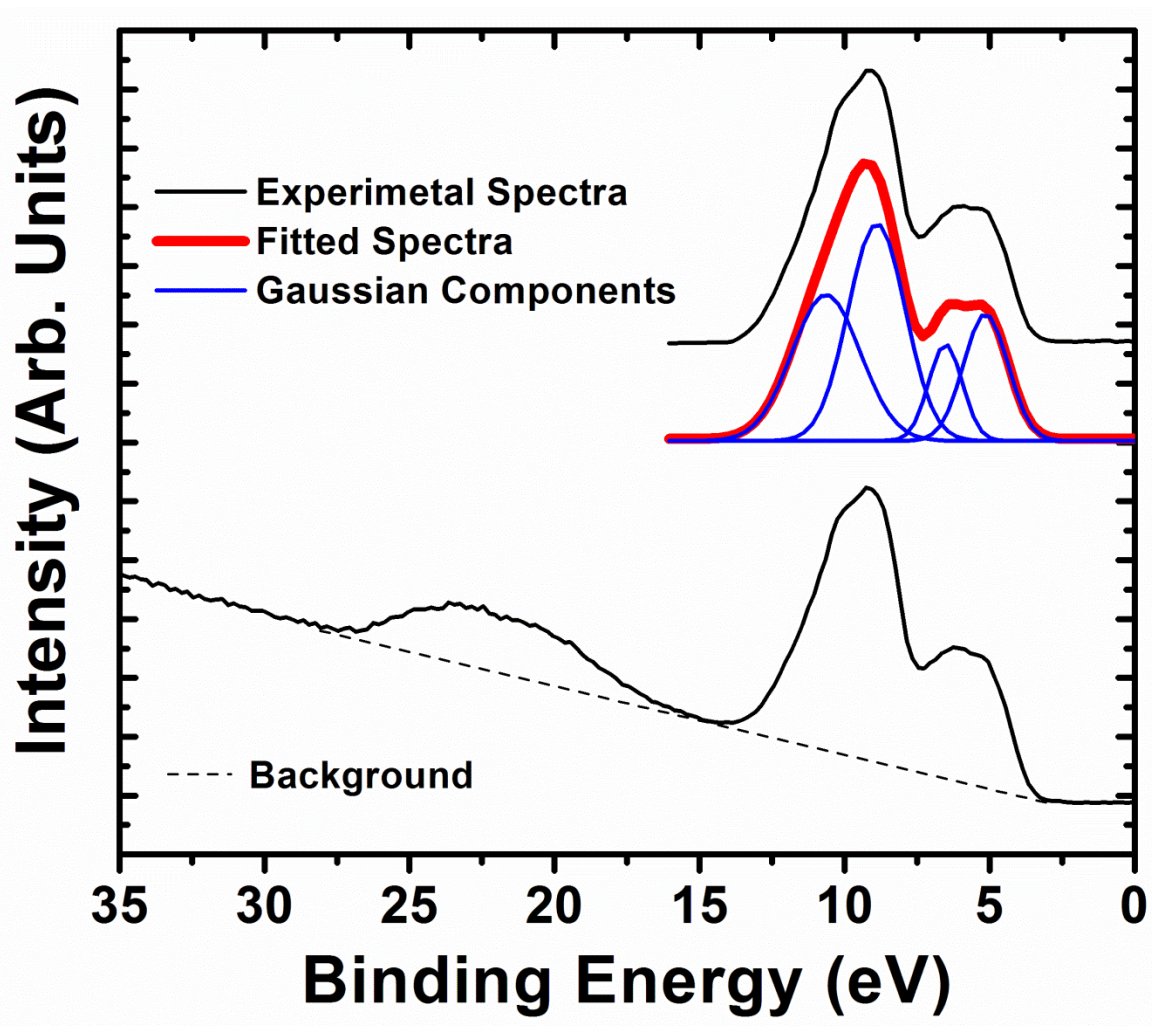


Figure 2.1.5 A typical valence band spectra obtain from UPS. The dashed line indicates the secondary electron tail and is due to inelastic scattering of the electrons before reaching the analyzer. Subsequent steps are shown on the top right portion of the figure.

This background follows a decaying exponential function. However, in some cases, the subtraction of a straight line can be used in good approximation. Then, the spectrum is

deconvoluted into Gaussian distributions, which are then assigned to a specific orbital or to a strong weighted contribution from an orbital. Sometimes the software employed for the UPS measurements do not convert the kinetic energy of the electron into binding energies, nor take into consideration the workfunction of the system. In those cases one can use equation 2.1.5 to obtain an energy conversion. Once the energy is converted into binding energy one can reference the data to the Fermi level of the metal as discussed above.

What makes this technique valuable is the high resolution possible in these measurements, but complications exist as the photoemission cross sections are not always well defined for photons of low energy. Second, the low energy allows probing the electrons orbiting in the valence band of the solid as shown in [Figure 2.1.6](#). In the context of this work, UPS will prove very useful as it will give us information about the bonding of the material and combined with inverse photoemission (see [Section 2.2](#)) provide an estimate of the solid electronic band gap.

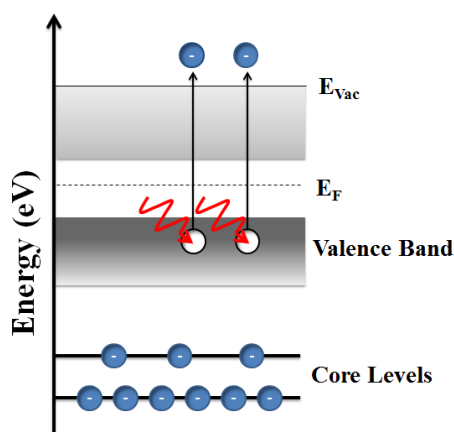


Figure 2.1.6 Energy level diagram describing the ultraviolet photoemission process.

2.1.4 X-ray Photoemission Spectroscopy

X-ray photoemission spectroscopy (XPS) also obeys the same process underlined on [Section 2.1.1](#) with the difference that the photons causing the electronics excitations have energies in the range of 1000 eV-10 keV. Since photon energies are far greater than those used in the UPS process, electrons from the core levels can be removed from the material as depicted in [Figure 2.1.7](#) and detected by the electron analyzer.

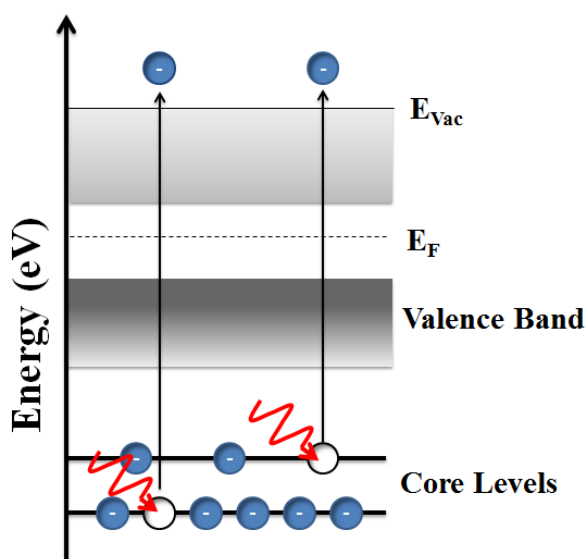


Figure 2.1.7 Energy level diagram describing the X-ray photoemission process.

This technique will allow for the extraction of chemical oxidation states, elemental composition and in some cases extract the effective Debye temperature of the solid, which may accompany a phase transition. The development of a high resolution XPS analyzer for the studies of core level binding energies is reported to begin with the work done by Siegbahn [10]. A typical X-ray source in the laboratory uses either aluminum or magnesium for the anode material which can provide energies of 1486.6 eV with the Al-K α line or 1253.6 eV with the Mg-K α line. The main reason to have two anodes in the x-rays source is due to Auger electron spectroscopy lines that are formed in during the

photoemission process. These Auger lines are constant in kinetic energy and totally dependent on the anode used. Sometimes, these lines can overlap in the energy range of an energy band from the compound, burying the signal from the solid or interfering with the signal. By changing the anode, one can change the position of the Auger line, so the overlapping of the signal will not occur.

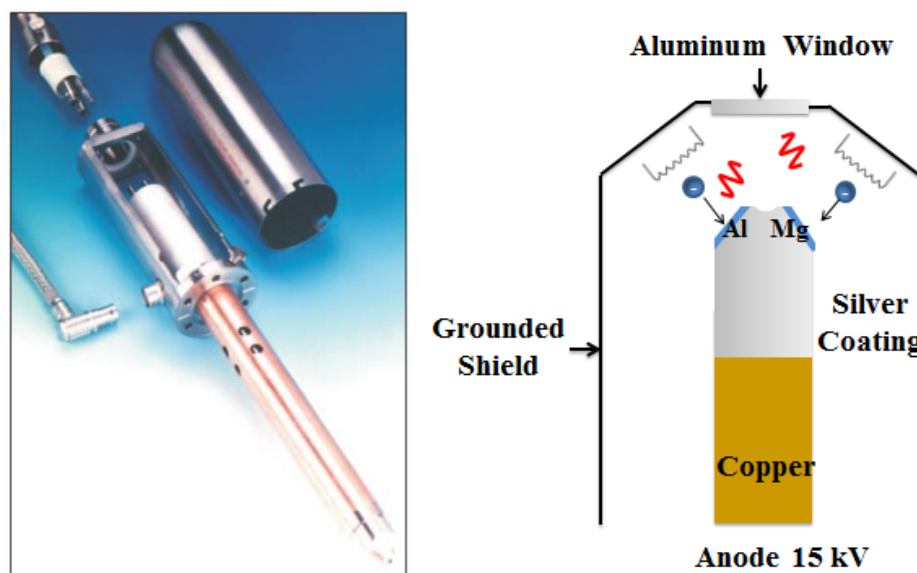


Figure 2.1.8 (a) The physical geometry of the X-rays source and (b) a schematic of the of the X-ray source. Figure (a) was taken from the Thermo Scientific's application note 31057.

Electrons are emitted from a thoria-coated iridium filament (to provide high emission and longer usage of the cathode) and accelerated towards the anode due to the electric field formed by the potential difference of 15 keV as shown in [Figure 2.1.8 \(b\)](#). When the electrons strike either the magnesium or aluminum anode, they lose energy causing a deceleration hence emitting light in the x-ray regime. However, the x-ray light must be filtered to reduce bremsstrahlung irradiation and to minimize the contamination of the sample in the UHV chamber due to thermal desorption from the internal structures of the

x-ray source. To this end, an aluminum window is placed at the aperture of the source as shown in [Figure 2.1.8 \(b\)](#).

2.1.5 Resonant Photoemission Spectroscopy

Resonant photoemission also results in the same final state described in [Section 2.1.1](#) except that the photon energy provided by the light source is varied over a wide range. The photon energy can be selected from a continuous set of values (5.0 eV up to 1500 eV) with the implementation of a monochromator and a synchrotron source. A synchrotron light source refers to the combination of a particle accelerator, a storage ring and a set of beamlines. The process starts out by producing thermal electrons via an electron gun. These electrons are then accelerated by a large electric field and directed into a linear accelerator (LINAC). At the exit of the LINAC electrons had gain a huge amount of energy due to microwave light absorption, so they leave the accelerator with speeds close to the speed of light. From the LINAC they enter to what is called the booster ring in which the electrons are forced to travel in a circular path by means of magnetic forces due to bending magnets. This results in electrons with energies in the order of GeV. The next stage is to feed this beam into the storage ring where the electron beam will be traveling in a quasi-circular path, reinforce periodically with accelerators to keep their speed almost constant. How do we get light out of this ring? Right before the beam line, there is a bending magnet which will cause the electrons to accelerate as it curves, this will cause light emission which will be directed into the specific beamline. The actual process is easier said than done! One must use extra instrumentation to keep the electron beam focused, ultra high vacuum conditions to avoid scattering events, and

electron injections to maintain the flow of electrons. After light is emitted, the need of a monochromator is imperative to reduce the energy of the photons.

Our experiments on resonant photoemission spectroscopy (RPES) and high resolution angle resolved photoemission spectroscopy (ARPES) were performed in the Center of Advanced Microstructures & Devices (CAMD) in Baton Rouge, Louisiana. [Figure 2.1.9](#) shows a schematic of the storage ring in CAMD along with their beamlines. The 3m toroidal grating monochromator (TGM) and the normal incidence monochromator (NIM) beamline that were employed for our experiments

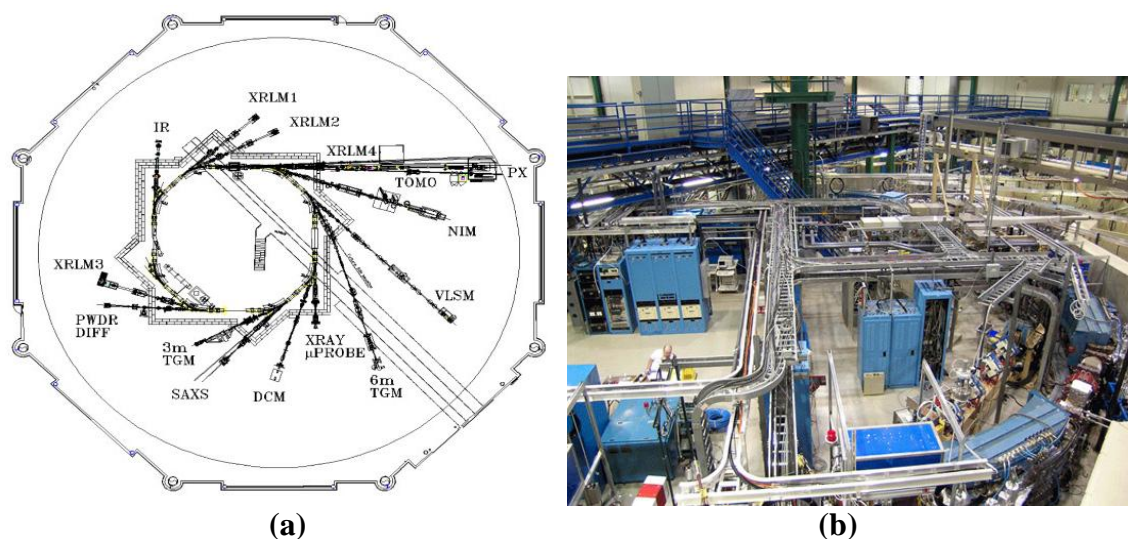


Figure 2.1.9 A (a) schematic and (b) picture of the storage ring in CAMD. Taken from [11, 12].

A schematic of the beamline and a picture of the 3m TGM is shown in [Figure 2.1.10](#).

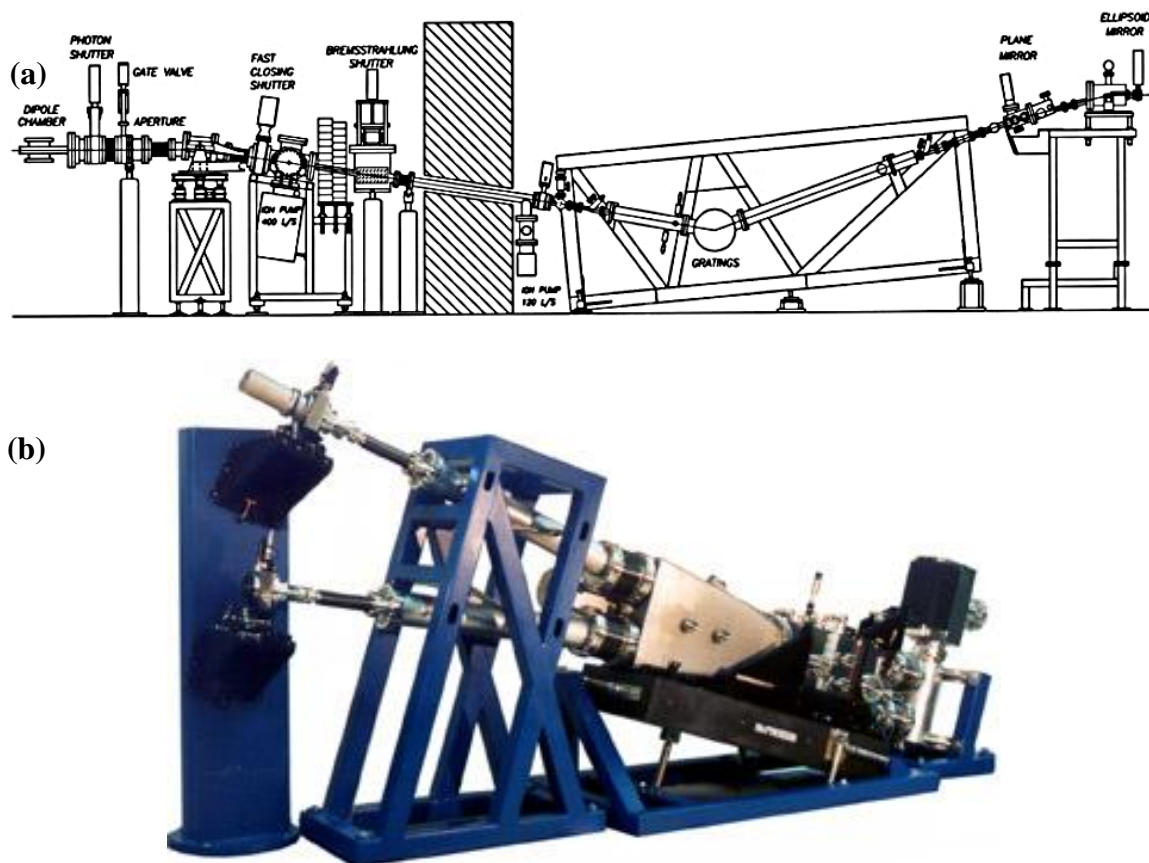


Figure 2.1.10 (a) The 3m TGM beamline and (b) a picture of the TGM. Taken from [13, 14].

For the sake of completeness, the UHV chambers employ in the experiment are shown in [Figure 2.1.11](#).

There are two main advantages when using a synchrotron source. One, the variation of photon energy allows for the mapping of the electronic band structure along the growth direction of the compound (assuming the compound has a strong texture). Second, the photoemission cross section of the elements has an energy dependence so resonance studies on rare earth and some transition metals can be performed. Among

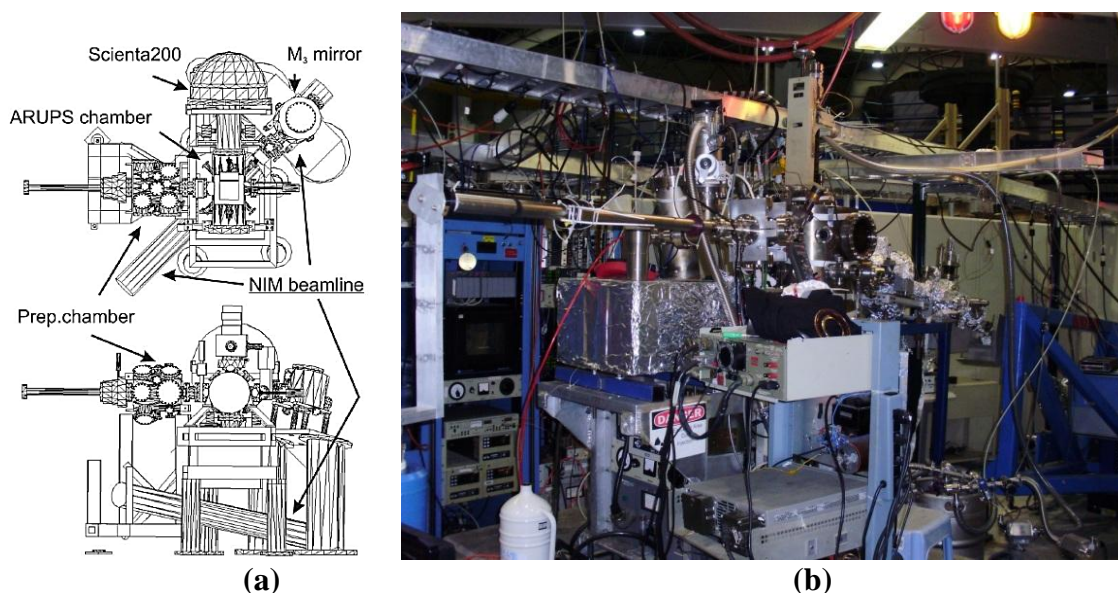


Figure 2.1.11 (a) The UHV chamber used for the high resolution angle resolved photoemission spectroscopy and (b) the resonant photoemission experiments. (a) was taken from [15].

other advantages are high intensity and brightness, small beam size spot and variable polarization. Given the nature of the light polarization from a Synchrotron source (and if symmetry permits), one can select to probe contribution from one orbital or another as permitted by the photoemission selection rules.

Regarding the studies reported in this work, RPES will prove extremely useful when we purposely scan through the resonant regions of gadolinium and europium rare-earth elements to study the resonances processes taking place in the solid, and high resolution ARPES will be used to map the electronic band structure near the Fermi level. A whole chapter ([Chapter 6](#)) is devoted into discussing resonant effect and how these affected by the conductivity of the sample in question.

2.1.6 Matching the Photoemission and the Theoretical Density of States

It is important to understand the means in which the experimental density of states (DOS) is obtained and how it is compared to experiments. Having studied the basic features of the PES process, it is worth expanding the relationships between the theoretical band structure of a solid and the electron energy distribution derived or established in the PES process. As shown in [Figure 2.1.12](#), the electron energy distribution of the photoemission spectra often gives a replica of the electron energy distribution in the solid, although slightly modified (changing cross-sections, matrix element effects, quantum selection rules and the fact that it is a final state spectroscopy means photoemission is not and cannot be an exact reproduction of the ground state density of states). In the theoretical DOS calculation ([Figure 2.1.12 \(a\)](#)) the energy levels corresponding to the core electrons is represented by a delta function (straight line in the E v.s. $N(E)$ plot), whereas the valence band electrons, being more delocalized, undergo dispersion as suggested by the quadratic increase in the density of state. Notice that the Fermi level dictates the energy of the electron at the highest occupied state in the solid at temperature $T = 0 K$, and the vacuum level represents the energy that must be overcome to release the electron from the solid. The spectrum measured by the photoemission process (also referred to as the photoemission density of state) resembles quite closely the solid density of state as shown in [Figure 2.1.12 \(b\)](#). The core level electron energies are broader due to non-idealities such as inelastic collision of the detected electrons and instrumentation resolution.

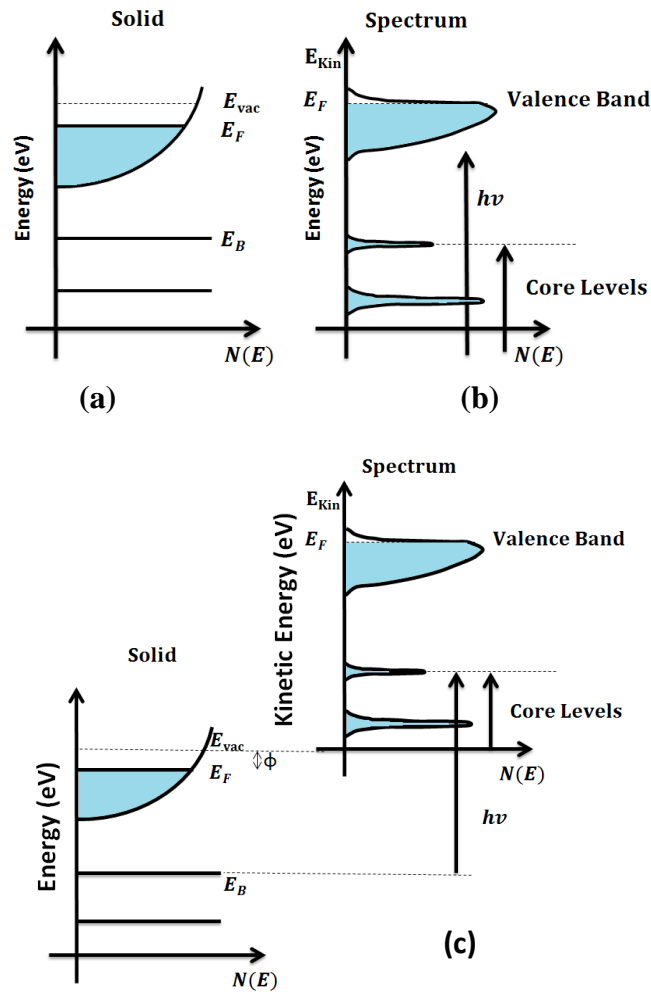


Figure 2.1.12 The relation between the density of state from a (a) theoretical and (b) experimental point of view. (c) The reference energy between the two DOS distribution.

The valence band also undergoes changes due to finite temperature effects as seen by the tail extending above the Fermi level, but overall, both DOS are qualitatively similar. A major difference between these two DOS measurements is the energy scale in which they are measured. The theoretical calculation alludes to what happens inside the solid whereas the experiment makes reference to what happens outside the material. This is

why usually PES is referred to as a final state measurement in order to determine an initial state, whereas in theory one builds an initial state. As shown in [Figure 2.1.12 \(c\)](#), if one wants to compare the two density of states, an adjustment in energy must be made. The energy conservation expression [equation (2.1.5)] takes care of this problem.

2.1.7 Connection between Photoemission and Reciprocal Space

In a crystalline material, atoms are placed in a periodic lattice, usually called a bravais lattice. A bravais lattice is an infinite array of discrete points with an arrangement and orientation that appears exactly the same, from whichever of the points the array is viewed. Schrodinger equation tells us that the wavefunction of the electron moving throughout the lattice must adopt the periodicity of the crystal if one wants to describe the states in which the electrons are inside the solid. Due to the wave nature of the electron, knowledge of the exact position of the electrons is not possible. However, not all hope is lost... for each wavefunction (or state) allowed by the Schrodinger equation, the electron will have a definite wavelength or momentum through the de Broglie relation

$$p = \frac{h}{\lambda} \quad (2.1.6)$$

This is, for each wavefunction the Schrodinger equation allows, we can know to a large certainty, the wavelength corresponding to the electron in that state (or the wavevector through the relation $k = \frac{2\pi}{\lambda}$). Each of the allowed k values form a space on its own, this space is called reciprocal space.

To summarize the above in short words, electrons that contribute to the electronic band structure are delocalized in real space (i.e. their exact position is unknown), instead, we defined a new space, called reciprocal space (or k-space), in which the energy of each electron is well define (are known accurately) through the wavevector \mathbf{k} . For this reason, all theoretical calculations yield energy expressions in terms of the wavevectors. In a E vs \mathbf{k} plot, each \mathbf{k} point is interpreted as a possible state an electron can occupy or is occupying based on the placement of the Fermi level. However, measurements of the PES process only provide us with the kinetic energy of the electron and the emission angle of the ejected electron. Well... how do we construct the experimental electronic band structure with that information? This question is quite subtle, let's make use of [Figure 2.1.13](#) in an attempt to bring clearness to the problem.

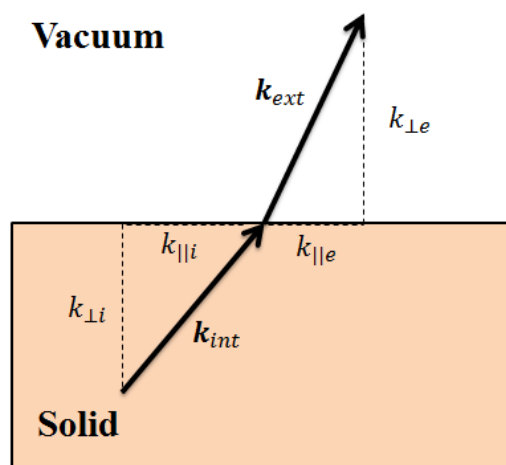


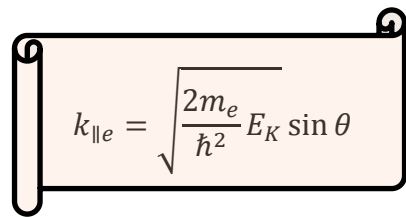
Figure 2.1.13 Schematic of the electron propagation along the solid vacuum interface.

After the electron make the transition from the valence band into the conduction band, it will propagate trough the crystal with wavevector \mathbf{k}_{int} . Once outside the sample, we can describe with a wavevector \mathbf{k}_{ext} . The transmission of the electron trough the

surface into the vacuum requires that the wavevector component parallel to the surface to be conserved, this is,

$$k_{\parallel e} = k_{\parallel i} \quad (2.1.7)$$

but $k_{\parallel i}$ is given by $\sqrt{\frac{2m_e}{\hbar^2} E_K} \sin \theta$, hence



$$k_{\parallel e} = \sqrt{\frac{2m_e}{\hbar^2} E_K} \sin \theta \quad (2.1.8)$$

Unfortunately, for its component normal to the surface there is a key complication. The potential step across the solid-vacuum interface k_{\perp} is not a conserved quantity and has to be corrected by an additional potential term (often called the inner potential. In the simplest assumption, one can assume a free electron in the final state inside of the crystal with parabolic dispersion given by

$$E_f = \frac{\hbar^2 k_{\perp}^2}{2m_e} - U_{in} \quad (2.1.9)$$

Once the electron is in the vacuum side, conservation of energy dictates that

$$E_K = E_f - E_{vac} \quad (2.1.10)$$

However, $E_{vac} = 0$ is our reference level for the measured kinetic energy in the PES process, hence, by substituting equation 2.1.9 into 2.1.10 and solving for k_{\perp} we obtain

$$k_{\perp} = \sqrt{\frac{2m_e}{\hbar^2} (E_k + U_{in})} \quad (2.1.11)$$

It turns out that the photoemission results can be directly related to the reciprocal space through the relations 2.1.8 and 2.1.11. These relationships are of extreme importance, as they unify the PES results with the reciprocal space of a solid. The meaning of these wavevectors is summarized in [Figure 2.1.14](#). Note that for each value of the electron kinetic energy and/or each value of the emission angle, different values of k_{\perp} or k_{\parallel} are obtained. When these different wavevector values are plotted with the measured energy (this process is referred to as mapping into k-space), it results in the electronic band structure of the solid. An example of this can be seen in [Figure 5.2.4](#) and [Figure 5.2.5](#) in [Chapter 5](#).

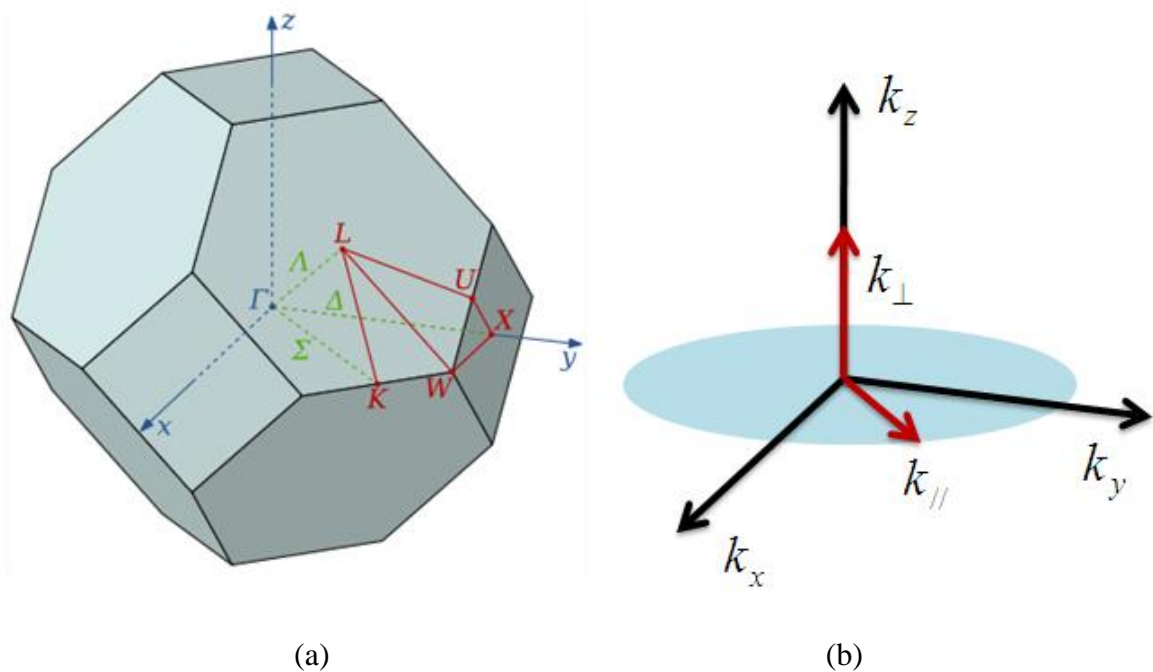


Figure 2.1.14 (a) The first Brillouin zone for a face centered cubic (FCC) lattice and (b) the wavevectors along the direction perpendicular to the surface of a film and the wavevector along the direction parallel to the surface of the film.

2.1.8 Charging Considerations in PES

One key ingredient in the photoemission process is the compensation of the electron lost in the ejection. This is usually fulfilled by “grounding” the sample to a vast source of electrons (say Earth). In a metal and many semiconductors the replacement of the lost electron is fast and does not interfere with the results of the experiment. Unfortunately in high k insulators (such as the ones in this work) this charge compensation represents a bit of a problem. In this type of materials a positive potential can develop in the region where the light beam is incident since the ejected electron cannot be compensated leaving behind a positive charge at the surface. The positive charge accumulates and interacts electrostatically with the ejected electron, reducing its

kinetic energy. The problem with this phenomenon is that the electron analyzer base its detection capabilities in the electron kinetic energy. This charging effect will lead to energy bands shifted from their actual position. If the charging is very strong, the shift in binding energy can be such as to bury the band in the secondary electron tail, or can lead to a decrease in the photoemission intensity. To complicate this even further, if the charging is non-uniform, electrons in different regions of the material can feel different retarding potential. This will result in broadenings of the electronic bands and sometimes even distortions. It is common to make a distinction between lateral and vertical differential charging as discussed in [16].

However, several approaches and studies have been performed to solve this problem [17]. The use of a reference material such as carbon [18] or a gold layer [19] has been implemented, as well as the use of a very thin layer on a conducting substrate [20]. Flood guns [21] have been successfully used to supply electron to the surface of the film compensating whatever hole is created in the photoemission process. An alternate way to get around this problem is to heat the material at elevated temperatures. This approach is the one used in this work. The idea consists on promoting valence electrons to the conduction band where they can travel freely and recombine with any hole in their trajectory. One might claim that the electronics properties at these high temperatures might be altered and might not resemble those at room temperature, but in fact changes are not that drastic so one can make analogies between both limits. In cases in which charging is strong, useful information can be extracted in terms of the activation energy of the material.

2.2 Inverse Photoemission Spectroscopy

Inverse photoemission is a technique that is used to probe the unoccupied density of state of a crystalline material. As suggested by the name (although not a spectroscopy itself), inverse photoemission is the “inverse of the photoemission process, loosely speaking “electron goes in and photon goes out”. Formally, low energy electrons are directed into the film, these electrons then couple to a higher energy state and decays to a lower energy state. During the decay between the energy levels, a photon is emitted with some energy characteristic of the transition (i.e. the photon energy is equal to the energy difference between the energetic levels) as [Figure 2.2.1](#) suggest. The electrons are supplied by an electron gun and the photons are detected using a Geiger-Muller detector as denoted in [Figure 2.2.2](#) [22].

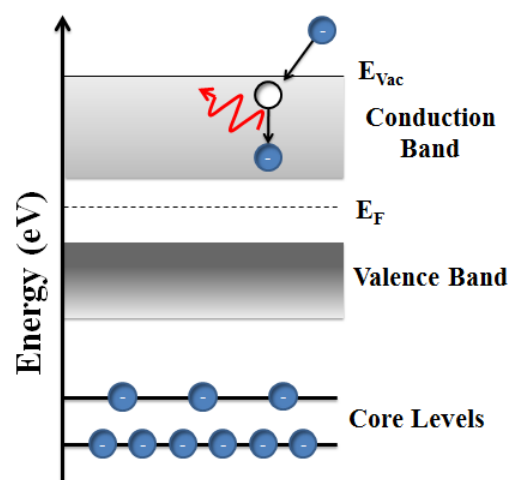


Figure 2.2.1 Energy level diagram summarizing the IPES process.

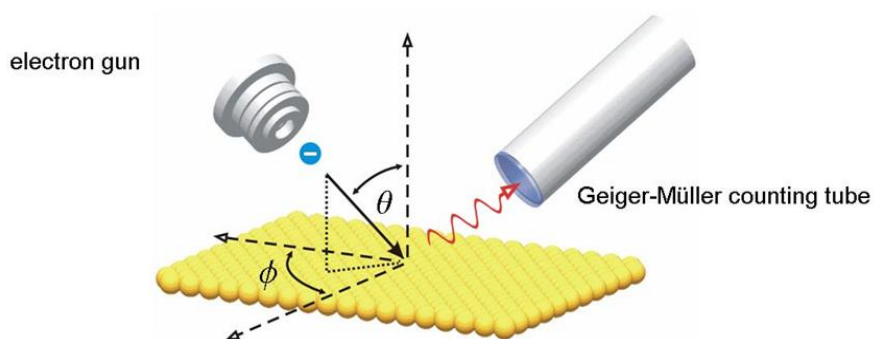


Figure 2.2.2 Schematic of the inverse photoemission process.

Given the low energy of the electrons this technique is very surface sensitive (meaning that one can probe most of the surface details and less of the bulk details, unlike the case of photoemission). This also means that the surface of the material must be treated carefully depending on the experiment to be performed, as contaminant signal can be picked, affecting the reliability of the data.

2.3 Neutron Detectors

There are currently two mechanisms used for the detection of neutrons; scintillation and the use of semiconductor to form diodes detectors. We adopted the later for neutron testing using Gd:HfO₂ films on p-type Si(100). In general, when an n-type material (such as Gd:HfO₂) is deposited on a p-type material they form a p-n junction which result in a rectifying diode. Since electrostatic equilibrium conditions must persist between the two materials when unbiased, charge transfer between the two materials will lead to the formation of a depletion region (Figure 2.3.1). This will result in a band bending near the interphase of both materials, resulting in the formation of a potential

step as shown in Figure 2.3.2. The potential step dependence on the bias voltage is what one wants to exploit in these devices as the polarity of the bias voltage will determine how much current will flow through the device.

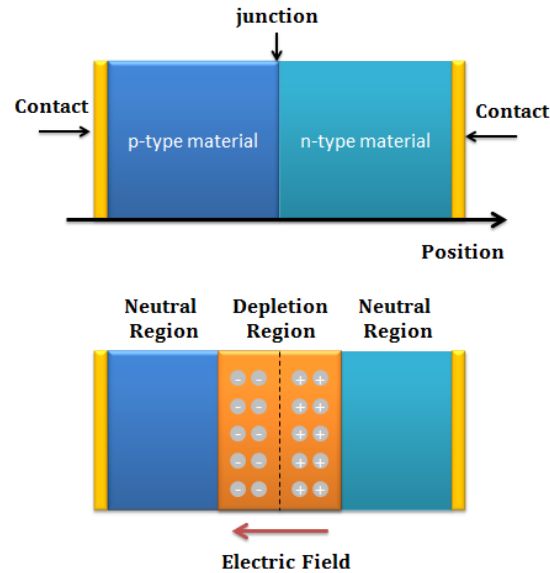


Figure 2.3.1. A schematic showing (a) the p-n junction geometry and (b) the depletion region and neutral region of a diode.

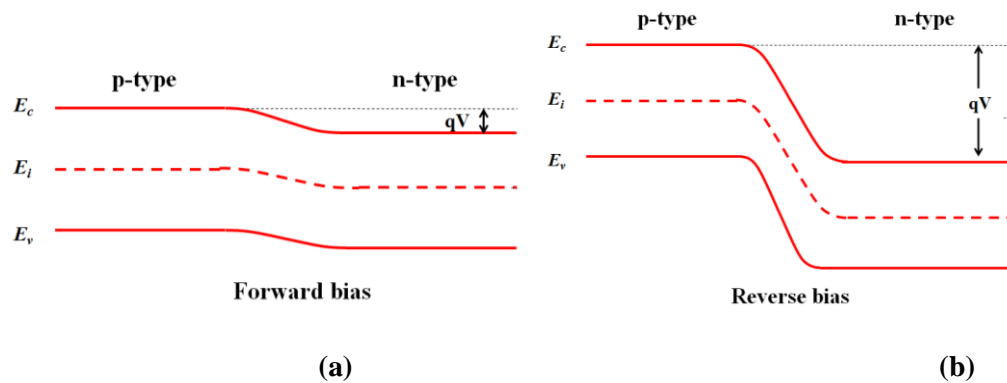


Figure 2.3.2. A p-n junction diode in (a) forward and (b) reverse bias operation.

We are interested in the reverse bias mode for neutron detection for two reasons. First, the number of carriers in this bias mode is very small at operating temperatures resulting in small leakage currents through the material in the absence of radiation. This will facilitate the detection of the energy deposited by the incident radiation once the neutron capture event takes place. Secondly, after the electron-hole pairs are formed by charged particle excitation, the carriers need to be separated as fast as possible, before recombination occurs, if one wants to detect a pulse. In this configuration the depletion region can extend into the bulk of the material resulting in a strong electric field throughout the depleted region, which will facilitate the carrier transport

A typical setup is depicted in [Figure 2.3.3](#). Plastic (with large hydrogen content) is used to slow down the neutrons so detection can be achieved as the neutron capture cross section is higher at lower energies. Also a cadmium or lead foil can be implemented to discriminate from Gamma-rays signals. Once the nuclear reaction occurs, electron-hole pairs will travel through the material and injected into the contacts, where detection will occur in the form of a pulse. Unfortunately, these pulses are weak and one requires an amplification stage to have signals strong enough to be detected by both the pulse counter and the amplifier.

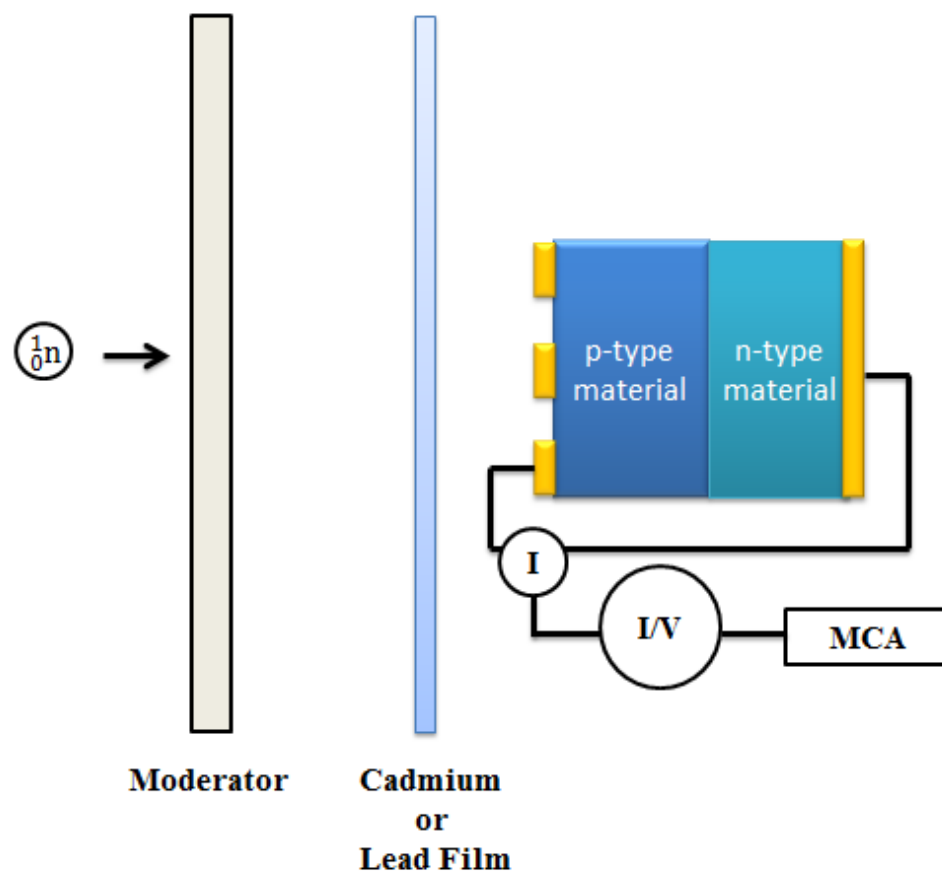


Figure 2.3.3 The neutron detection mechanism for a diode detector. The neutrons are incident into a moderator (usually a hydrocarbon plastic) to slow them down. Cadmium foil is used to test for Gamma sensibility although a thin foil of lead is sometime used.

The neutron capture pulse height spectra will be taken using a curie plutonium–beryllium source which provided 2.2×10^4 thermal to epithermal neutrons $\text{cm}^{-2} \text{s}^{-1}$, as calibrated by foil activation methods. The diodes were reverse biased with 2V, a value well below the breakdown voltage. The pulse height spectra gathering electronics were developed and implemented in a single-chip solution. The pulse counting and binning electronics is based on a solution that integrates a custom low-power microcontroller core, I/O hardware, timers, SRAM and a low-power radiation sensor front-end on a single chip using a $0.35\mu\text{m}$ CMOS technology. The design choices have been driven by low operating power, small chip area, reliable communication and robustness constraints. The

overall detection and binning architecture are schematically shown in [Figure 2.3.4](#). The neutron capture pulse sensor front-end is based on a charge sensitive amplifier (CSA) circuit that has significant reduction in power consumption [23], compared with [24]. This effective multichannel detector design allows the peak current available to the CSA to be more than 20 times the dc bias level by utilizing an adaptive bias scheme that dynamically scales the bias current during a particle detection event.

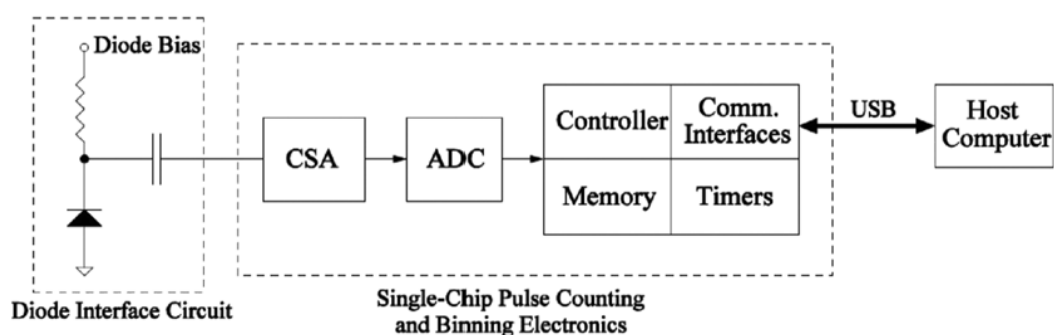


Figure 2.3.4 Single-chip pulse counting and binning electronics block diagram. The design occupies a total silicon area of 10mm² fabricated in a 0.35 μ m CMOS technology (see text). The charge sensitive amplifier (CSA) and analog-to-digital converter (ADC) are indicated schematically.

This permits the amplifier to stay in the linear region allowing more accurate characterization of neutron capture detector events. The microcontroller core responsible for processing the particle events for binning and transmitting the data to a host system is a standard 16 bit RISC architecture with 28 instructions implemented with a clock speed of 8 MHz. The core consumes 17 000 digital gates with an estimated extra 3000 gates required for a test access port. Communication with the chip is accomplished with a 3V USB-to-serial communications device. The entire circuit consumes between 39 and

400 μ W of power depending on the particle detection rate. The maximum possible analog to-digital converter (ADC) conversion rate, and therefore particle detection rate, is 300 000 samples s^{-1} , but here we have exploited the large charge/voltage integration times available, for better pulse height resolution. A conversion gain of 833 μ VfC $^{-1}$, corresponding to 1.2 pF of integration capacitance, has been utilized. With an 8-bit ADC resolution, 256 bins were created using an incremental bin resolution of 5.64 fC/bin, which corresponds to 4.7 mV after charge-to voltage conversion. A diode bias level of 2V has been used with a bias resistor value of 20 kohms

2.4 X-ray Absorption Fine Structure

X-ray absorption spectroscopy (XAS) is a technique used for determining the absorption coefficient of a material as a function of photon energy via the comparison of the incoming light intensity and the outgoing light intensity. This provides useful information about the chemical and physical states of an atom. A typical absorption spectra obtained from this technique is shown in [Figure 2.4.1](#). Due to the information provided by different segments of the spectra, is common to divide the absorption edge spectra into three different regions. The first region is named the pre-edge region and it contains information about ligand fields and oxidation states. The second region is referred as x-ray absorption near edge structure (XANES) and provide information about the oxidation states and coordination chemistry. The third region is referred as extended x-ray absorption fine structure (EXAFS) and provides information about the distance, coordination numbers and species of the neighbors of the absorbing atom.

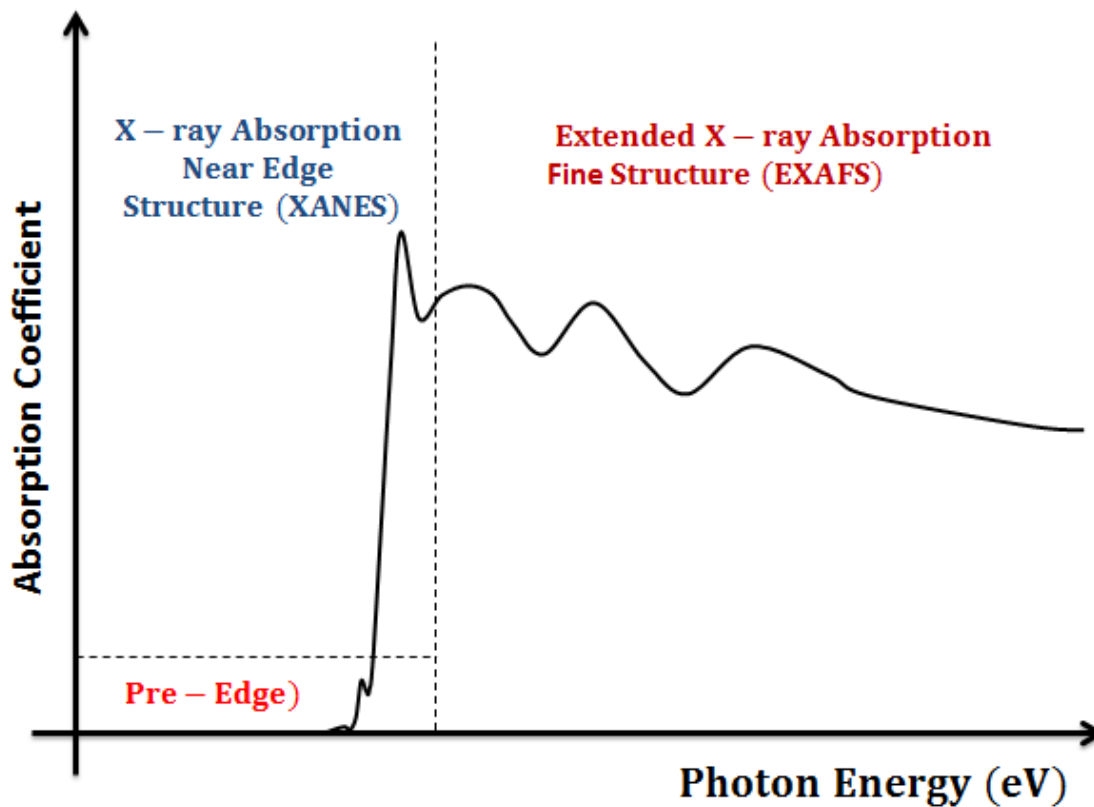


Figure 2.4.1 A hypothetical x-ray absorption spectra.

Although there is no clear distinction, the XANES region is around 30-50 eV of the main absorption edge. The rest is considered as part of the EXAFS region.

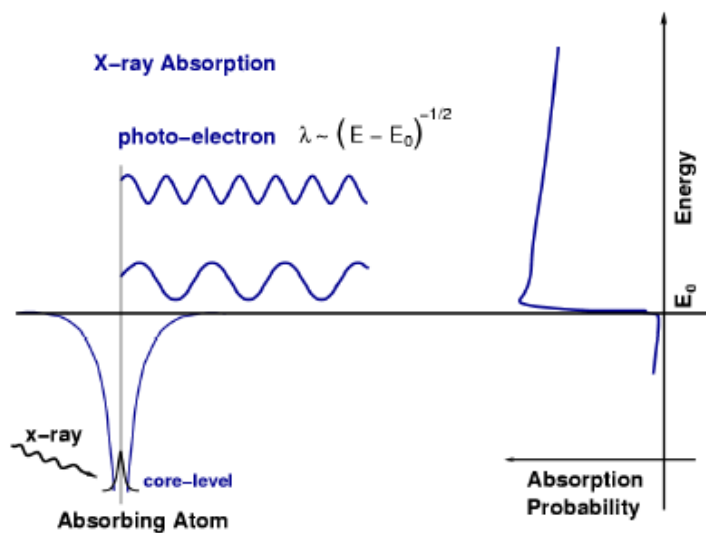
This process starts with the absorption of an x-ray photon by a core level electron. If the x-ray photon energy is equal (or higher) to the binding energy of the core level electron, this electron can be promoted to a continuum where it behaves as a wave with wavelength given by

$$\lambda = \frac{2\pi}{\sqrt{\frac{2m_e}{\hbar^2}(E - E_0)}} \quad (2.4.1)$$

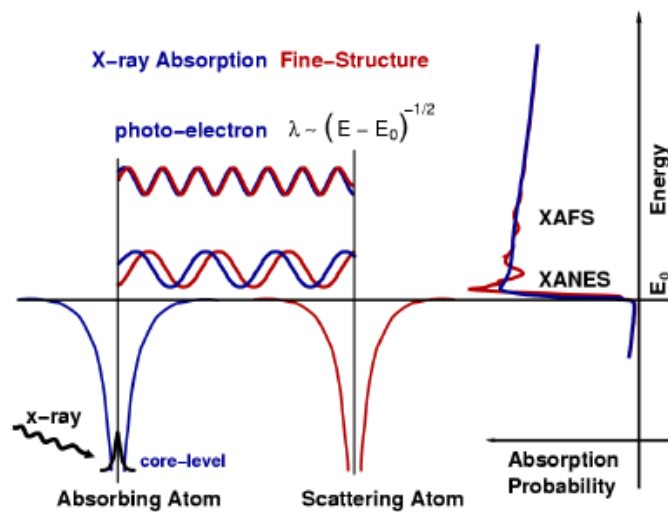
In the case where there are no neighbors, the electron propagates with an absorption probability as depicted in as shown in [Figure 2.4.2 \(a\)](#). When the same process takes place but the neighbor's atoms are included into the picture, the electrons that are excited from the absorbing atom can suffer scattering from neighboring atoms and returning to the absorbing atom resulting in a modulation of the absorption coefficient or wavefunction at the absorbing atom site.

Macroscopically, the XAFS set up consist of the instrumentation as shown in [Figure 2.4.3](#). The x-ray beam is generated by a synchrotron which is then monochromatized and energetically tuned up by a monochromator. Then, the intensity of the incident light is recorded and compared do that detected in the fluorescence or transmitted detector, depending of the mode being implemented. Synchrotron radiation is implemented due to its high intensity and photon energy tunable characteristic. Since our samples are thin films, the fluorescent mode was employed as is known to be more sensitive to films with low elemental concentrations (in the transition mode the signal is overwhelm by large background absorption). The connection between the absorption coefficient and the intensities detected in the fluorescence mode is

$$\mu(E) = \frac{I}{I_0} \quad (2.4.2)$$



(a)



(b)

Figure 2.4.2 Schematic of x-ray absorption in terms of an energy diagram and the absorption probability spectra for the case where (a) there are no neighbors and (b) the photo-electron can scatter from a neighboring atom. This figure was taken from [25].

This is very useful because from a theoretical stand point, the EXAFS part can be described by

$$\mu(E) = \mu_0(E)[1 + \chi(E)] \quad (2.4.3)$$

where $\mu_0(E)$ represents the absorption coefficient of the absorbing atom as if there were no neighbor atoms (no scattering) and $\chi(E)$ is a function that describe the oscillatory behavior right after the rising edge. The function $\mu_0(E)$ is usually known, $\mu(E)$ can be determine experimentally, this means that the form $\chi(E)$ can be calculated.

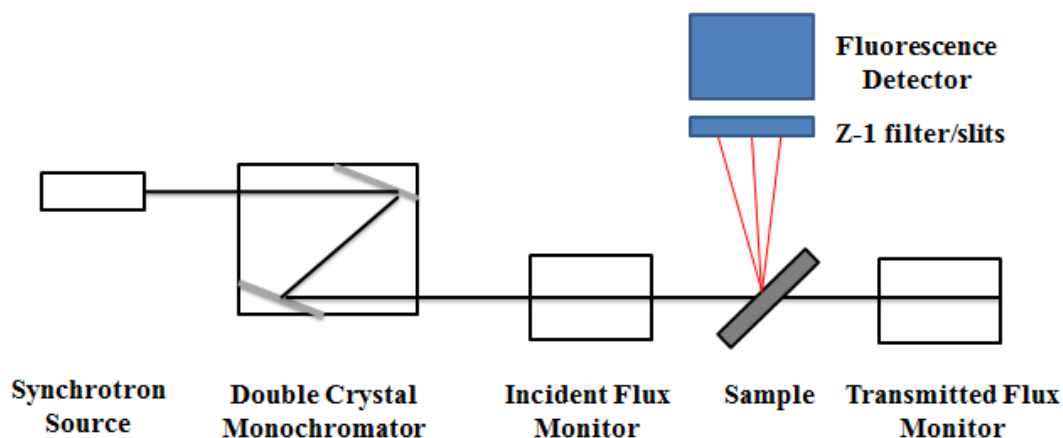


Figure 2.4.3 Schematics of experimental setup for XAFS measurement in fluorescence mode from CAMD.

This in turn will allow for the identification of near neighbors coordination shells which can be modeled using the EXAFS equation

$$\chi(E) = \sum_j \frac{N_j e^{-2k^2 \sigma_j^2} e^{-\frac{2R_j}{\lambda(k)}} f_j(k)}{k R_j^2} \sin[2k R_j + \delta_j(k)] \quad (2.4.4)$$

For the sake of clarity, $f_j(k)$ is the scattering amplitude, $\delta_j(k)$ is the phase shift, N_j is the number of neighboring atoms, R_j is the distance to the neighbor atom, σ_j^2 is the disorder in the neighbor distance. The subscript j represent the individual coordination shells of identical atoms at approximately the same distance from the central atom and the exponent $e^{-\frac{2R_j}{\lambda(k)}}$ accounts for inelastic scattering and the core hole lifetime. Equation (2.4.4) will allows us to know N , R and σ_j^2 and since $f_j(k)$ depends on the atomic number Z of the neighboring atom, EXAFS is sensitive to the atomic species of the neighboring atom. It is customary to multiply $\chi(E)$ by a power of k to emphasize the oscillation.

This equation implies that XAFS can probe about 5 Å or so, so it is perceived as a local probe technique. The XAFS oscillation will consists of different frequencies that correspond to different distances for each coordination shell, which will lead to the use of Fourier transforms in the analysis. The values for $f_j(k)$ and $\delta_j(k)$ are included in the FEFF software.

References

- [1] H. Hertz, “On the influence of Ultraviolet light on the electric discharge”, *Annalen der Physik* **267** (8): 983–1000 (1887).
- [2] A. Einstein, *Annalen der Physik* 322, Issue 6, 1521-3889 (1905)
- [3] H.P. Bonzel, Ch. Kleint, “On the history of photoemission”, *Progress in Surface Science*, Volume 49, Issue 2, June 1995, Pages 107-153.
- [4] Friedrich Reinert and Stefan Hüfner, “Photoemission spectroscopy—from early days to recent applications”, *New J. Phys.* 7 97 2005
- [5] Stefan Hüfner, “Photoelectron Spectroscopy: Principles and Applications”, 2003
- [6] J.E. Inglesfield and E.W. Plummer, “The Physics of Photoemission”, *Studies in Surface Science and Catalysis*, Volume 74, Pages 15–61 (1992)
- [7] R.Schlaf, “Calibration of Photoemission Spectra and Work Function Determination”, <http://rsl.eng.usf.edu/Documents/Tutorials/PEScalibration.pdf>
- [8] Sir Nevill Mott, “65 years in Physics”, N.F. Mott and A.S. Alexandrov.
- [9] W.E. Spicer and C.N. Berglund, “d-Band of copper”, *Phys. Rev. Lett.* 12 9–11(1964)
- [10] C. Nordling, E. Sokolowski and K. Siegbahn, “Precision method for obtaining absolute values of atomic binding energies”, *Phys. Rev.* 105 1676–7 (1957)
- [11] Amitava Roy, Eizi Morikawa, Henry Bellamy, Challa Kumar, Jost Goettert, Victor Suller, Kevin Morris, David Ederer, John Scott, “Status of the Center for Advanced Microstructures and Devices (CAMD)”, *Nuclear Instruments and Methods in Physics Research Section A: Accelerators, Spectrometers, Detectors and Associated Equipment*, Volume 582, Issue 1, 11 November 2007, Pages 22-25
- [12] <http://www.camd.lsu.edu/news/shutdown2.htm>
- [13] <http://mcphersoninc.com/synchrotron/uhvmonochromators/nim.htm>
- [14] Yaroslav Losovyj, Ihor Ketsman, Eizi Morikawa, Zhenjun Wang, Jinke Tang, Peter Dowben, “Optimization of the 3m TGM beamline, at CAMD, for constant initial state spectroscopy”, *Nuclear Instruments and Methods in Physics Research Section A: Accelerators, Spectrometers, Detectors and Associated Equipment*, Volume 582, Issue 1, 11 November 2007, Pages 264-266

- [15] Yaroslav Losovyj, Kevin Morris, Luis Rosa, John D. Scott, Peter Dowben, High-resolution photoemission study of organic systems at the CAMD 3m NIM beamline, Nuclear Instruments and Methods in Physics Research Section A: Accelerators, Spectrometers, Detectors and Associated Equipment, Volume 582, Issue 1, 11 November 2007, Pages 258-260
- [16] B.J. Tielsch and J.E. Fulghum, "Differential Charging in XPS Part I: Demonstration of Lateral Charging in a Bulk Insulator Using Imaging XPS", Surface and Interface Analysis", Volume 24, Issue 1, pages 28–33, (1996)
- [17] T.L Barr, "Studies in differential charging", Journal of Vacuum Science & Technology A: Vacuum, Surfaces, and Films , vol.7, no.3, pp.1677-1683, May 1989
- [18] Terry L. Barr and Sudipta Seal, "Nature of the use of adventitious carbon as a binding energy standard", Journal of Vacuum Science & Technology A: Vacuum, Surfaces, and Films , vol.13, no.3, pp.1239-1246, May 1995
- [19] D.J. Hnatowich, J. Hudis, M.L. Perlman, and R.C. Ragaini, "Determination of Charging Effect in Photoelectron Spectroscopy of Nonconducting Solids", J. Appl. Phys. **42**, 4883 (1971)
- [20] Mary E. Counts, James S. C. Jen, and James P. Wightman, "Electron spectroscopy for chemical analysis study of lead adsorbed on montmorillonite" The Journal of Physical Chemistry 77 (15), 1924-1926 (1973)
- [21] G. Barth, R. Linder, C. Bryson, "Advances in charge neutralization for XPS measurements of nonconducting materials", Surface and Interface Analysis Volume 11, Issue 6-7, pages 307–311, April 1988
- [22] K.C Prince, "Improved inverse photoemission detector", Review of Scientific Instruments, vol.59, no.5, pp.741-742, May 1988
- [23] Schemm N, Balkır S and Hoffman M W 2008 IEEE Int. Symp. on Circuits and Systems (ISCAS) 2008(Seattle, WA, May 2008) pp 1866–9
- [24] Osberg K, Schemm N, Balkır S, Brand J, Hallbeck S, Dowben P and Hoffman M 2006 IEEE Sensors J. 6 1531
- [25] Matthew Newville, "Fundamentals of XAFS", Chapter 3, page 13 (2004)

Chapter 3

Sample Preparation, Crystallographic Structure and Composition

“It is most necessary to avoid rusticity in any way, whether in material, design, or execution”

-George Edmund Street-

Both experimental and theoretical insights provide evidence that these materials can form heterojunction devices. But before heading towards that goal, one must face the challenge of growing these materials on substrates. Growing the material on substrates is not enough since one must do so with the highest quality possible (by these I mean the arrangements of the atoms must be as periodic as possible). To explore these issues, we discuss the methods used for deposition of the films studied in this work and some of the experimental techniques that will allow us to determine to some extent their quality, composition and structural geometry.

From this section one can start seeing the effects that rare earth dopants have in the crystallographic structure of these semiconducting compounds by means of the local and bulk structure measurements performed.

3.1 Sample Growth Method

To paint, the painter needs to transfer the paint from the can into the surface to be coated. However the outcome depends on the medium that is used to transfer the paint. A paintbrush, a roll painter, a painting gun, even the hand will do the job, but the finish on the wall will be entirely different. Loosely speaking, the deposition process can relate to that in that it consists of taking material from one place (a source or target material) and transfers it into another place (a substrate). Vapor is usually the medium used to do the transfer, this means that these processes must evaporate the target material (material to be deposited or vaporized) and then collect it via condensation at the substrate. Although conceptually the deposition sounds like an easy task, extreme caution must be implemented as slight changes in parameters such as the chamber pressure, background gases, temperature, the material to be deposited and the method for evaporation play an important role in the process and can affect the outcome of the film deposition. This section is concerned with the growth techniques used for the deposition of thin films.

3.1.1 Hybrid plasma-assisted PVD/CVD process

The chromium doped diamond-like carbon thin films (Cr-DLC) were synthesized using the hybrid plasma-assisted PVD/CVD deposition technique by collaborators (Dr. Varshni Singh group) at Louisiana State University. A physical vapor deposition (PVD) process refers to a method for thin film deposition via the condensation of a vaporized form of the target material onto a substrate. The word “physical” stands on the fact that no chemical reaction is involved during the deposition and “vapor” due to the phase in

which the target material is present just before the deposition is performed. This type of deposition is too general so is customary to separate it in different branches as shown in Figure 3.1.1.

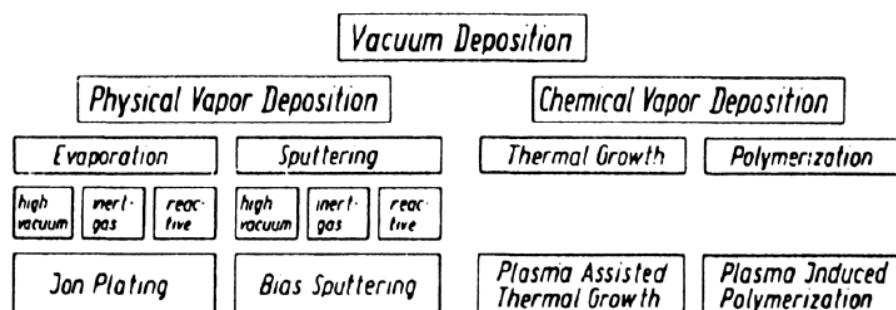


Figure 3.1.1 Survey of vacuum deposition techniques. Adapted from [1].

On the other hand, chemical vapor deposition (CVD) is the process by which one can produce films with high levels of purity via chemical reactions. This technique relies on exposing a substrate to a precursor. The target material vapor then reacts (or decomposes) with the precursor on the surface of the substrate resulting in a film. The deposition can result in a metal, semiconductor or even alloy compounds. In the hybrid plasma-assisted PVD/CVD process, the reaction is activated by creating plasma in the vapor phase. As the name suggest involves a chemical decomposition of a precursor gas and the vaporization of a target material.

The 3%, 5%, 11% 15% and 20% chromium doped diamond-like carbon thin films were grown using this technique [2-4]. Silicon (100) was used as the substrate material for the film deposition. All substrate were cleaned ultrasonically in acetone and dried in

air. Before the deposition, the chamber filled with argon several times to purge the vacuum chamber while the background pressure was pumped down to 1.33×10^{-4} Pa before each flush. The silicon substrates were sputter cleaned using ionized argon for 20 minute at 3.3 Pa with a bias voltage of 1500 V. The process involved magnetron sputtering from a Cr target (99.5% Cr) in an Ar/CH₄ discharge with a ratio of 1: 5.33 and total flow rate 47.5 sccm. The substrate was biased at -1000 V and placed 16 cm from the magnetron target. The Cr content in the Cr-DLC films was varied by operating the magnetron under current control and modulating the current between 100 mA and 350 mA, as described elsewhere [2]. The chamber pressure was maintained at 2.66 Pa. After deposition, the substrate was cooled inside the chamber in an argon atmosphere. The temperature of the substrate during deposition was maintained below 100 C. Two small areas were masked on each sample surface to determine the films thickness an optical profilometer. The carbon and chromium content in the films was determined as described in [2].

3.1.2 Pulsed Laser Deposition

The pulsed laser deposition technique (a branch under PVD deposition) consists of an incident high power pulsed laser that strikes the surface of the target material. The energy transfer between the laser and the surface will form an ablation plume that will result in the evaporation of a thin layer of the target material. This process is a non-equilibrium process since the surface (or outermost layers about 1000 Å) of the target material is extremely perturbed due to the short laser pulses (50 ns) while below is cooled.

Figure 3.1.2 show a schematic of the process. Due to the strong temperature gradient, periodic turns of material vapor are produce and deposit on the substrate material via condensation, resulting in a film with composition nearly identical of that of the target surface. This is one the reason why the PLD process is thought to be advantageous in growing thin films.

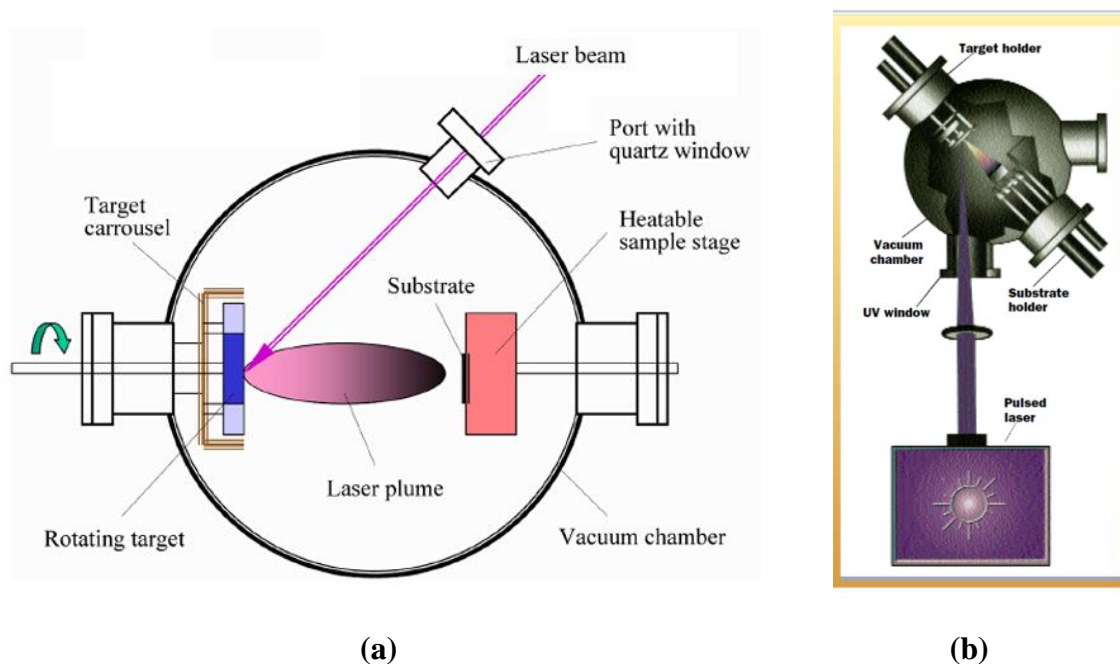


Figure 3.1.2 (a) Schematic of the pulsed laser deposition process and (b) geometrical set up inside the UHV chamber. The pictures were adapted from [5, 6].

The remaining of the samples (as shown below) used for this work were grown using PLD deposition by Professor Jinke Tang group at the University of Wyoming. These are europium oxide (EuO), gadolinium doped europium oxide (Gd:EuO), cerium doped europium oxide (Ce:EuO), gadolinium oxide (Gd_2O_3) and gadolinium doped hafnium oxide (Gd:HfO₂). The dopant content will be specified where discussed.

Gd₂O₃ and Gd:HfO₂ Compounds:

The Gd:HfO₂ films were deposited on both p-type and n-type silicon (100) substrates, at a growth rate of about 0.15 Å/s. The HfO₂ and Gd:HfO₂ targets were prepared using standard ceramic techniques (refers to the mixing of a percent of each of the powders and compress them to form a solid target) using high purity HfO₂ and Gd₂O₃ powders [7, 8]. The gadolinium concentration in these compounds was 3%, 10% and 15%. The Gd₂O₃ was grown on Si (100) using a pure Gd₂O₃ target.

Before the deposition, the Si (100) substrates were cleaned with diluted HF acid, rinsed with acetone, and then immediately put into the vacuum chamber. Before deposition, the surface of the Si substrate was sputter cleaned in a plasma of H₂ (8%) and Ar (92%) mixture created by a DC sputtering gun operating in the reverse bias mode. The chamber was pumped to a base pressure of 3×10^{-7} Torr and the deposition was carried out in a mixture of H₂ and Ar (8% H₂) to introduce the necessary oxygen vacancies. The vacuum was maintained at 10^{-5} Torr during the deposition with a substrate temperature of 500 °C. The doping level was determined from the target composition, with companion measurements using near edge X-ray absorption spectroscopy (NEXAFS), and on separate samples by X-ray emission spectroscopy (XES or EDAX) on similarly prepared samples. The complementary spectroscopies show that the films and the target have essentially the same composition.

EuO, Gd:EuO, Ce:EuO Compounds:

There are known complications to the growth of EuO on a silicon substrate. Key among the problems is that the presence of a high oxygen partial pressure at the initial

stages of the EuO film growth leads to formation of Eu^{3+} (indicative of Eu_2O_3) at the Si/EuO interface [9, 10]. Methods for preparing EuO films reported so far include reactive thermal evaporation of Eu and molecular beam epitaxy (MBE) under ultrahigh vacuum in the presence of oxygen gas [9-13]. For this work, we used pulsed laser deposition (PLD) for the growth of EuO films and EuO films with their corresponding rare earth dopant on Si (100), shown previously to be viable [14]. Hydrofluoric acid (HF) and acetone were used to clean the silicon wafers. Before the deposition, the silicon wafers were annealed at 750 °C in vacuum, at a pressure of 10^{-5} Torr of pure H_2 gas (99.995%) to reduce the native SiO_2 surface layer from the wafers. All samples were grown on these wafers using PLD at room temperature. The targets used in the PLD process were either Eu (99.9%), Ce (99.9%) or Gd (99.9%) metal or a mixture of Eu with Gd (or Ce (99.9%)), as described previously [14]. We chose the gadolinium substitution level of 4% which was reported optimal [11].

3.2 Studies of the Crystallographic and Local Structure using X-ray Absorption Fine Structure and X-ray Diffraction

A building consist of two infrastructures; the frame or foundation in which the whole support relies, and the design which assign a space, form and shape of the frame. An architect is a person who plans, designs and supervised the construction of a building. Its job is to ensure that its employee's ensemble the building piece by piece by rigorous implementation of the blueprints. A similar situation happens with a film or material after deposition. A film is compose of a lattice (periodic arrange of points that follow some symmetry) and a basis which is the specific atom or molecule that is assign to each point. In this sense, a material scientist plays “sort of” the same role as the architect but in the

microscopic world. Once the deposition is performed, knowledge of the crystallographic structure (building's frame) and its local environment (building design) is necessary for characterization of the films. Unfortunately, due to lack of human perception at small scales, a material scientist can only study the structure and local environments of films by means of experimental techniques such as the ones discussed in [Section 2.4](#).

Following that line, x-ray absorption near edge Structure and extended x-ray absorption fine structure were implemented to study the local structure of Cr-DLC and Gd:HfO₂ films. The measurements were done at the Center for Advanced Microstructures and Devices (CAMD) synchrotron facility. The data was collected at the DCM beamline and monochromatic light was obtained by using a double crystal monochromator of Lemonnier type [15]. The energy resolution was approximately 2.0 eV and spectra were acquired in the fluorescent yield mode, using a Ge detector (Canberra).

X-ray diffraction provided evidence of the effects in the crystallographic structure cause by the dopant inclusion. The most remarkable effects are seen in Gd:HfO₂ in which a change in crystal structure is evident as the dopant concentration increases, and in Gd:EuO in which the crystal structure remain invariant but the direction of growth along a very unstable surface is preferred.

3.2.1 The local structure of amorphous Diamond like Carbon doped with Chromium

The x-ray absorption (XAS) data at the K- edge of Cr (5989.2 eV) was collected using a monochromatic X-ray beam from the Synchrotron source in CAMD. The incident beam intensity (I_0) was monitored with an ionization chamber. XAS spectra were recorded in fluorescence mode for the Cr-DLC films using a 13 element germanium

detector. EXAFS spectra were recorded over an energy range of 5700 – 6970 eV with 1 eV steps and XANES spectra were recorded from 5910 – 6400 eV with 0.2 eV steps in the near edge region. Data for pure Cr and Cr₃C₂ (standards) were recorded in transmission detection mode.

XANES data were fitted with a linear pre-edge for background removal and normalized to the 6300 - 6400 eV post-edge regions of the spectra using the WinXAS software package [16, 17]. The EXAFS data were extracted and analyzed utilizing the UWXAFS software package [15]. The position of the adsorption edge E_0 was set at the first inflection point of the Cr spectrum, and the extracted EXAFS signal was Fourier transformed over the region of 2.0 Å⁻¹ to 11 Å⁻¹, using a Hanning window function. Refined structural parameters were obtained from nonlinear least square fitting in R-space over a range of 1.2 Å to 3.0 Å, encompassing the first two peaks representing Cr...C and Cr...Cr, in the single scattering approximation. Theoretical phase and amplitude functions were calculated using FEFF8, a computer program for *ab initio* calculation of EXAFS and XANES spectra using multiple-scattering theory [16]. The amplitude reduction factor S^2_0 was determined by fitting the EXAFS data of the Cr₃C₂ powder standard yielding a value of 0.72.

XANES spectra were obtained from selected Cr-DLC films with Cr content of about 1 %, 0.4 %, 1.5 %, 2.8 % and 11.8 % along with pure Cr, Cr-III oxide (Cr₂O₃) and Cr carbide (Cr₃C₂) samples are shown in [Figure 3.2.1](#). The chemical state of the absorbing atom determines the position of the absorption edge, E_0 (5989.2 eV for Cr). This is usually defined as the first inflection point in the absorption spectrum. We know that Cr is in a neutral state in metallic Cr, in the Cr (III) oxidation state in Cr₂O₃ and probably bracket the oxidation state of chromium in Cr₃C₂, consistent with the near-edge

absorption spectra of Figure 3.2.1. Therefore, as expected, Figure 3.2.1 shows that the chemical state of the absorbing Cr atom is different in metallic Cr, Cr_3C_2 and Cr_2O_3 , in agreement with data reported by Pantelouris et al. [18] and prior work [30]. The pre-edge structure for the Cr-DLC films is similar to that observed in Cr_3C_2 (but not in Cr). This suggests that the Cr atom in these films has a chemical state similar to the state of Cr in Cr_3C_2 . These results [30] are in agreement with those reported by Singh and Meletis [19], where the TEM observations on Cr-DLC film with 4.8 at.% Cr showed crystalline nanoclusters, 2–5 nm in size, embedded in the amorphous matrix. This result differs somewhat from the work of Gassner et al. [20] on Cr-doped films of amorphous hydrogenated carbon made via unbalanced dc magnetron sputtering, where the as-deposited films contain a metastable fcc CrC which transforms into Cr_3C_2 and Cr_7C_3 precipitates upon annealing.

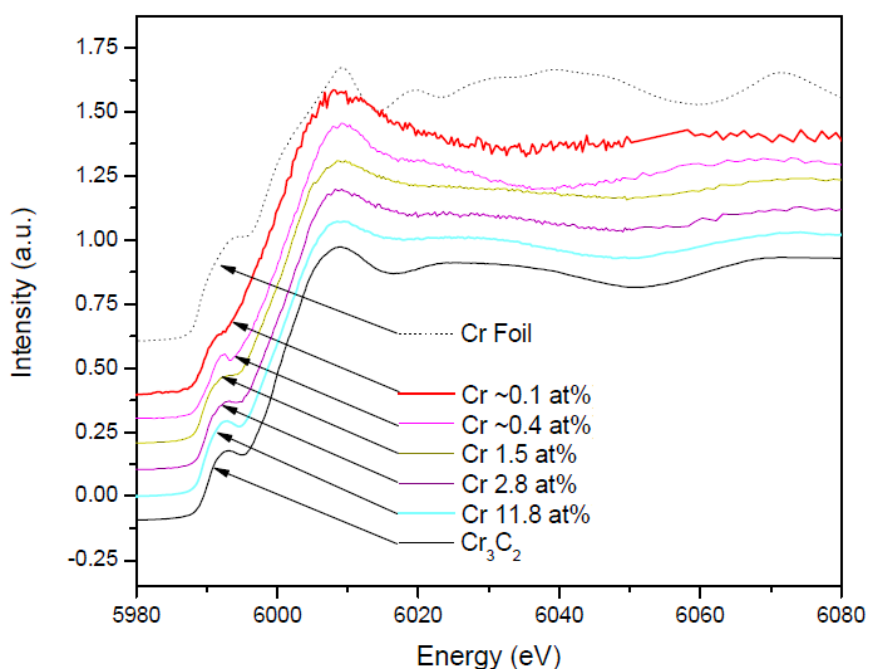


Figure 3.2.1 The X-ray absorption near-edge structure (XANES) spectra for the Cr-DLC films along with pure Cr and Cr carbide (Cr_3C_2). The spectra are normalized and translated along the y-axis (intensity) for clarity.

The analysis of the XANES spectra of the Cr-DLC films shows that the chemical state and the local environment around the absorbing Cr atoms remains essentially the same in the films with Cr content ≥ 1.5 %. With lower Cr content (0.4 and 0.1 at.%), a different local environment compared to that in the rest of the Cr-DLC films and Cr_3C_2 is evident [30]. It was also observed that the amplitude of the white line increases with diminishing Cr content in the films. This increase suggests a decrease in the electron density around the absorber atom and can be attributed to the sharing of electrons by the Cr atoms, present on the interface of nanoclusters, and the hydrogenated carbon in the matrix. The nanocluster size is expected to decrease with decreasing the Cr content resulting in the increase in the surface to volume Cr atom ratio. Indeed, the reduction in size of metal nucleated nanocluster inclusions, with decreasing metal content has been observed and reported for Co-DLC [21], Co-C [22] and Ti-DLC [23] as well as Ti-doped amorphous-C [24], Ni-doped amorphous-C [25, 26]. If such a surface effect plays a dominant role in changing the shape of XANES spectra with changing Cr content in the films, Figure 3.2.2 illustrates the Fourier transform of the extended X-ray absorption (EXAFS) spectra of Cr carbide and Cr-DLC films. The spectra of the films with relatively higher Cr content (11.8 and 2.8 at.%) show two peaks (1.5 and 2.1 Å) corresponding to the two sub-shells (Cr . . C and Cr . . Cr) of the first coordination shell [30]. No significant features were observed above 2.6 Å in the radial distribution curves (Figure 3.2.2). This absence of an indication of order suggests a highly disordered (amorphous) structure with short-range order that is mainly limited to the first coordination shell. The spectrum for the Cr carbide shows a shoulder around the same distance as the first peak of the films. This is mostly due to the contribution from Cr . . C bonds. The main peak centered around 2.0 Å shows the contribution mainly from the Cr . . Cr bonds. The second peak of the films with 1.5

% and 0.4 % of chromium drifts to the right side and is at 2.2 and 2.5 Å, respectively. Since the Cr . . . Cr bond lengths are nearly the same (Table 3.2.1), this could be attributed to the artifacts introduced due to higher noise level in the EXAFS spectra of these films.

The first sub-shell conforms to Cr . . . C bond contributions.

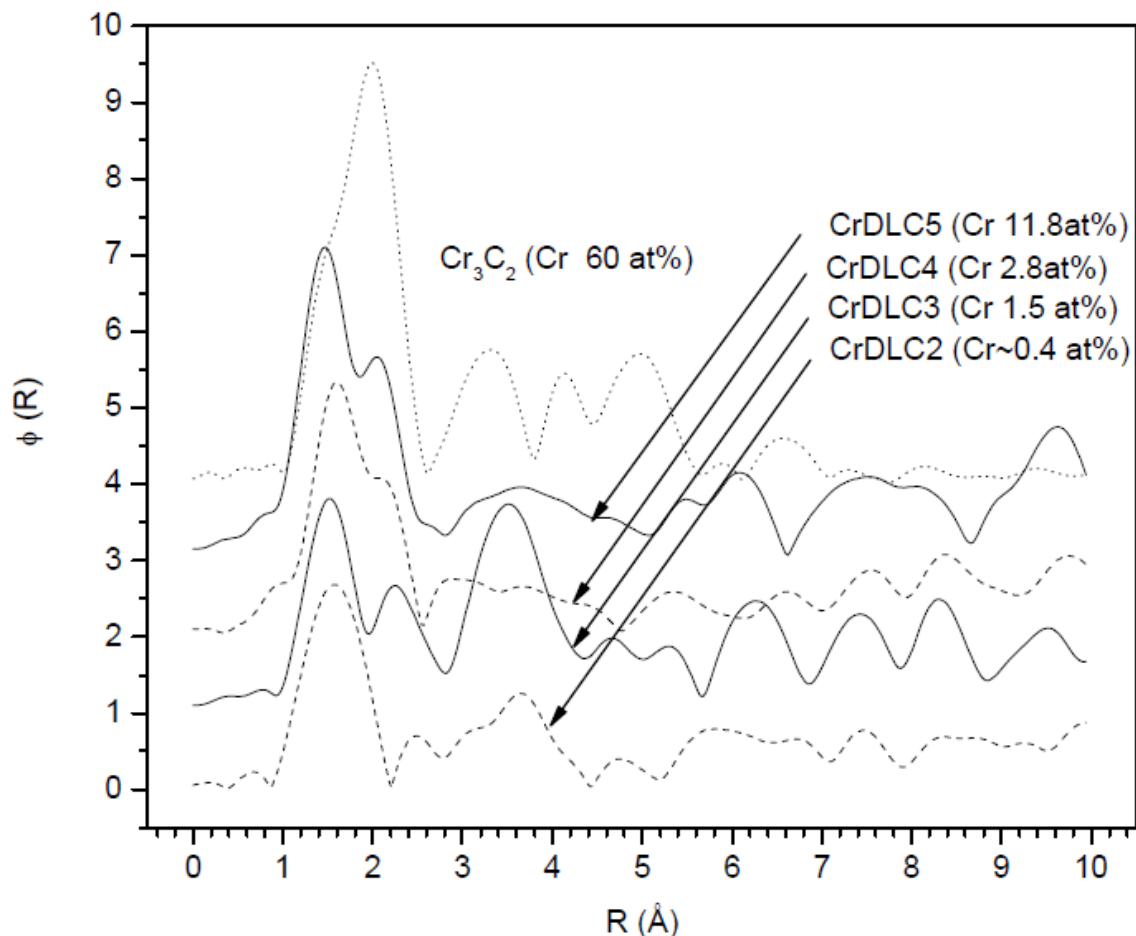


Figure 3.2.2 The Fourier transform of the extended X-ray absorption fine structure spectra (EXAFS) for the Cr-DLC films along with pure Cr carbide (Cr_3C_2). The spectra are translated along the y -axis (intensity) for clarity.

The corresponding coordination number (number of nearest C neighbors) remains nearly constant (around 4.0) with decreasing Cr content except for the film with ~0.4 % Cr. In the latter film, the coordination number increases significantly (becomes 6.6), indicating a breakdown of the carbide structure and dispersion of the Cr atoms in the matrix. Also, the bond length is nearly the same for all the films and is similar to that of Cr_3C_2 powder.

Sample	Model Fit [30]	$N_{\text{Cr-C}}$	$R_{\text{Cr-C}} (\text{\AA})$	$N_{\text{Cr-Cr}}$	$R_{\text{Cr-Cr}} (\text{\AA})$
Cr_3C_2		4.0 ± 0.0	2.20 ± 0.0	11.0 ± 0.0	2.70 ± 0.0
Cr/C 0.007; 0.4% Cr		6.6 ± 0.67	2.25 ± 0.01	2.0 ± 0.92	2.76 ± 0.1
Cr/C 0.030; 1.5% Cr		3.6 ± 0.4	2.17 ± 0.013	3.2 ± 0.58	2.77 ± 0.01
Cr/C 0.050; 2.8% Cr	70% Cr_3C_2 and 30% of 0.1 at% Cr film.	3.9 ± 0.56	2.25 ± 0.04	4.2 ± 0.82	2.79 ± 0.06
Cr/C 0.230; 11.8% Cr	87% Cr_3C_2 and 13% of 0.1 at% Cr film	3.9 ± 0.3	2.18 ± 0.01	5 ± 0.7	2.75 ± 0.01

Table 3.2.1 Structural parameters for Cr-DLCs and Cr_3C_2 obtained from curve fitting Sample Model fit [30]

3.2.2 Gadolinium Occupancy in Semiconducting Hafnium Oxide

Gd L_3 edge x-ray adsorption near edge structure (XANES) and extended x-ray absorption fine structure (EXAFS) spectra of 3% doped sample were collected. Magnitude and imaginary part of the Fourier transformed (FT) $k\chi(k)$ of the Gd L_3 edge for 3% samples is shown in [Figure 3.2.3](#). While the magnitude of the Fourier transformed $k\chi(k)$ is not precisely the pair radial distribution function, this does provide an indication of the radial spacing of atoms in the vicinity of Gd. The first peak at $\sim 0.8\text{--}2.5 \text{\AA}$ corresponds to the single scattering contribution of Gd–O pairs. A multi-peak structure at $\sim 2.5\text{--}5.2 \text{\AA}$ is due to combined contributions of Gd–O, and Gd–Hf single-scattering paths as well as several multiple scattering paths, as summarized in [Figure 3.2.4](#).

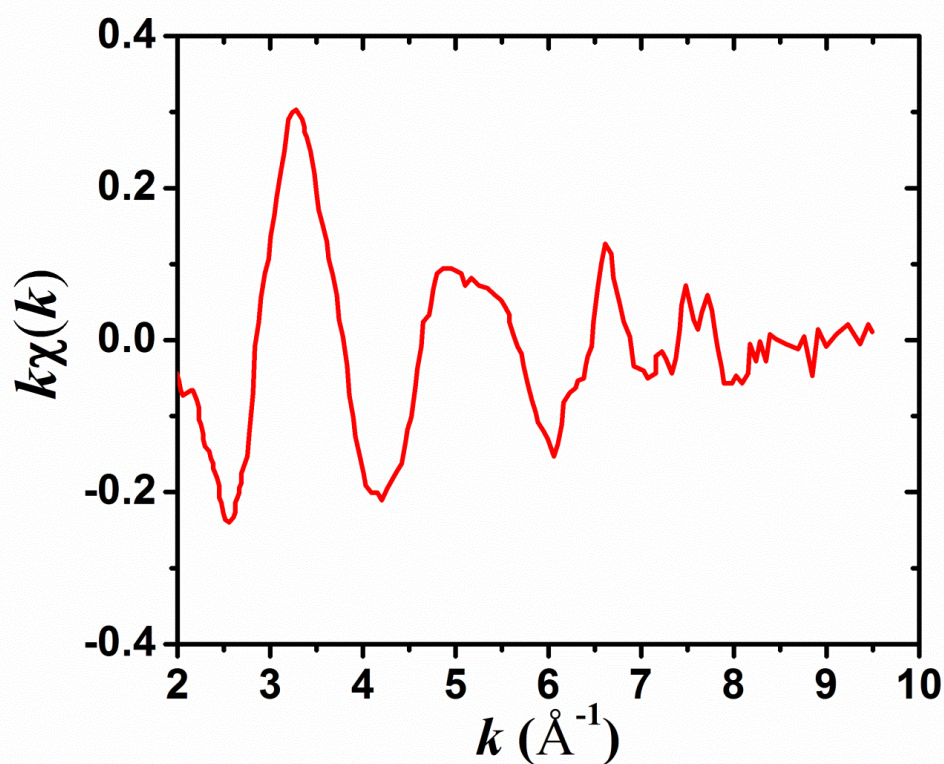


Figure 3.2.3 (a) The $k\chi(k)$ of 3% Gd doped HfO_2 extracted from the Gd L_3 -edge EXAFS spectra.

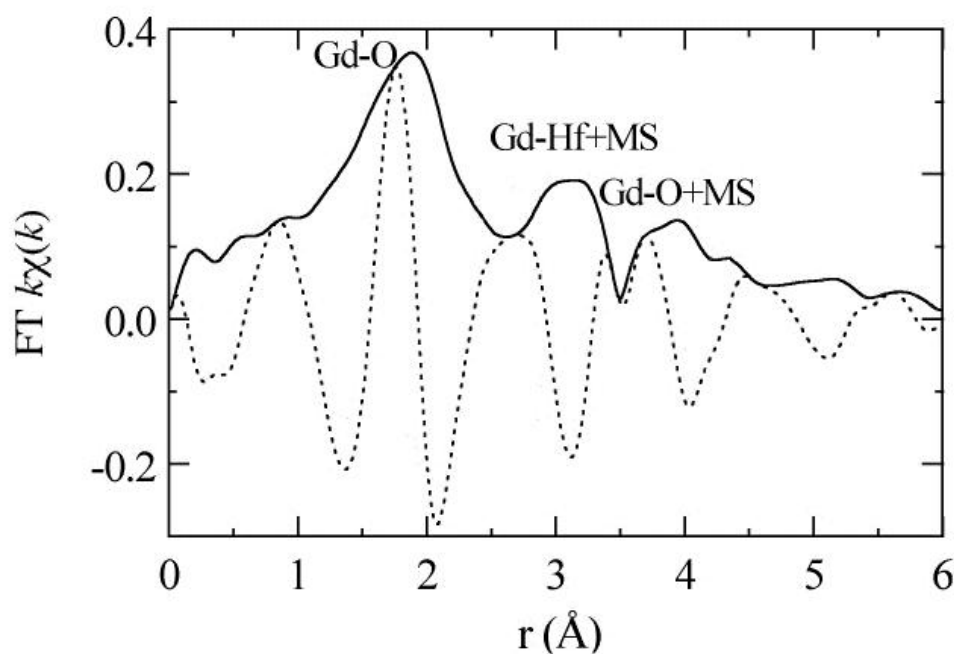


Figure 3.2.4. The Fourier transform (FT) of 3% Gd-doped HfO_2 EXAFS data. The oscillating curve (dashed lines) is the imaginary part of the Fourier transform of the data. The envelope (solid lines) are the magnitudes of the Fourier transform. The 3% data are transformed with a square window between 2.8 and 9.4 \AA^{-1} . The peak assignment is based on HfO_2 .

In other words, we find that Gd occupies the Hf site in HfO_2 , consistent with expectations [27, 7].

3.2.3 Structural phase transition in Gd:HfO₂

X-ray diffraction (XRD) provides evidence of the Gd doping effects in the structure of the Gd:HfO₂ films as shown in Figure 3.2.5. At low doping concentrations (3%), the structure crystallize in the monoclinic structure as determined by the scattering angle at 28° and with texture along the (-111) crystallographic plane. With an increased level of 10% Gd doping, a new cubic structural phase is seen as indicated by the XRD feature at an angle of 29.2° with strong textured along (111) direction, still retaining a small component of the monoclinic phase.

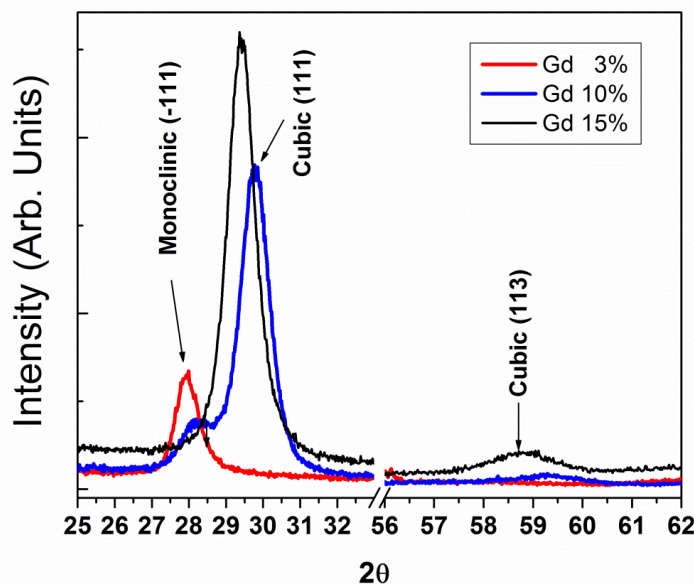


Figure 3.2.5 Part of the XRD pattern for 3%, 10%, and 15% Gd doped HfO₂. The 3% Gd doped films are consistent with that of the HfO₂ in a simple monoclinic structure. The 10% doped samples are mixed monoclinic and majority cubic phases, as indicated, while 15% Gd-doped samples are in a fluorite phase. In the fluorite fcc phase, the lattice constant increases with increased Gd doping. Taken from [28].

For a doping level of 15% Gd, no monoclinic phase is visible in the XRD spectra, consistent with the face centered cubic fluorite phase in XRD.

3.2.4 Comparison of Gd:HfO₂ and Gd₂O₃ Monoclinic Crystal Structure

Both X-ray diffraction and extended X-ray adsorption fine structure spectroscopy show that 3% Gd doped HfO₂ films and Gd₂O₃ films grown on Si (100) are highly textured. As noted above, the X-ray diffraction patterns show that the resulting approximately 250 nm thick 3% Gd doped HfO₂ films are in a single monoclinic phase with strong texture growth, with about 3% strain compared with the undoped HfO₂ (Figure 3.2.6 (a)) [12,15]. From the largest peak near 28 degree (2 θ), it is estimated that the lattice spacing for (-111) is increased by $d = 0.0030$ nm, from 0.3147(1) nm for the undoped HfO₂ films to 0.3177(1) nm for Gd-doped samples (Figure 3.2.5). The peak is shifted to lower angles by 0.338°. For Gd₂O₃, the X-ray diffraction is consistent with highly textured monoclinic Gd₂O₃, not the more expected cubic structure [28, 29]. But the substrate has a strong influence on the texture and crystal structure of the Gd₂O₃ film [30, 31], as is clearly the case here. The textured structure is such that the (-402) planes mostly lie along the surface of the film. Some (401) and (202) planes are also found to orient parallel to the surface of the film. Only the (h0l) planes (planes parallel to the b axis) are grown parallel to the surface. The lattice spacing along the <-402> direction is about 0.2965 nm and the lattice spacing for <401> and <202> is 0.3033 nm and 0.3402 nm, respectively. The Gd₂O₃ unit cell is large with inequivalent Gd (three) and oxygen atoms (in a number of inequivalent sites) as schematically shown in Figure 3.2.6 (b). The repeat along the surface normal is eight times the (-402) layer spacing or about 2.372 nm

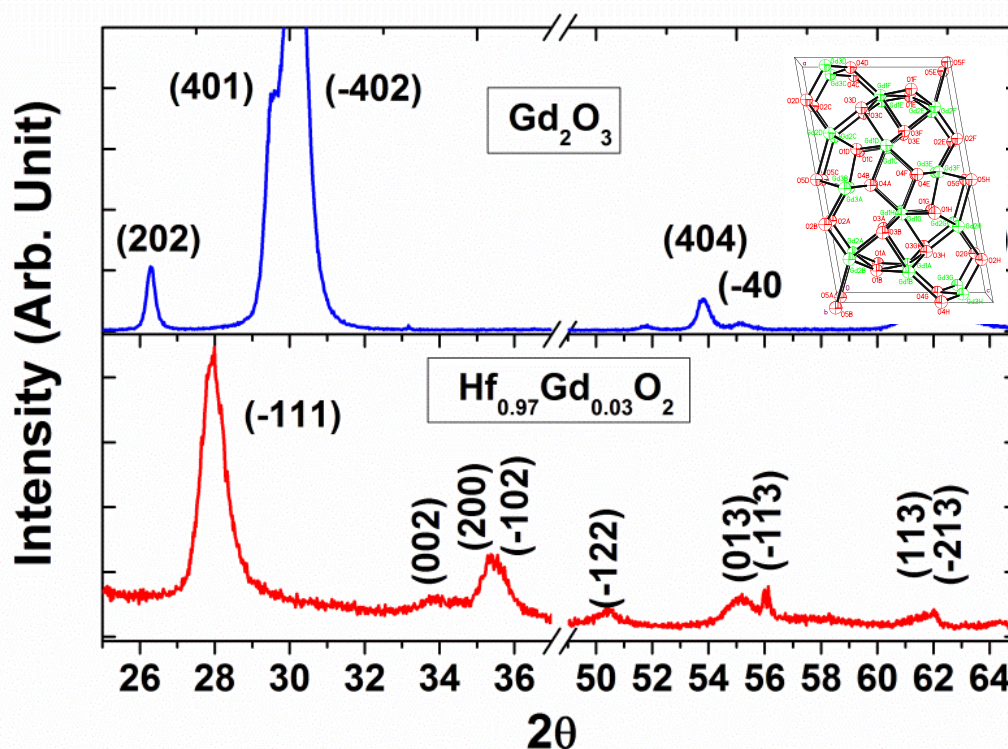


Figure 3.2.6 (a) Part of the XRD pattern of the film is shown in figure. X-ray diffraction patterns of PLD grown Gd_2O_3 (upper panel) and 3% Gd doped HfO_2 (lower panel). The bar diagrams included in each panel are the standards of monoclinic Gd_2O_3 and HfO_2 , respectively. For 3% Gd doped HfO_2 (lower panel), the XRD is consistent with that of HfO_2 in a simple monoclinic structure. (inset) Structure of Gd_2O_3 , with the packing of the ions in Gd_2O_3 as viewed along the b -axis. The green and red spheres represent gadolinium and oxygen atoms respectively. The Gd .. Gd interactions are not shown.

3.2.5 The (111) polar Surface in Gd:EuO

The XRD provides an excellent indication that both the EuO and Gd doped EuO films are high quality europium oxide films. Figure 3.2.7 shows the XRD patterns of both EuO and Gd:EuO films. No impurity phase was observed in either the EuO or the Gd:EuO films, where the substrates were annealed at 750 °C for a shorter time. For The Gd:EuO films, there is evidence of silicide formation as peaks of EuSi were observed in some films [see Fig. 3.2.7 (a)]. The substrates were annealed at 750 °C for a longer time for these oxygen deficient films. Europium in the laser-induced plume tends to react with

Silicon to form EuSi_2 , in this case because it is less likely to have residual SiO on the surface of the substrates that prevents the reaction of Eu and Si .

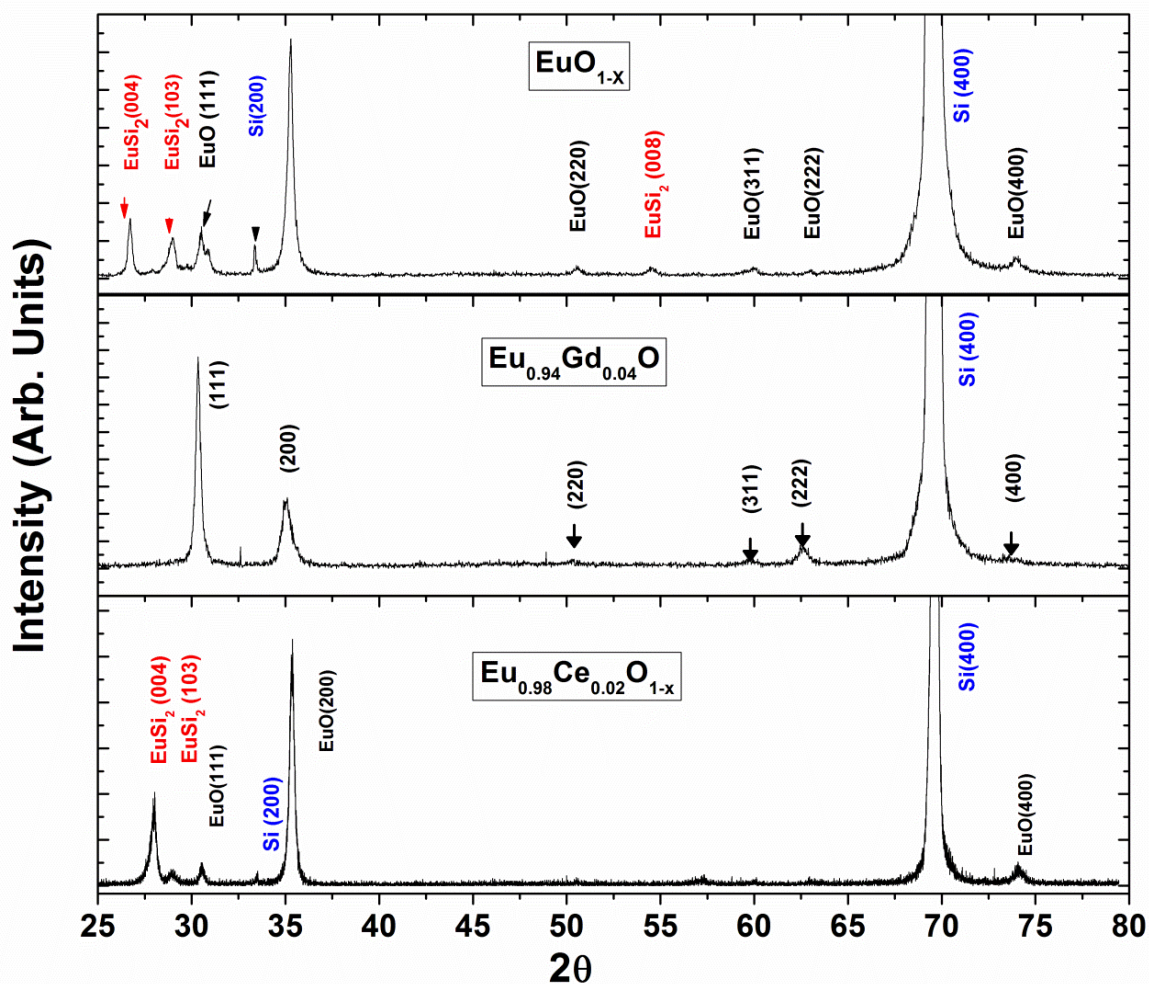


Figure 3.2.7 X-ray-diffraction pattern for PLD-grown (a) EuO , (b) Gd-doped EuO films on $\text{Si}(100)$ and (c) $\text{Ce}:\text{EuO}$.

As can be seen, for the EuO_{1-x} films, the XRD is dominated by the (200) diffraction line as expected from prior work [32, 33]. For the $\text{Eu}_{0.96}\text{Gd}_{0.04}\text{O}$ films the dominant XRD feature is (111) indicating that the preferential texture growth has altered with just this small amount of Gd doping. The lattice constants determined from the (200)/(111) peaks for the Gd-doped, oxygen deficient, and stoichiometric EuO are consistent with the presence of Gd and O vacancies. While $a = 0.5131$ nm for EuO , this lattice constant

decreases to 0.5106 nm for EuO_{1-x} . Upon Gd doping, the unreduced sample $\text{Eu}_{0.96}\text{Gd}_{0.04}\text{O}$ has a lattice constant of nm because of the smaller Gd radius, but this value decreases further to 0.5091 nm for $\text{Eu}_{0.96}\text{Gd}_{0.04}\text{O}$ when the film is oxygen deficient. Evidently 4% Gd doping induces a 0.0013–0.0015 nm reduction in the lattice parameter while oxygen vacancies independently result in a reduction of 0.0025–0.0027 nm. While the changes in lattice constant are expected from lattice change, the changes in texture growth are a little unusual, but could be the result of a change in interfacial strain, although small. Although we do not believe these changes are a result of a crystallographic phase change, as with the inclusion of 4% of Gd in the cubic (Fm3m) lattice EuO is expected to remain a soluble random alloy of the same crystal structure [34], such a possibility cannot be ruled out. We find no evidence of Eu metal either as bulk precipitates or at the surface in either XRD or x-ray photoemission in any of our samples.

As shown in [Figure 3.2.7 \(c\)](#), the XRD pattern of $\text{Eu}_{0.98}\text{Ce}_{0.02}\text{O}_{1-x}$ is consistent with a film having the fcc rock salt crystal structure expected of EuO. It shows that the stacking planes are mostly aligned with the $\langle 200 \rangle$ orientation as reported from prior works [5,11] The XRD provides a good indication that the Ce:EuO film is of high quality and strongly textured. As in the case of EuO and Gd:EuO, there is evidence of silicide formation as peaks of EuSi_2 were observed in the film. The lattice constants a determined from the (200) peaks for $\text{Eu}_{0.98}\text{Ce}_{0.02}\text{O}_{1-x}$ are consistent with the presence of Ce. While a = 0.5131 nm for EuO, this value decreases to 0.5105 nm for $\text{Eu}_{0.98}\text{Ce}_{0.02}\text{O}_{1-x}$ because of the smaller Ce^{3+} radius and oxygen deficiency. Because the doping level for Ce used here is a little lower than the Gd doping level, and because the radius of Ce^{3+} is a little larger than that of Gd^{3+} , the lattice constant of $\text{Eu}_{0.98}\text{Ce}_{0.02}\text{O}_{1-x}$ is larger than that of Gd doped EuO_{1-x} .

As a closing note, one might wonder why the Gd:EuO textured changes with a small inclusion of Gd. Moreover, why would the films grows along the (111) polar surface, which is known to be an energy expensive and very unstable surface. Cerium is expected to have similar valency as gadolinium, yet, the effects in the textured growth are completely different. Free carriers are known to screen the electrostatic field in these types of surfaces for metallic films, but in a semiconductor or insulator (such as EuO) this is very unlikely. Would it be that 4% of Gd doping drives the system to a nonmetal to metal transition?

References

- [1] Schiller, O. Heisig and K. Geodick, Proc. 7th Int'l. Vacuum Congress, p. 1545, Vienna (1977)
- [2] V. Singh, V. Palshin, R.C. Tittsworth, E.I. Meletis, "Local structure of composite Cr-containing diamond-like carbon thin films", Carbon 44, 1280 (2006)
- [3] X. Fan, E.C. Dickey, S.J. Pennycook, M.K. Sunkara, "Z-contrast imaging and electron energy-loss spectroscopy analysis of chromium-doped diamond-like carbon films", Appl. Phys. Lett. 75, 2740 (1999)
- [4] A.A. Adjaottor, E. Ma, E.I. Meletis, "On the mechanism of intensified plasma-assisted processing", Surf. Coat. Technol. 89, 197 (1997)
- [5] http://groups.ist.utl.pt/rschwarz/rschwarzgroup_files/PLD_files/PLD.htm
- [6] T. Venkatesan and Steven M. Green, "Pulsed Laser Deposition: Thin Films in a Flash", American Institute of Physics 1996.
- [7] I. Ketsman, Ya. B. Losovyj, A. Sokolov, J. Tang, Z. Wang, K.D. Belashchenko and P.A. Dowben, "The n-type Gd-doped HfO₂ to silicon heterojunction diode", Appl. Phys. A 89 489–92 (2007)
- [8] W. Wang, Y. Hong, M. Yu, B. Rout, G.A. Glass and J. Tang. "Structure and magnetic properties of pure and Gd-doped HfO₂ thin films", J. Appl. Phys. 99 (2006)
- [9] A. Schmehl, V. Vaithyanathan, A. Herrnberger, S. Thiel, C. Richter, M. Liberati, T. Heeg, M. Röckerath, L. F.Kourkoutis, S.M.ühlbauer, P. Boni, D. A. Muller, Y. Barash, J. Schubert, Y. Idzerda, J. Mannhart, and D. G. Schlom, "Epitaxial integration of the highly spin-polarized ferromagnetic semiconductor EuO with silicon and GaN", Nat. Mater. 6, 882 (2007).
- [10] R. P. Panguluri, T. S. Santos, E. Negusse, J. Dvorak, Y. Idzerda, J. S. Moodera, and B. Nadgorny, "Half-metallicity in europium oxide conductively matched with silicon", Phys. Rev. B 78, 125307 (2008).
- [11] H. Ott, S. J. Heise, R. Sutarto, Z. Hu, C. F. Chang, H. H. Hsieh, H.-J. Lin, C. T. Chen, and L. H. Tjeng, "Soft x-ray magnetic circular dichroism study on Gd-doped EuO thin films", Phys. Rev. B 73, 094407 (2006).
- [12] K. Sattler and H. C. Siegmann, "Paramagnetic Sheet at the Surface of the Heisenberg Ferromagnet EuO", Phys. Rev. Lett. 29, 1565 (1972).

- [13] P. G. Steeneken, L. H. Tjeng, I. Elfimov, G. A. Sawatzky, G. Ghiringhelli, N. B. Brookes, and D.-J. Huang, "Exchange Splitting and Charge Carrier Spin Polarization in EuO", *Phys. Rev. Lett.* 88, 047201 (2002).
- [14] X. Wang, P. Liu, K. A. Fox, J. Tang, J. A. Colón Santana, K. Belashchenko, P. A. Dowben, and Yu Sui, "Effects of Gd Doping and Oxygen Vacancies on the Properties of EuO Films Prepared via Pulsed Laser Deposition", *IEEE Trans. Magn.* 46, 1879 (2010).
- [15] M. Lemonnier, O. Collet, C. Depautex, J.M. Esteva and D. Raoux, "High vacuum two crystal soft X-ray monochromator", *Nucl. Instrum. Methods A* 152 109 (1978)
- [16] T. Ressler, "WinXAS: A New Software Package not only for the Analysis of Energy-Dispersive XAS Data", *J. Phys. IV* 7, C2 (1997)
- [17] E.A. Stern, M. Newville, B. Ravel, Y. Yacoby, D. Haskel, "The UWXAFS analysis package: philosophy and details" *Physica B* 208–209, 117 (1995)
- [18] A. Pantelouris, H. Modrow, M. Pantelouris, J. Hormes, D. Reinen, "The influence of coordination geometry and valency on the K-edge absorption near edge spectra of selected chromium compounds", *Chem. Phys.* 300, 13 (2004)
- [19] V. Singh, J.C. Jiang, E.I. Meletis, "Cr-diamondlike carbon nanocomposite films: Synthesis, characterization and properties", *Thin Solid Films* 489, 150 (2005)
- [20] G. Gassner, P.H. Mayrhofer, J. Patscheider, C. Mitterer, "Thermal stability of nanocomposite CrC/a-C:H thin films", *Thin Solid Films* 515, 5411 (2007)
- [21] F.L. Wang, J.C. Jiang, E.I. Meletis, "Vortex motion in $\text{YBa}_2\text{Cu}_3\text{O}_{7-\delta}$ twinned single crystals and epitaxial films", *J. Appl. Phys.* 95, 2569 (2004)
- [22] V.G. Palshin, R. Tittsworth, J. Hormes, E.I. Meleis, X. Nie, J. Jiang, H. Modrow, in *Proceedings of the International Workshop*, Old Dominion University (2002)
- [23] W.J. Meng, R.C. Tittsworth, J.C. Jiang, B. Feng, D.M. Cao, K. Winkler, V. Palshin, "Ti atomic bonding environment in Ti-containing hydrocarbon coatings", *Appl. Phys.* 88, 2415 (2000)
- [24] S. Zhang, X.L. Bui, Y. Fu, "Magnetron-sputtered nc-TiC/a-C(Al) tough nanocomposite coatings", *Thin Solid Films* 467, 261 (2004)
- [25] G.Y. Chen, J.S. Chen, Z. Sun, Y.J. Li, B.K. Tay, J.W. Chai, "Field emission properties and surface structure of nickel containing amorphous carbon", *Appl. Surf. Sci.* 180, 185 (2001)

- [26] J.S. Chen, S.P. Lau, Z. Sun, G.Y. Chen, Y.J. Li, B.K. Tay, J.W. Chai, *Thin Solid Films* 398–399, 110 (2001)
- [27] Ya. B. Losovyj, I. Ketsman, A. Sokolov, K.D. Belashchenko, P.A. Dowben, J. Tang and Z. Wang, “The electronic structure change with Gd doping of HfO₂ on silicon”, *Appl. Phys. Lett.* 91 132908 (2007)
- [28] Haire G and Eyring L 1994 *Handbook on the Physics and Chemistry of Rare Earths* vol 18 (London: Elsevier) p 429
- [29] N. Horosaki, S. Ogata and C. Kocer, “Ab initio calculation of the crystal structure of the lanthanide Ln₂O₃ sesquioxides”, *J. Alloys Compounds* 351 31
- [30] M. Hong, J. Kwo, A.R. Kortan, J.P. Mannaerts and A.M. Sergent, “Epitaxial Cubic Gadolinium Oxide as a Dielectric for Gallium Arsenide Passivation”, *Science* 283 1897 (1999)
- [31] Y. Yacoby, M. Sowwan, E. Stern, J.O. Cross, D. Brewes, R. Pindak, J. Pitney, E.M. Dufresne and R. Clarke, “Direct determination of epitaxial interface structure in Gd₂O₃ passivation of GaAs”, *Nat. Mater.* 1 99 (2002)
- [32] A. Schmehl, V. Vaithyanathan, A. Herrnberger, S. Thiel, C. Richter, M. Liberati, T. Heeg, M. Röckerath, L. F. Kourkoutis, S. Mühlbauer, P. Böni, D. A. Müller, Y. Barash, J. Schubert, Y. Idzerda, J. Mannhart, and D. G. Schlom, “Epitaxial integration of the highly spin-polarized ferromagnetic semiconductor EuO with silicon and GaN”, *Nat. Mater.*, vol. 6, p. 882, 2007.
- [33] J. Lettieri, V. Vaithyanathan, S. K. Eah, J. Stephens, V. Sih, D. D. Awschalom, J. Levy, and D. G. Schlom, “Epitaxial growth and magnetic properties of EuO on (001) Si by molecular-beam epitaxy”, *Appl. Phys. Lett.*, vol. 83, p. 975, 2003.
- [34] J.M. An, S.V. Barabash, V. Ozolins, M. van Schilfgaarde and K.D. Belashchenko, “First-principles study of phase stability of Gd-doped EuO and EuS”, *Phys. Rev. B* 83, 064105 (2011)

Chapter 4

Magnetoresistive Effects in Chromium doped Diamond-like Carbon Heterostructure

“Anything that won't sell, I don't want to invent. Its sale is proof of utility, and utility is success”

-Thomas A. Edison -

How far can one go in making devices from local moment semiconductors? While the emphasis of this thesis is on rare earth doped semiconductors (with huge local moments, $7.3 \mu_B$ in the case of gadolinium), as a starting point we have fabricated a “demonstration” device from diamond like materials, more specific, from chromium carbide alloys, which potential relies in the manipulation of its local magnetic moments while preserving its semiconducting properties. This material serves as a trailer for a device, which if engineered adequately, might lead to promising applications in spintronics research. Nonetheless, as noted in the introduction, fundamental understanding is a paramount issue.

How to gain that fundamental understanding? The approach, as discussed in the later chapters is to look at systems with well-behaved band structures where nominal chemical valancing can be used to alter the doping of the semiconductor. Yet, an example of what may well be possible in devices that are reliable and in materials that are perhaps slightly more conventional is provided in this chapter. In the context of this work, Cr-DLC should be perceived as an exemplary tale of a local magnetic moment system and a success in a device with magnetoresistive effects at room temperature.

4.1 Why Studying Chromium doped Diamond-like Carbon?

The study of doped semiconductors has attracted considerable interest, but the doping of a wide band gap insulator (like diamond) offers an opportunity to increase the coupling of magnetic impurities. If the medium of exchange is mediated by the overlap of defect states, then a quasi-low K dielectric with large band gap will decrease the effective defect wave function radius in the context of the magnetic polaron model [1-4]. Thus for a smaller-K dielectric as the host semiconductor, more local moments can be introduced into the host semiconductor without over doping of the semiconductor. In the most simplistic view, the effective Bohr radius of the impurity defect scales proportionally with the dielectric constant, expected to be about 5.6 for diamond-like (chemical vapor deposition) films [5,6]. This means that diamond-like films are not a high-K dielectric material per se, but the propensity to form defects and accommodate large transition metal concentration means the spin polarization extinction length could be quite large, if mediated by the defects [2-4], without completely destroying the useful semiconductor properties. In addition, local wave functions for impurities could lead to a sort of weak clustering of impurities [3, 7-9], as is observed with Cobalt in semiconducting boron carbides [7-9]. The pairing of the cobalt atoms in the semiconducting boron carbides, but not in close proximity, suggests a role for strain or extended orbitals [5-8]. Other semiconductors could exhibit similar effects; for example, $\text{HgBa}_2\text{CuO}_4$ seems to involve orbitals that extend beyond third-nearest-neighbor atoms [10].

Chromium is a successful magnetic impurity in a number of semiconductors [11-22]. If chromium is a successful dopant in diamond-like carbon films, two questions surface, beyond those related to the question of the majority carrier introduced by chromium doping or questions related to magnetic ordering: is the doping random, i.e. dilute [23-24]; are the impurities weakly clustered as in Co-doped semiconducting boron carbides [7-9] or do the dopants cluster more strongly as has been observed for cobalt dopants in some oxide dielectrics [25-29]?

Doping of diamond-like carbon (DLC) films with metals could create a two dimensional array of nanoclusters within the DLC matrix or an atomic- scale composite (solid solution in the DLC matrix). Clustering of chromium impurities is expected with chromium doping in diamond-like films at with high concentrations ($\geq 1.5\%$) [30], although Fan et al. [31] performed *z*-contrast imaging and electron energy loss spectroscopy on Cr-doped DLC and reported uniform Cr distribution in C matrix at lower levels (6 %) and Cr-rich cluster formation at high doping levels (12 %).

4.2 The Role of Chromium and Chromium Carbide

At higher chromium concentrations the EXAFS and XANES provide strong indications that there are chromium carbide precipitates as discussed in Section 3.2.1. The decrease in Cr . Cr coordination number and reduced amplitude of Fourier transform (FT) features with decrease in Cr content for films with $\geq 1.5\%$ Cr can be correlated to the reduction in size of metal nucleated chromium carbide nanoclusters leading to higher percentage of Cr atoms on the surface that has fewer nearest neighbors. The increase in C

nearest neighbors for the film with approximately 0.4 % Cr indicates that the environment around Cr atoms has changed significantly. It suggests that Cr may be present in very small groups of atoms dissolved in the amorphous hydrogenated carbon matrix. This is schematically illustrated in [Figure 4.2.1](#).

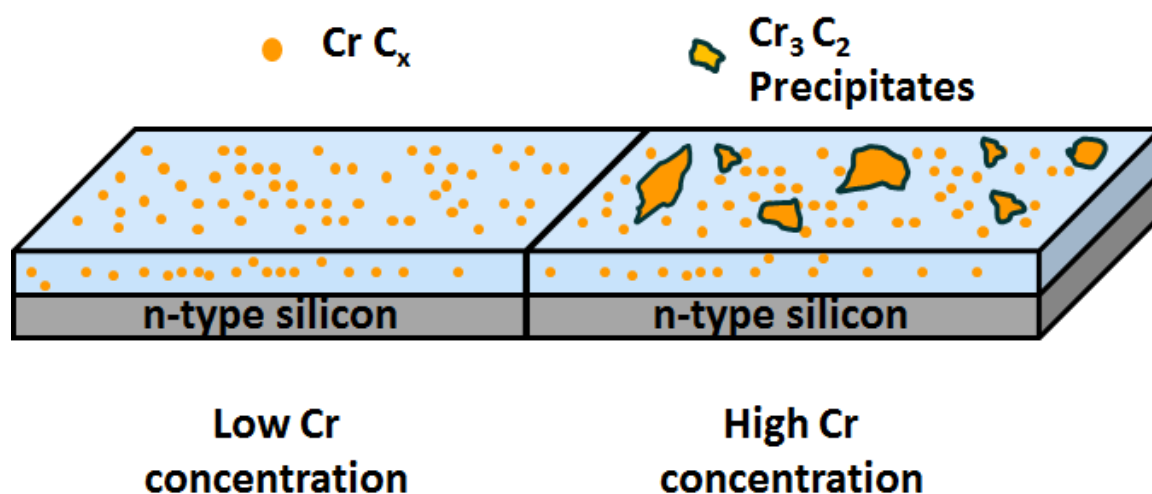


Figure 4.2.1 Cr_3C_2 precipitates only at high doping levels, with the precipitates at higher concentration at the interfaces

At the surface, the situation is somewhat different. Chromium carbide precipitates occur at the higher chromium concentrations and segregate to the surface (and possibly the buried interface) in far greater concentrations than the bulk solution would suggest. From the photoemission, we can clearly see a strong Cr 3d band intensity at the Fermi level, as shown in [Figure 4.2.2](#). The sharp density of states at the Fermi level at the higher photon energies in photoemission looks like a more metallic chromium precipitate at the surface when compared to the undoped diamond-like films.

In fact, while chromium-rich precipitates likely segregate to the surface, these are very likely chromium carbides. We observe that the largely carbon weighted photoemission features at 6 eV are enhanced at photon energies of about 39 to 44 eV as shown in [Figure 4.2.3](#). This is at the Cr 3p band (binding energy of 42 eV) and indicates that the chromium 3d bands are strongly hybridized to carbon 2p. The density of states around 2–3 eV away from the Fermi level increases in intensity at photon energies of about 48 eV to 50 eV and again at about 60 eV, indicating a filling of the Cr 3d bands through the carbide formation, thus chromium photoemission features are enhanced by the weaker Cr 3p to 4s as well as the Cr 3s to 4p resonances. These resonances can occur, but, from studies of nickel [32], are known to be much weaker.

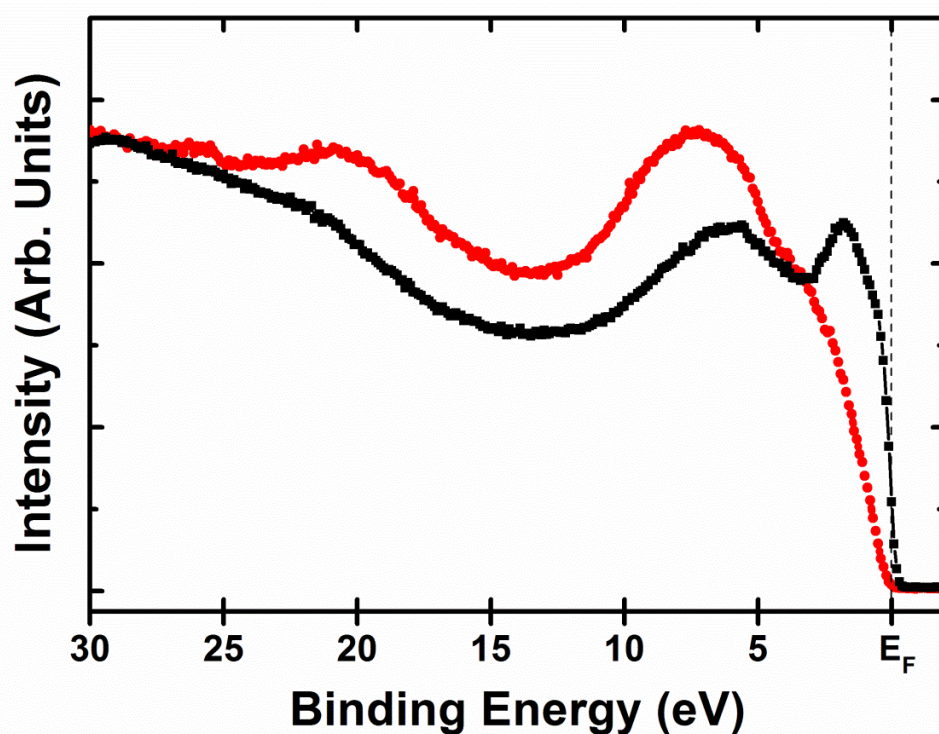


Figure 4.2.2 Photoemission from a 25% chromium doped DLC film (*black*) deposited on silicon, compared to undoped DLC film (*red*). The photon energy was 70 eV and the photoelectrons were collected along the surface normal.

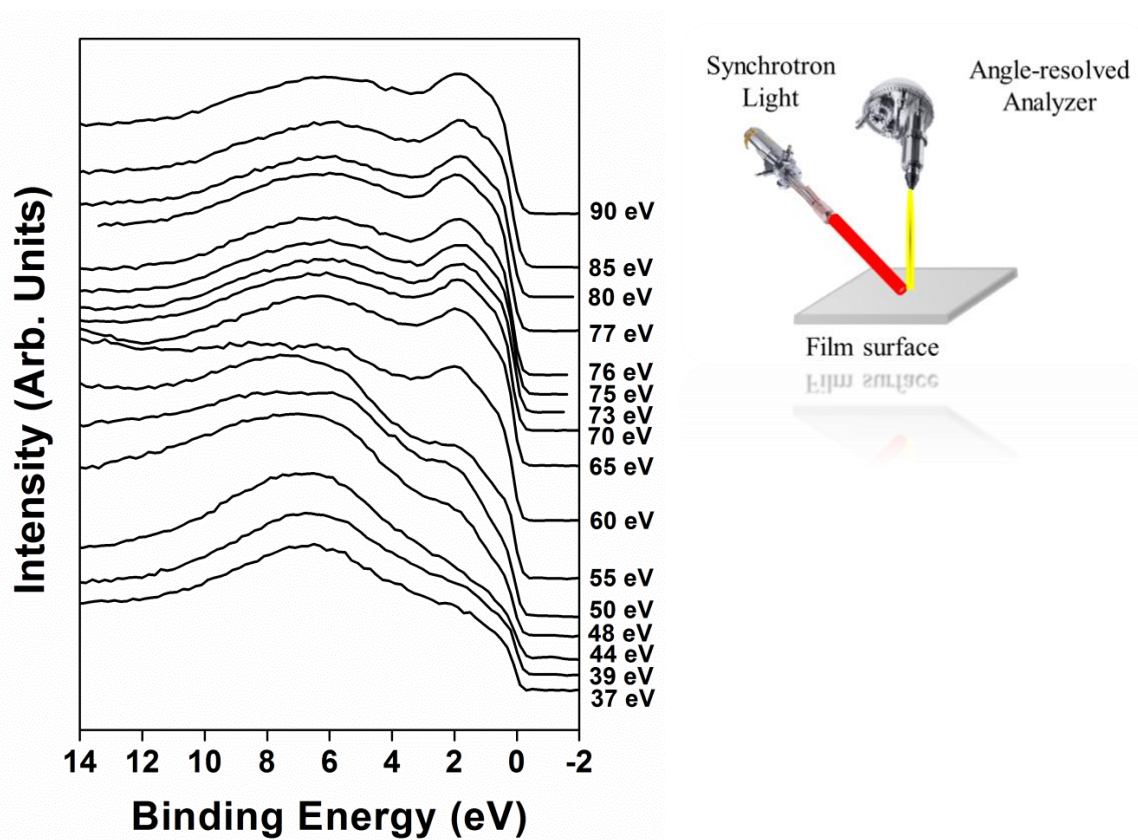


Figure 4.2.3 The photoemission spectra of the 11.0 % Cr-doped DLC film on silicon as a function of photon energy (scale on the right). The photoelectrons were collected along the surface normal.

In fact, these results are very consistent with the work that shows major changes in the surface energies of metal containing amorphous carbon films [33], which may be a result of surface segregation in the case of the nickel containing films, and oxide formation in the case of films doped with Fe or Al.

The strong hybridization between Cr 3d and C 2p bands is likely reason for the low-temperature ferromagnetism of the dilute Cr-DLC. Below 12 Kelvin, the system exhibits ordinary hysteresis loops, with a coercivity of order 0.8 mT (8 Oe), but at somewhat elevated temperatures (above 20 Kelvins), the hysteresis loops are constricted

(wasplike). Figure 4.2.4 shows the magnetization curves of Cr-DLC films with about 3% chromium concentration.

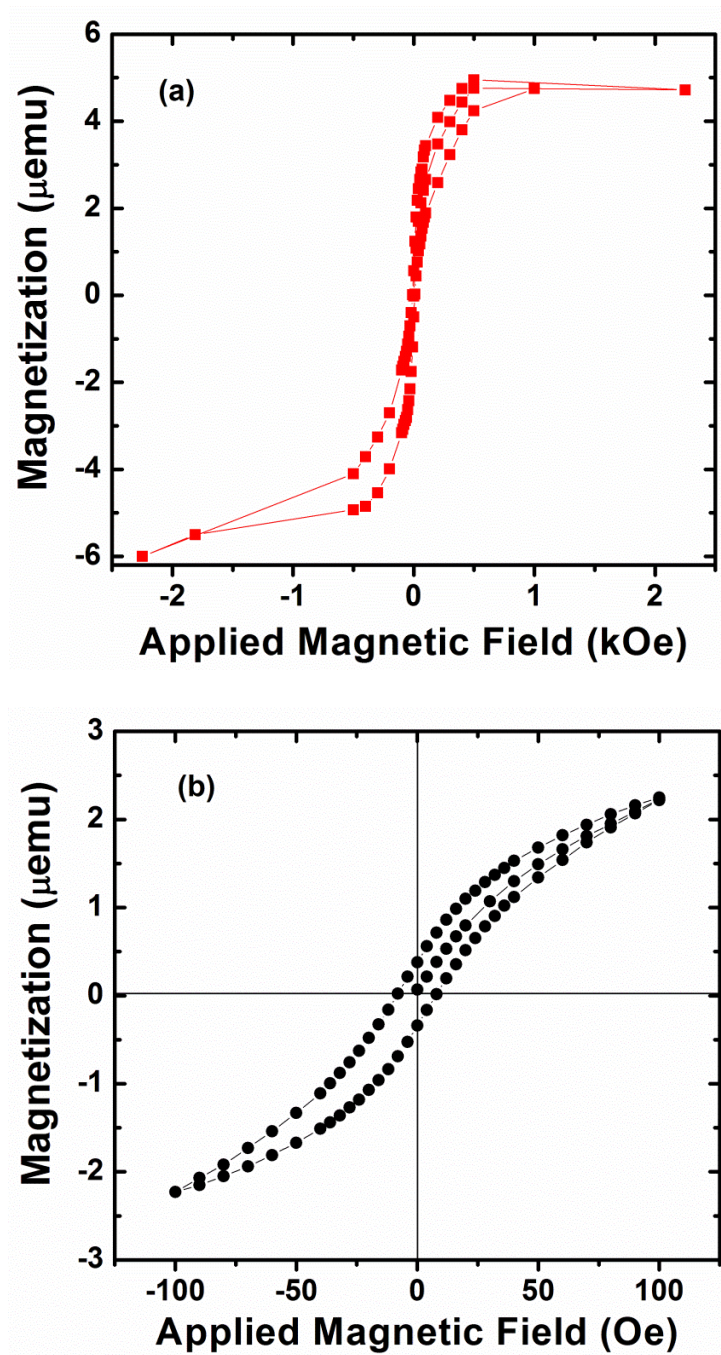


Figure 4.2.4 Hysteresis loops and virgin magnetization curves of Cr-DLC with 3 % Cr at (a) 20 Kelvins and (b) 10 Kelvins.

Constricted loops frequently occur in inhomogeneous ferromagnets [26] and likely reflect a cluster-size distribution ranging from very few interatomic distances to about 10 nm. Exchange interactions leading to Curie temperatures above 20 Kelvins are common in magnetic oxides and not surprising in the present system, where the C $2p$ electrons strongly hybridize with the Cr $3d$ electrons. In fact, the strong overlap between $2p$ electron orbitals in elements such as B, C, and O means that $2p$ moments created by transition-metal ions and other impurities couple relatively rigidly to neighboring $2p$ atoms. Relatively extended orbitals of this type occur in some oxides [16] and Co doped semiconducting boron carbides [7–9].

4.3 Heterojunctions with Silicon Substrates

Generally, we consider chromium a p-type dopant of diamond- like materials, and this is supported by our ability to make good heterojunction diodes with n-type silicon, as seen in Figure 4.3.1. At low doping levels heterojunction diodes can be made, but the capacitance is quite large and dominates the devices properties, consistent with amorphous carbon films on n-type silicon [34-35]. With 5 % Cr doping of the DLC films, the heterojunction with n-type silicon shows clear rectification [Figure 4.3.1(a)], which appears to improve with 11 % and 15 % Cr doping, as seen in Figure 4.3.1(b) and Figure 4.3.1(c), respectively. This improvement in the heterojunction diode rectification, at the higher doping levels, is more evident at lower temperatures for 15 % Cr doped heterojunctions, well below room temperature, as indicated in Figure 4.3.1.

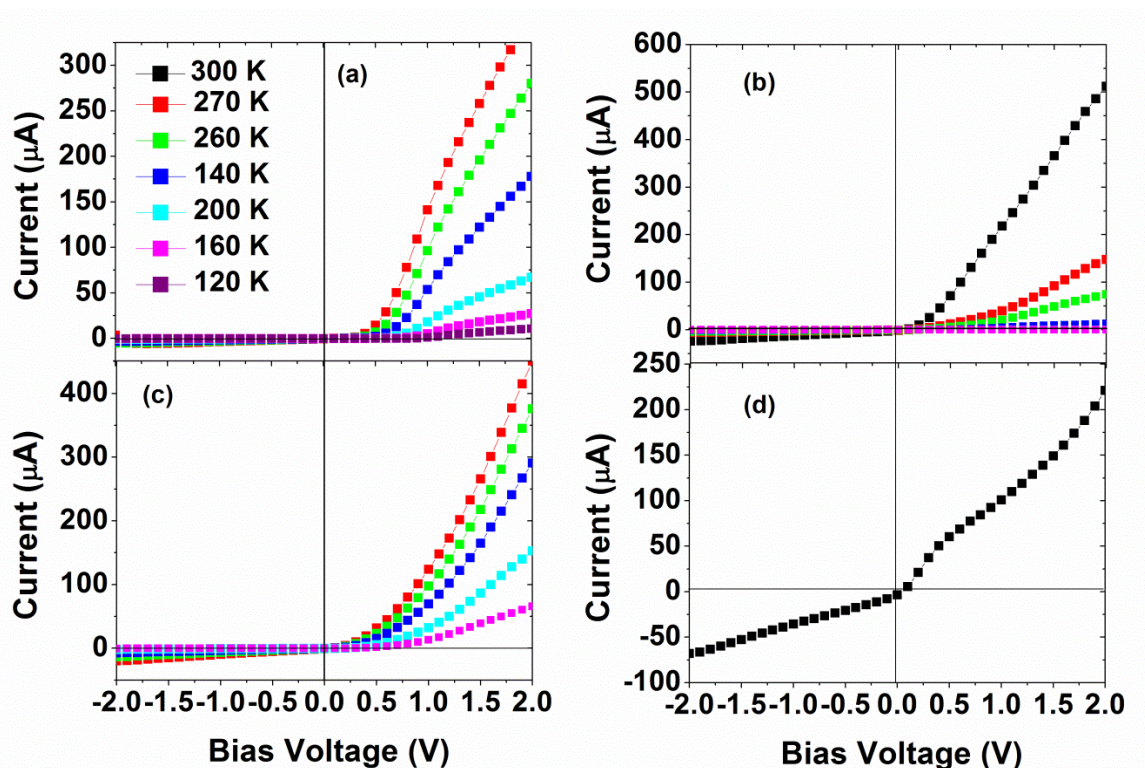


Figure 4.3.1 The I-V curves from Cr-DLC films in a heterojunction with n-type silicon, as a function of temperature, for different chromium doping levels (a) 5.0 %, (b) 11.0 %, (c) 15 % and (d) 20 %.

Increasing the Cr doping concentration with the DLC films to 20 % and beyond does not, however, lead to improved diode characteristics in the heterojunction with silicon. With a Cr doping concentration of 20 at.%, the heterojunction diodes with n-type silicon show very large leakage currents in reverse bias and increasingly resemble a ‘bad’ conventional resistor, as indicated in [Figure 4.3.1](#). What is, perhaps, surprising, is the magnetoresistance of these heterojunction diodes, even at room temperature. In fact, the heterojunction diodes of n-type silicon and 11 % and 15 % Cr-doped DLC films as the p-type semiconductor show a strong negative magnetoresistance, with the forward bias current increasing with increasing magnetic field, as indicated in [Figure 4.3.2](#). At 2.0 V

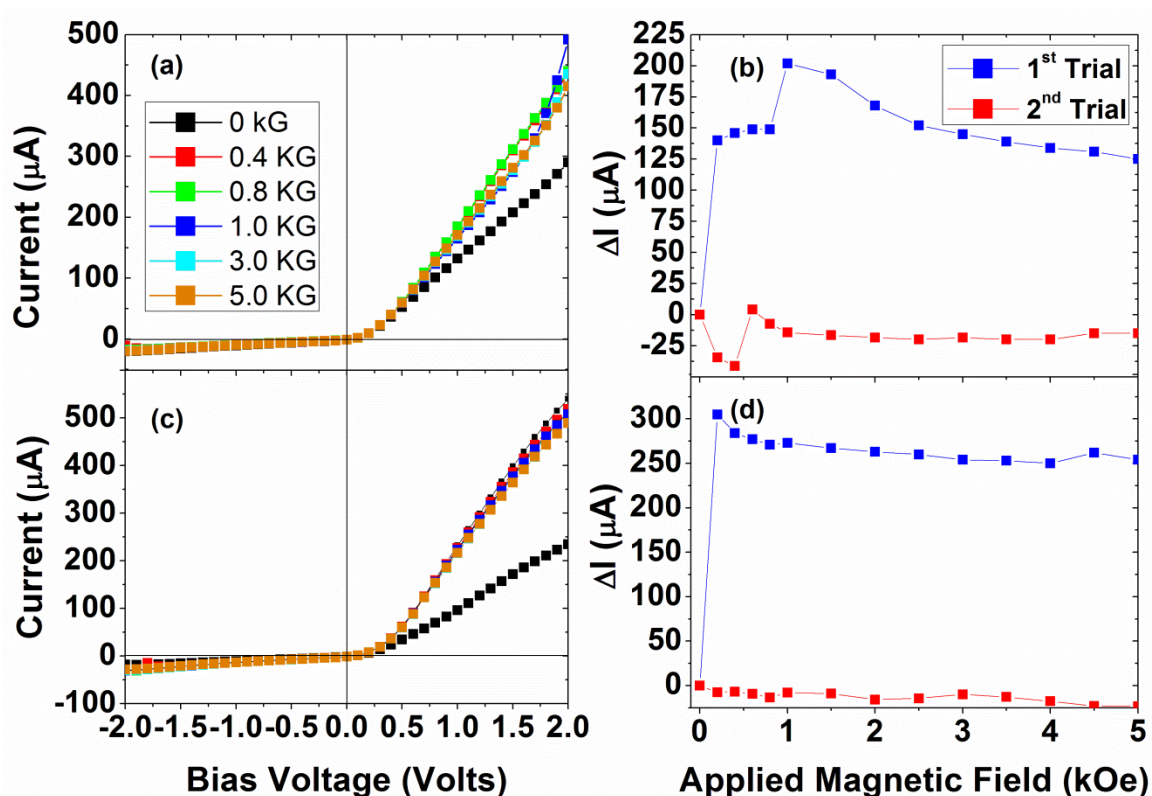


Figure 4.3.2 The I-V curves from the 11 % Cr (a) and 15 % Cr (b) Cr-DLC film to n-type silicon heterojunction devices with changing applied magnetic field. The change in forward current, as a function of the magnetic field, for Cr-DLC film to n-type silicon heterojunction devices at 11.0 % Cr (c), and 15.0 % Cr (d). Forward bias voltage was 2.0 V in panels (c) and (d). All data were acquired at room temperature. In the first trial (*blue*) negative magnetoresistance was observed, but in subsequent trials (*red*) little or no magnetoresistance was found without application of a large field.

forward bias, the negative magnetoresistance is as much as 50 to 100% with as little as 300 Oe applied field. This negative magnetoresistance saturates and shows little change at the higher applied magnetic fields, indicating that some magnetic ordering is the origin of this effect. For the 11% Cr doped DLC/silicon heterojunctions, the negative magnetoresistance is shown in greater detail in Figure 4.3.3. This behavior can be modeled as discussed below. The large increase in the negative magnetoresistance is observed in applied field of 50 to 200 Oe, which values are about the same as the

coercive field in the lightly Cr-doped DLC films. Thus the change in the forward bias current of these diodes may be related to a soft magnet or moment paramagnetic phase dominated by widely dispersed Cr atoms that dominate the DLC films at low Cr doping concentrations. Alignment of a soft magnet phase or the moments of a paramagnetic phase with the hard magnetic could lead to a decrease in resistance. Assuming a dielectric constant of 5.6, and still preserve wave function overlap, the distance between Cr atoms would be 6 Å. This is consistent with the doping levels for which large negative magnetoresistance is observed, but does little to explain the phenomena. In order to explain the decrease in resistance, we model our junction with an equivalent scheme as shown in [Figure 4.3.4](#).

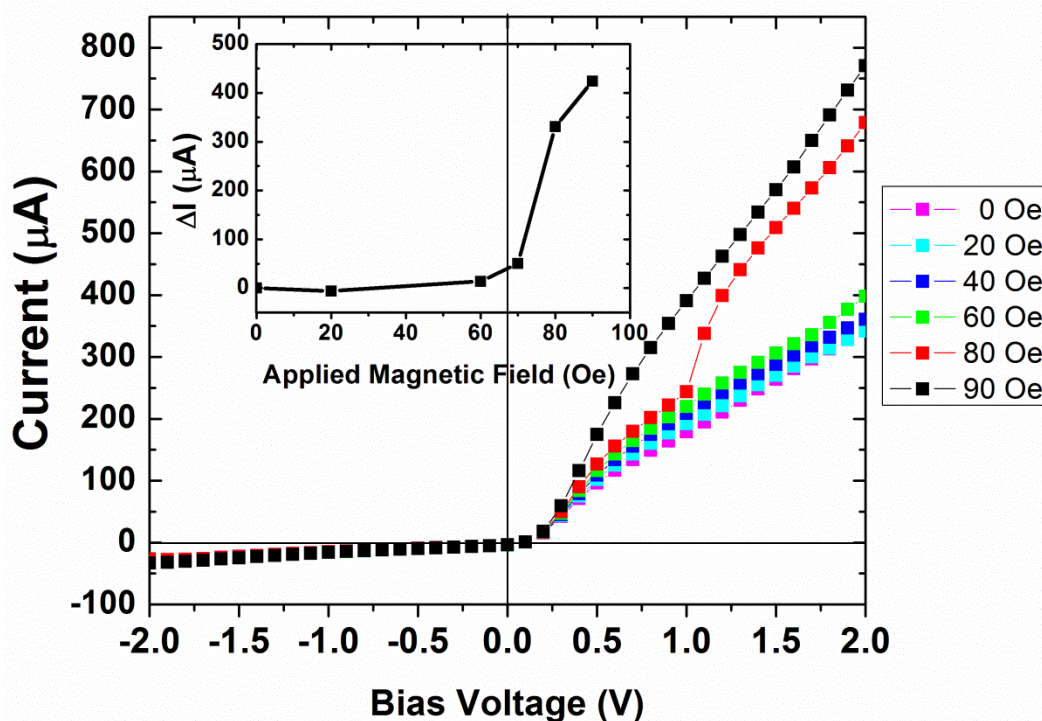


Figure 4.3.3 The I-V curves from a 11 % Cr Cr-DLC film to n-type silicon heterojunction device after magnetization of the sample in a field of 1.0 T. The increase of the negative magnetoresistance is quite evident, and plotted in the *inset* for 2 V forward bias.

This simple model can be described with a modified Shockley equation for a p-n junction:

$$I = I_0 \left(e^{\frac{q(V-IR(H,V))}{k_B T}} - 1 \right) \quad (4.3.1)$$

where I_0 is the saturation current and $R(H, V)$ is the resistance of the semiconductor region doped with the magnetic ions. If the external magnetic field suppresses the spin

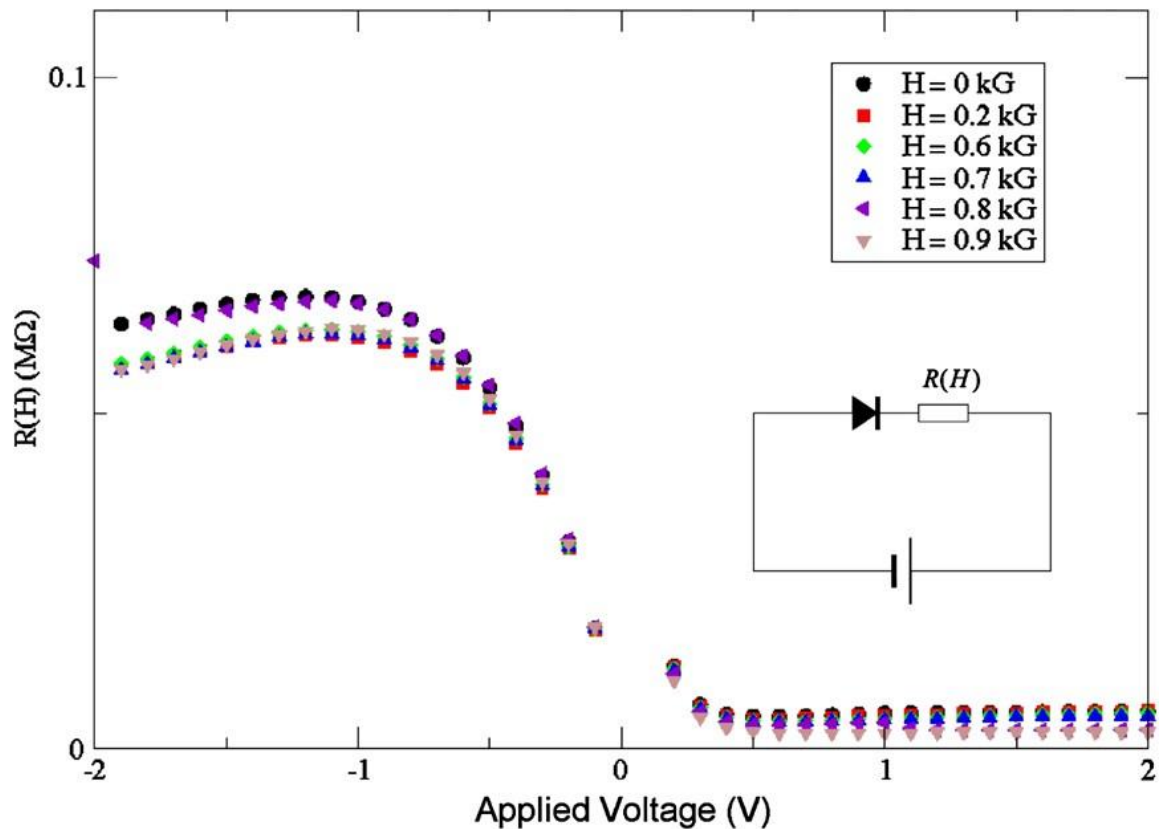


Figure 4.3.4 The resistance of the 11% Cr-doped DLC/silicon heterojunction diode is dependent on voltage in the reverse bias, as indicated in model calculations. The forward bias does not have the same dependence, because the function $R(H)$ is constant with $V > 0$. The schematic is the ideal of the effective circuit for the model calculations.

fluctuation of the magnetic ions, it should lead to a decrease in the resistance. Using the saturation current I_0 , we can determine the resistance from the data:

$$R(H, V) = \frac{1}{I} \left[V - \frac{k_B T}{q} \log \left(\frac{I}{I_0} + 1 \right) \right] \quad (4.3.2)$$

Because resistance can depend on both the voltage and the applied magnetic field, we have plotted $R(H, V)$ versus V in [Figure 4.3.4](#), using the data taken for 11% Cr doped DLC/silicon heterojunctions. If the resistance is not dependent on voltage, our function, $R(H, V) = R(H)$, should be constant for each value of the applied magnetic field H . We found that this is only true for the forward bias; for the reverse bias the resistance does depend on voltage (see [Figure 4.3.4](#)). Now that we have determined the behavior of resistance for changing voltage, we want to fix the voltage and determine if the resistance decreases as the applied magnetic field H increases. We have plotted the resistance $R(H)$ versus H for the forward bias at $V = 1.0 \text{ V}$ in [Figure 4.3.5](#), using the data for the 11% Cr doped DLC/silicon heterojunctions. The resistance does indeed decrease with increasing magnetic field. Hence, we can conclude that the external magnetic field suppresses the spin fluctuations of the magnetic ions in the Cr-doped layer of the diode. Subsequent experiments repeated in large applied magnetic field show a more conventional small positive magnetoresistance, or little effect overall (little change in the forward current magnetoresistance), as indicated in [Figure 4.3.2](#).

It seems clear that there is a hard magnetic phase that becomes increasingly frustrated and “pinned” in different magnetic orientations as the magnetic field is reversed, so that saturating the domains might require a very high magnetic field, possibly as high as many Tesla. The need for a very high magnetic field to realign the harder magnetic phases and domains in the 11 % and 15 % Cr-doped DLC films is supported by experiments taken after applying to the sample a large magnetic field of more than 1.0 Tesla. In such cases, as seen in [Figure 4.3.3](#), a large negative magnetoresistance is observed again with small applied magnetic fields.

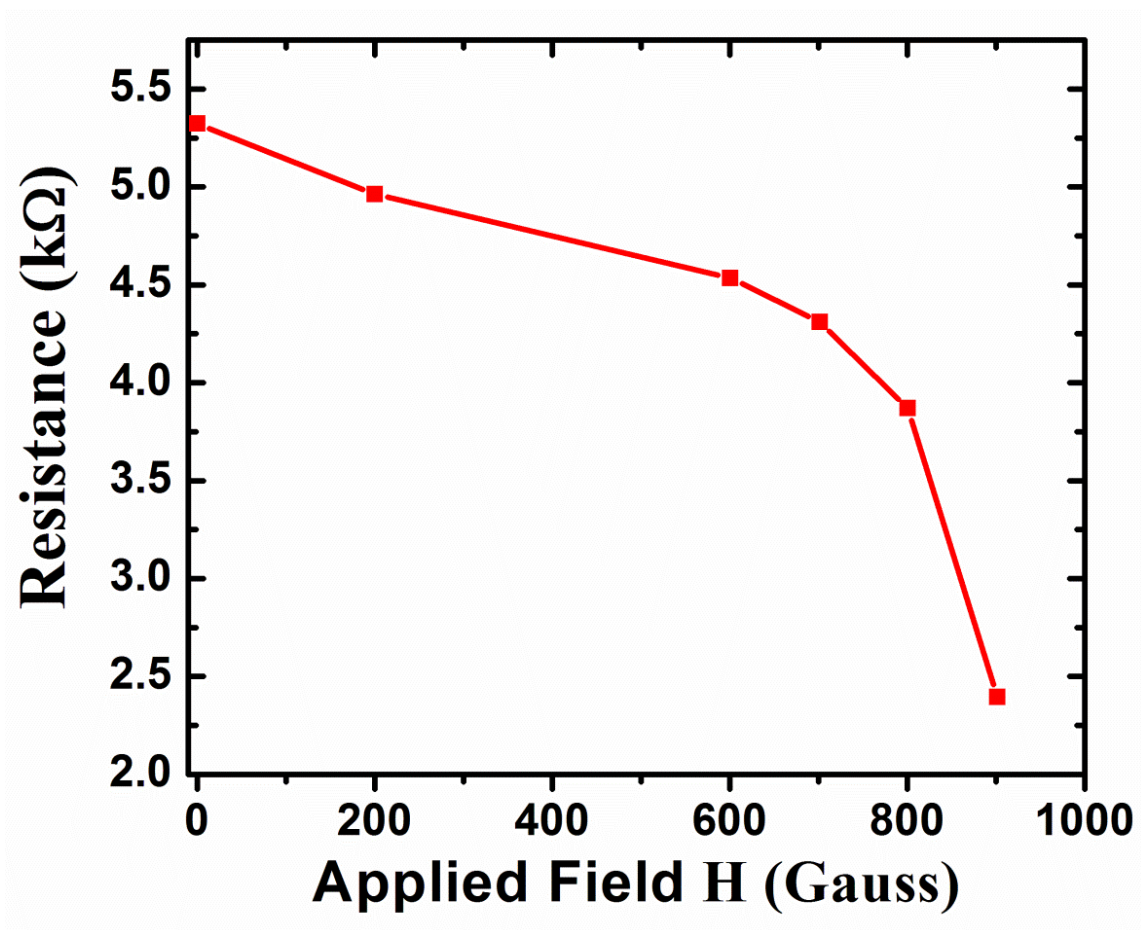


Figure 4.3.5 In the forward bias, in a simple model calculations, the resistance of the 11% Cr-doped DLC/silicon heterojunction diode decreases as the applied magnetic field increases.

The large decrease in magnetoresistance is not observed until about 70 to 90 Oe applied field (Figure 4.3.3), suggesting that this is, in fact, a moment super paramagnetic phase or a soft magnetic phase, not a simple paramagnetic phase, whose moment alignment leads to the observed negative magnetoresistance at low fields. This ‘rewriting’ the low-field magnetoresistance behavior is very reproducible. Overall, the magnetic training in the behavior of these heterojunction diodes leading to a decrease in the rectification properties of the diodes, and possibilities of ‘resetting’ the magnetoresistance behavior leading to a large negative magnetoresistance suggests a spintronic application for these devices that needs to be further explored. This does not seem to be classic memristor behavior as this is field controlled, and we see little voltage controlled.

References

- [1] J.M.D. Coey, M. Venkatesan, C.B. Fitzgerald, “Donor impurity band exchange in dilute ferromagnetic oxides”, *Nat. Mater.* 4, 173 (2005)
- [2] T. Dietl, “Origin and control of ferromagnetism in dilute magnetic semiconductors and oxides”, *J. Appl. Phys.* 103, 07D111 (2008)
- [3] T. Dietl, “Origin of ferromagnetic response in diluted magnetic semiconductors and oxides”, *J. Phys., Condens. Matter* 19, 165204 (2007)
- [4] J.M.D. Coey, “Dilute magnetic oxides”, *Curr. Opin. Solid State Mater. Sci.* 10, 83 (2006)
- [5] H.O. Pierson, *Handbook of Carbon Graphite, Diamond and Fullerenes* (Noyes, Park Ridge, 1993)
- [6] J.E. Field, *Properties of Diamond* (Academic Press, London, 1979)
- [7] L. Carlson, D. LaGraffe, S. Balaz, A. Ignatov, Ya.B. Losovyj, J. Choi, P.A. Dowben, J.I. Brand, “Doping of boron carbides with cobalt, using cobaltocene”, *Appl. Phys. A* 89, 195 (2007)
- [8] A.Yu. Ignatov, Ya.B. Losovyj, L. Carlson, D. LaGraffe, J.I. Brand, P.A. Dowben, “Pairwise cobalt doping of boron carbides with cobaltocene”, *J. Appl. Phys.* 102, 083520 (2007)
- [9] P.A. Dowben, A.Yu. Ignatov, J. Liu, R. Skomski, “The local environment of Co in B_5CH_x ”, *J. Appl. Phys.* 103, 07D125 (2008)
- [10] O.K. Andersen, T. Saha-Dasgupta, “Muffin-tin orbitals of arbitrary order”, *Phys. Rev. B* 62, R16219 (2000)
- [11] J. Blinowski, P. Kacman, J.A. Majewski, “Ferromagnetic superexchange in Cr-based diluted magnetic semiconductors”, *Phys. Rev. B* 53, 9524 (1996)
- [12] B.K. Roberts, A.B. Pakhomov, P. Voll, K.M. Krishnan, “Surface scaling of magnetism in Cr:ZnO dilute magnetic dielectric thin films”, *Appl. Phys. Lett.* 92, 162511 (2008)
- [13] B.K. Roberts, A.B. Pakhomov, V.S. Shutthanandan, K.M. Krishnan, “Ferromagnetic Cr-doped ZnO for spin electronics via magnetron sputtering”, *J. Appl. Phys.* 97, 10D310 (2005)

- [14] S. Kuroda, N. Ozaki, N. Nishizawa, T. Kumekawa, S. Marcet, K. Takita, "Growth and magnetic properties of novel ferromagnetic semiconductor (Zn, Cr)Te", *Sci. Technol. Adv. Mater.* 6, 558 (2005)
- [15] N. Ozaki, I. Okabayashi, T. Kumekawa, N. Nishizawa, S. Marcet, S. Kuroda, K. Takita, "Growth and magnetic properties of novel ferromagnetic semiconductor (Zn, Cr)Te", *Appl. Phys. Lett.* 87, 192116 (2005)
- [16] P.A. Anderson, R.J. Kinsey, S.M. Durbin, A. Markwitz, V.J. Kennedy, A. Asadov, W. Gao, R.J. Reeves, "Magnetic and optical properties of the InCrN system", *J. Appl. Phys.* 98, 043903 (2005)
- [17] J.Q. Wang, P.P. Chen, X.G. Guo, Z. Li, W. Lu, "Magnetic and optical properties of Cr⁺-implanted GaN", *J. Cryst. Growth* 275, 393 (2005)
- [18] A.Y. Polyakov, N.B. Smirnov, A.V. Govorkov R.M. Frazier, J.Y. Liefer, G.T. Thaler, C.R. Abernathy, S.J. Pearton, J.M. Zavada, "Properties of highly Cr-doped AlN", *Appl. Phys. Lett.* 85, 4067 (2004)
- [19] A.Y. Polyakov, A.V. Govorkov, N.B. Smirnov, N.V. Pashkova, S.J. Pearton, K. Ip, R.M. Frazier, C.R. Abernathy, D.P. Norton, J.M. Zavada, R.G. Wilson, *Mater. Sci. Semicond. Process.* 7, 77 (2004)
- [20] G.B. Cha, S.G. Cho, S.C. Hong, "First principles calculations on electronic structure and magnetism of (CrAs)₁(GaAs)_x (x = 1, 3, and 5) superlattices", *Phys. Stat. Sol. (b)* 241, 1423 (2004)
- [21] A.Y. Polyakov, N.B. Smirnov, A.V. Govorkov, G.T. Thaler, C.R. Abernathy, S.J. Pearton, J.M. Zavada, R.G. Wilson, "Optical and Electrical Properties of AlGa_N Films Implanted with Mn, Co, or Cr", *J. Electron. Mater.* 33, 384 (2004)
- [22] J.S. Lee, J.D. Lim, Z.G. Khim, Y.D. Park, S.J. Pearton, S.N.G. Chu, "Magnetic and structural properties of Co, Cr, V ion-implanted GaN", *J. Appl. Phys.* 93, 4512 (2003)
- [23] S.A. Chambers, T.C. Droubay, C.M. Wang, K.M. Rosso, S.M. Heald, D.A. Schwartz, K.R. Kittilstved, D.R. Gamelin, "Ferromagnetism in oxide semiconductors", *Mater. Today* 9, 28 (2006)
- [24] S.A. Chambers, "Ferromagnetism in doped thin-film oxide and nitride semiconductors and dielectrics", *Surf. Sci. Rep.* 61, 345 (2006)
- [25] T.C. Kaspar, T. Droubay, D.E. McCready, P. Nachimuthu, S.M. Heald, C.M. Wang, A.S. Lea, V. Shutthanandan, S.A. Chambers, M.F. Toney, "Magnetic properties of epitaxial Co-doped anatase TiO₂ thin films with excellent structural quality", *J. Vac. Sci. Technol. B* 24, 2012 (2006)

- [26] S.A. Chambers, T. Droubay, C.M.Wang, A.S. Lea, R.F.C. Farrow, L. Folks, V. Deline, S. Anders, "Clusters and magnetism in epitaxial Co-doped TiO₂ anatase", *Appl. Phys. Lett.* 82, 1257 (2003)
- [27] H.Q. Song, L.M. Mei, S.S. Yan, X.L. Ma, J.P. Liu, Y. Wang, Z. Zhang, "Microstructure, ferromagnetism, and magnetic transport of Ti_{1-x}Co_xO₂ amorphous magnetic semiconductor", *J. Appl. Phys.* 99, 123903 (2006)
- [28] G.S. Chang, E.Z. Kurmaev, D.W. Boukhvalov, D.L. Finkelstein, D.H. Kim, T.W. Noh, A. Moewes, T.A. Callcott, "Clustering of impurity atoms in Co-doped anatase TiO₂ thin films probed with soft x-ray fluorescence", *J. Phys., Condens. Matter* 18, 4243 (2006)
- [29] B.S. Jeong, Y.W. Heo, D.P. Norton, A.F. Hebard, "Structure and composition of secondary phase particles in cobalt-doped TiO₂ films", *Physica B* 370, 46 (2005)
- [30] V. Singh, V. Palshin, R.C. Tittsworth, E.I. Meletis, *Carbon* 44, 1280 (2006)
- [31] X. Fan, E.C. Dickey, S.J. Pennycook, M.K. Sunkara, "Z-contrast imaging and electron energy-loss spectroscopy analysis of chromium-doped diamond-like carbon films", *Appl. Phys. Lett.* 75, 2740 (1999)
- [32] Y. Sakisaka, T.N. Rhodin, P.A. Dowben, *Solid State Commun.* 49, 563 (1984)
- [33] J.S. Chen, S.P. Lau, Z. Sun, G.Y. Chen, Y.J. Li, B.K. Tay, J.W. Chai, "Metal-containing amorphous carbon films for hydrophobic application", *Thin Solid Films* 398–399, 110 (2001)
- [34] L. Valentini, V. Salerni, I. Armentano, J.M. Kenny, L. Lozzi, S. Santucci, "Effects of fluorine incorporation on the properties of amorphous carbon/p-type crystalline silicon heterojunction diodes", *J. Non-Cryst. Solids* 321, 175 (2003)
- [35] N. Konofaos, E.V. Evangelou, N.A. Hastas, Y. Panayiotatos, C.A. Dimitriadis, S. Logothetidis, "The effects of interface and bulk defects on the electrical performance of amorphous carbon/silicon heterojunctions", *Mat. Sci. Eng. B* 91–92, 379 (2002)

Chapter 5

Electronic Band Structure and Transport Characterization for Magnetic Dilute Semiconductors using High k Dielectric Materials

“I have not failed. I've just found 10,000 ways that won't work”

-Thomas A. Edison-

We have shown in chapter 3 that these rare earth based compounds can be grown with strong texture when using silicon as our substrate. This leads us to the next step of this saga which consists on exploring the effect by the introduction of rare earth dopants (specifically Gd and Ce) on the electronic band structure of these. A remarkable effect is seen on the EuO films as the inclusion of 4% Gd drive the system across the non-metal to metal transition. All rare earth doped and rare earth containing compounds were tested as to their ability to form heterostructure diodes. Although a rigorous characterization of the devices was not performed, our results provide complementary information regarding the device functionalities highlighting the attempts to reproduce the behavior observed in Cr-DLC (i.e. an I-V curve dependent on the external magnetic field).

5.1 A Comparison of Gd_2O_3 and Gd:HfO_2

5.1.1 The Experimental and Theoretical Band Structure

Photoemission measurements were performed as explained in [Section 2.1](#). The valence band edge is placed well away from the Fermi level for both 3% Gd doped and undoped HfO_2 films. As reported previously [[1](#), [2](#)], the Hf 4f binding energies and valence band edge are similar [[3](#)] or slightly larger than those reported elsewhere [[4](#), [5](#), [6](#)]. The shoulder on the broad photoemission peak at the binding energy of 9-10 eV, can be assigned strong Gd 4f weight [[4](#), [5](#)]. A small enhancement is evident in the photoemission density of state in the region of 4.0 eV with the increase of Gd concentration, as seen in the inset on [Figure 5.1.1](#). The opposite of this behavior (DOS decrease) have been reported when doping with yttrium. The increase in binding energy of all the major photoemission features seen with Gd doping is not observed for $(\text{HfO}_2)_{1-x}(\text{Y}_2\text{O}_3)_x$ samples [[6](#)]. It seem Yttrium segregates away from the zirconia surface [[7](#)], and might show similar behavior with HfO_2 . As of gadolinium, is expected to segregate towards the surface because of its larger size, but for this samples no significant gadolinium surface segregation was observed. Even though these materials have similar surface terminations [[8](#)], the Fermi level pinning may be very different for the two dopants.

The valence band density of states, as determined by photoemission for Gd_2O_3 , are very similar to that observed for 3% Gd doped films, as indicated in [Figure 5.1.2](#). The major difference is that for Gd_2O_3 , we require 4 components at a minimum to fit the valence band spectra, as also indicated in [Figure 5.1.2](#). This might be expected as from

the crystal structure as there are differences in the crystal field around oxygen and gadolinium: there are two very inequivalent oxygen species, and to a lesser extent true as

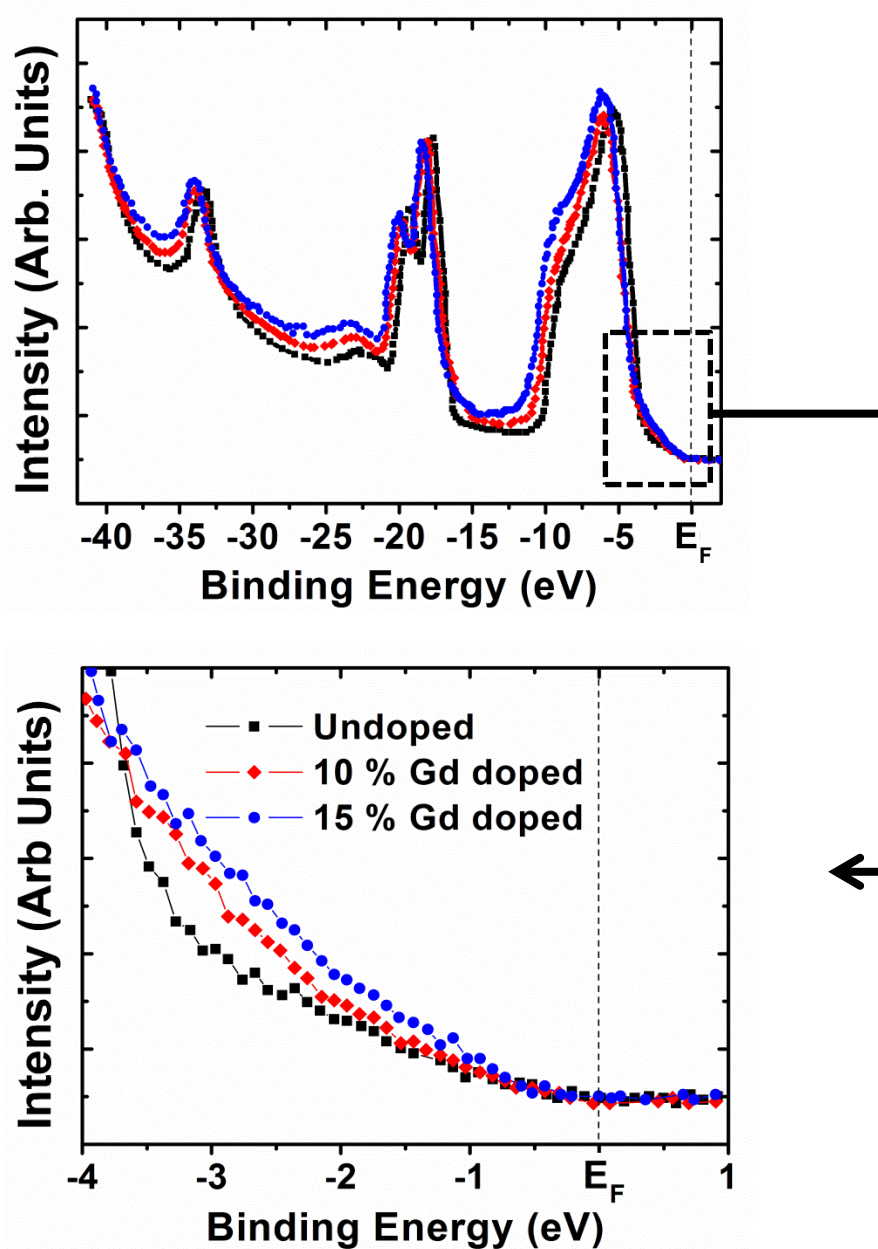


Figure 5.1.1 Different bands intensities for pristine and Gd-doped films of HfO_2 . The photon energy used was 100 eV and the light incidence angle is 45° . All photoelectrons were collected along the surface normal at $T = 320^\circ\text{C}$.

well of gadolinium, as indicated in [Figure 3.2.6](#). In fact the gadolinium atoms occupy

three inequivalent sites as well, but this does not really lead to a further splitting in the valence band electronic structure sufficient to explain, as discussed below, the two widely separated Gd 4f components at a binding energy of about 8.7 to 9.5 eV below the Fermi level and the ‘shoulder’ at a binding energy of 11 to 12 eV.

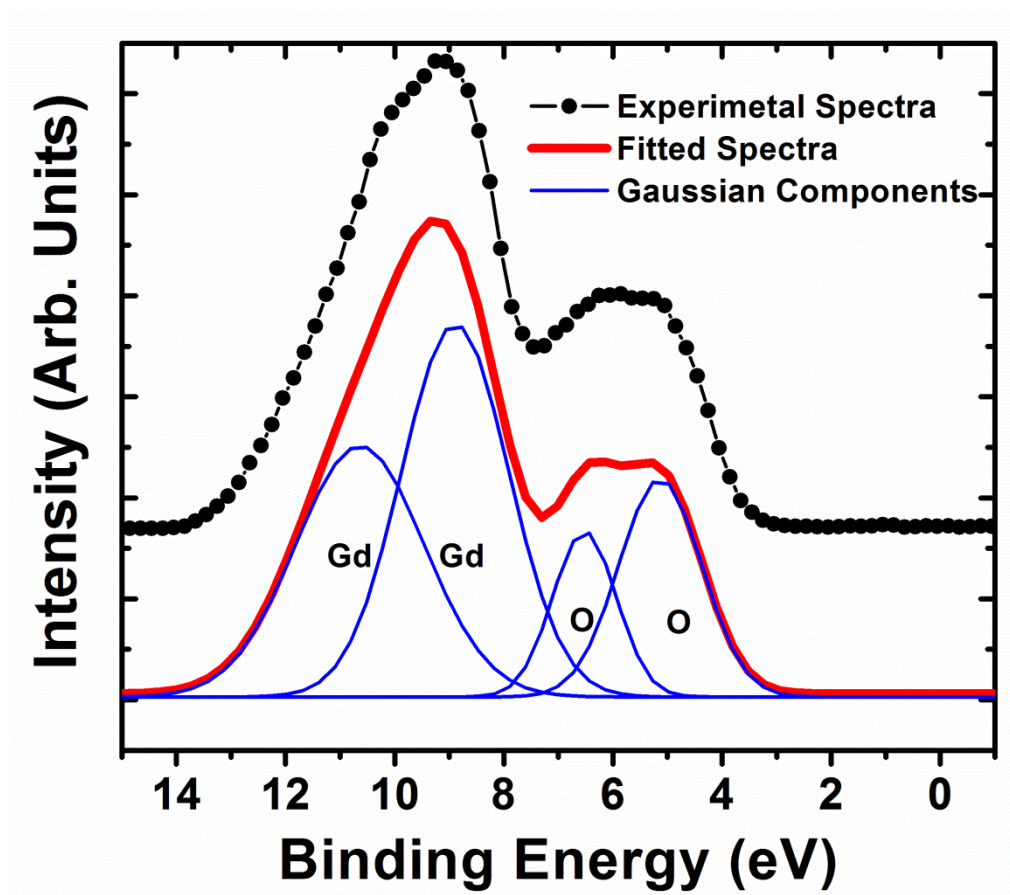


Figure 5.1.2 The photoemission spectrum of the valence band Gd_2O_3 $\langle \bar{4}02 \rangle$. The various components contributing to the valence band structure are indicated and major contributions to the photoemission features indicated. The photon energy is 117 eV and the light incidence angle is 45° . All photoelectrons were collected along the surface normal at $T = 240^\circ\text{C}$.

Confirmation that the Gd 4f states contribute to the shoulder at 9-10 eV on the broad photoemission feature from 5 to 10 eV binding energy was found in resonant photoemission (i.e. constant initial state spectroscopy) measurements of Gd doped HfO_2 .

The results are shown in [Figure 5.1.3](#).

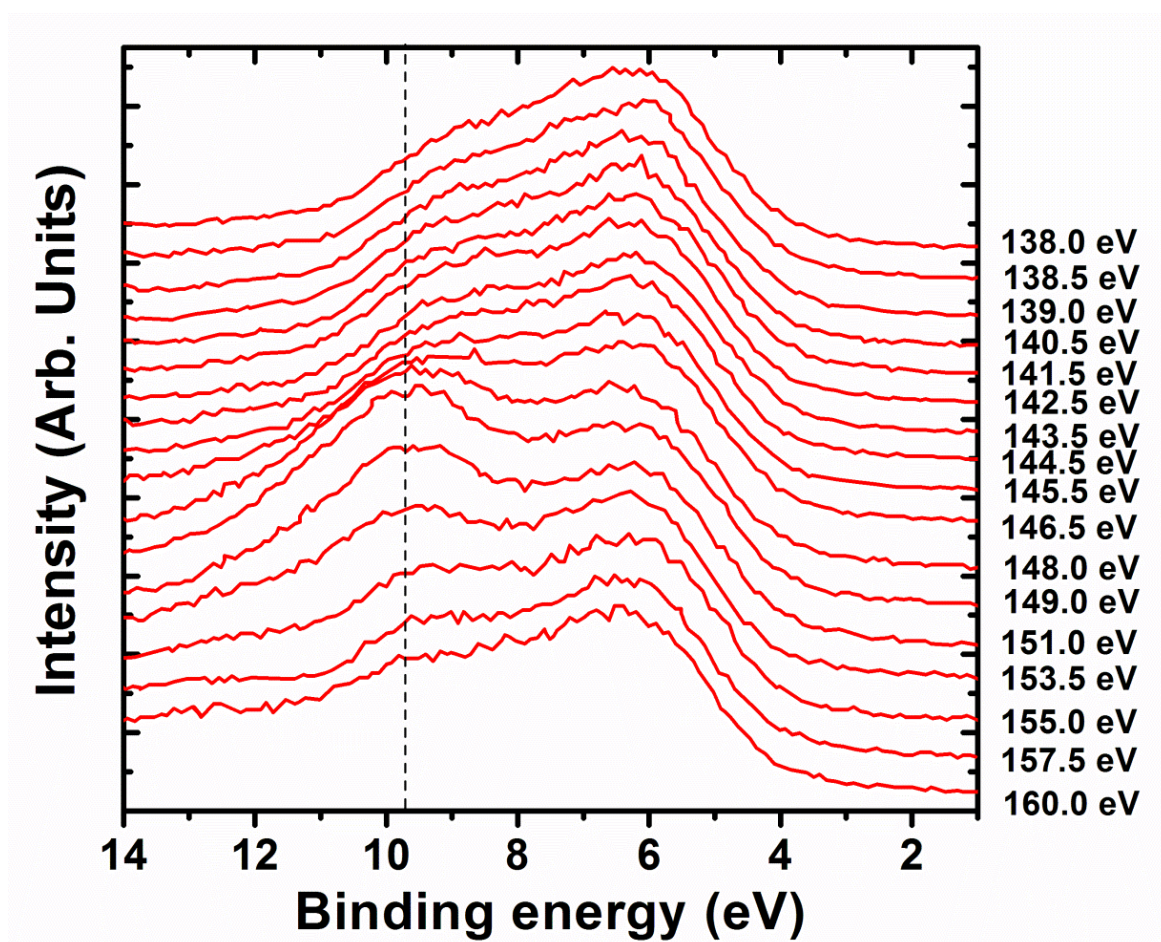


Figure 5.1.3 Resonant photoemission spectra for photon energies through the $4d \rightarrow 4f$ resonance for Gd doped films of HfO_2 . Light incidence angle is 45° . All photoelectrons were collected along the surface normal.

The photoelectron intensities from Gd doped HfO_2 , determined from the feature at about 9.5 eV binding energy (from the Fermi level) are strongly enhanced at about 149 eV photon energy. Similarly for Gd_2O_3 , we see that the components of the valence band at about 8.7 eV to 9.5 eV and the ‘shoulder’ at 11 eV to 12 eV binding energies are enhanced at about 152 eV, as shown in [Figure 5.1.4](#) and plotted in [Figure 5.1.5](#). For comparison, we have plotted this resonant enhancement in the valence band photoemission spectra, for both Gd_2O_3 and Gd doped HfO_2 films for various photon

energies in Figure 5.1.5 (a) and Figure 5.1.5 (b) respectively.

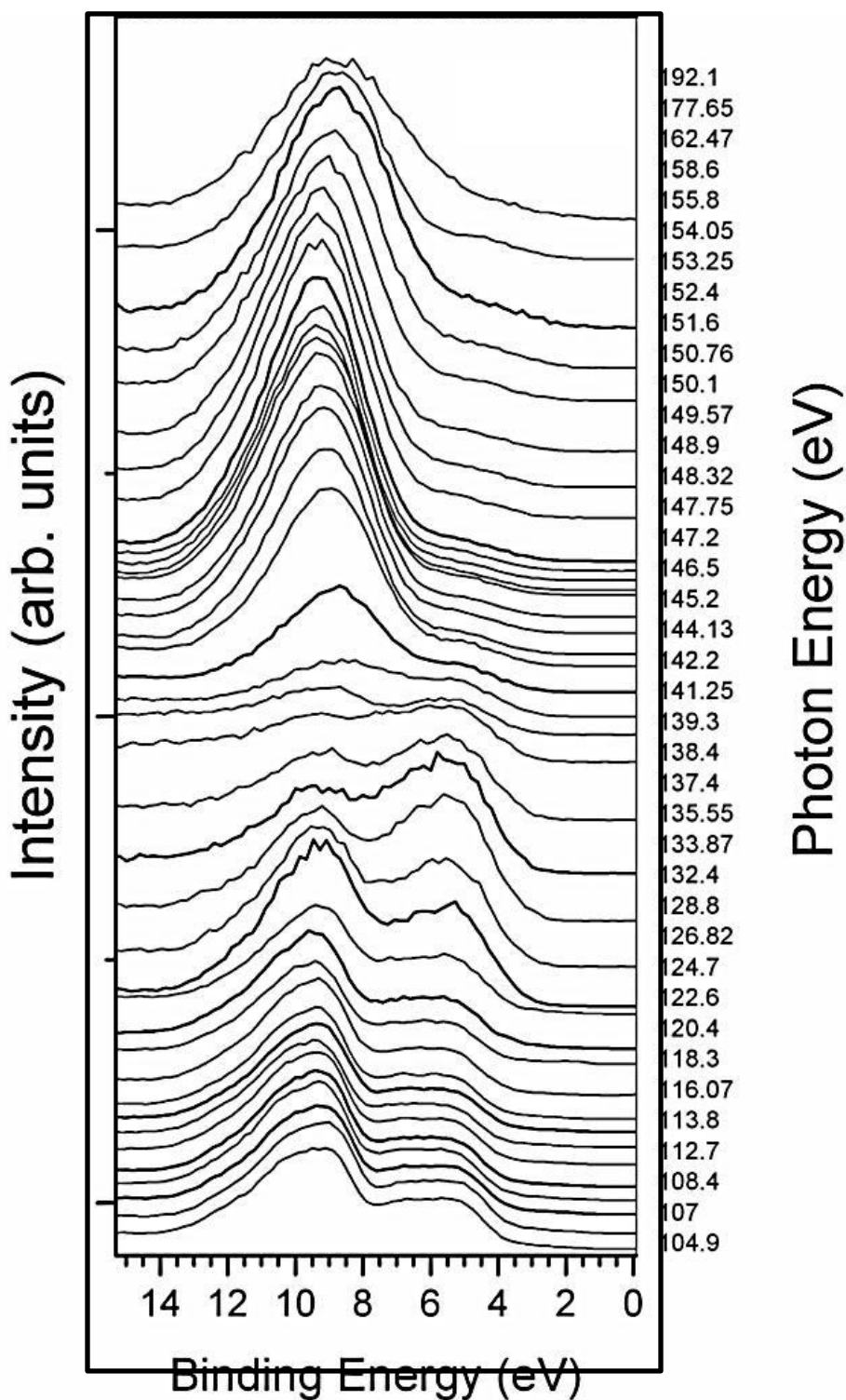


Figure 5.1.4 The resonant photoemission spectra for photon energies through the $4d \rightarrow 4f$ resonance for Gd_2O_3 . Light incidence angle is 45° . All photoelectrons were collected along the surface normal.

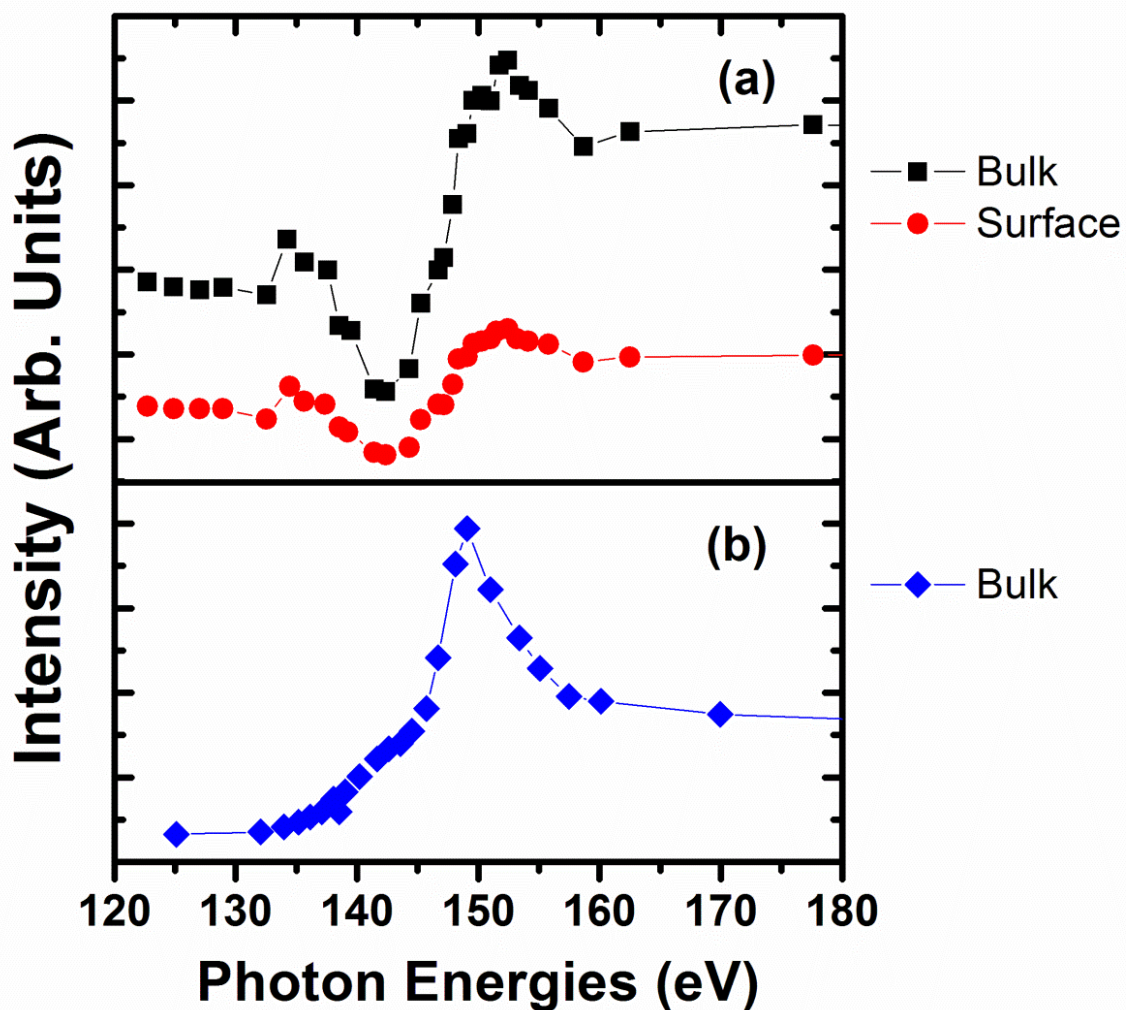


Figure 5.1.5 The resonant photoemission intensities through the $4d \rightarrow 4f$ resonance for Gd_2O_3 (a) and Gd doped films of HfO_2 (b). For Gd_2O_3 , there are seen to be two Gd 4f components at a binding energy of about 8.7–9.5 eV below the Fermi level and the ‘shoulder’ at a binding energy of 11–12 eV, which are assigned as bulk (*black*) and surface (*red*) components respectively.

It is clear that the resonant enhancements in the photoemission intensity, from this 9.5 eV binding energy final state for Gd doped HfO_2 and 8.7 to 9.5 eV for Gd_2O_3 , occur at photon energies corresponding to the core threshold binding energy of the Gd $4d_{3/2}$ (147 eV) shallow core although at somewhat larger photon energy for Gd_2O_3 . This shift of the photoemission resonance to higher photon energies is expected because of the

increase in binding energy of the 4d core and decrease in the conduction band edge binding energy (a placement of the conduction band edge well above the Fermi level [6]). These are in these nominally dielectric oxides, as compared to gadolinium metal. Thus the feature, in the region of 9.5 eV binding energy final state for Gd doped HfO₂ and 8.7 to 9.5 eV for Gd₂O₃, has strong Gd weight. The resonant photoemission process occurs because of an excitation from the 4d cores to a bound state, but with a final state identical to that resulting from direct photoemission from Gd 4f states [9-11]. The photoemission resonance, with changing photon energy, is due to constructive interference between the direct 4f photoionization and a $4d^{10}4f^7 \rightarrow 4d^94f^8 \rightarrow 4d^{10}4f^6 + e^-$ super Coster-Kronig transition, leading to a classic Fano resonance. The classic Fano resonance shape is very clearly seen for the Gd 4f weighted valence band feature intensities, as plotted in [Figure 5.1.5\(a\)](#).

These results are generally in agreement with our expectations from the calculated band structure and density of states. The electronic structure of the B-type Gd₂O₃ (monoclinic) having six formula units per monoclinic cell has been calculated using the projected augmented wave method and the generalized gradient approximation (GGA-PBE) with Hubbard U correction (GGA+U) [12] on the Gd 4f energy levels, as implemented in the VASP package [13]. In the GGA+U calculations, we use $U=7.5$ eV and $J = 0.6$ eV for the Gd 4f orbitals to take the correlation effects into account. The value of the Hubbard U used here is very close to the value used for the Gd 4f energy levels in the molecular endo-fullerene Gd@C₆₀ [14]. A similar (although somewhat smaller) value of $U = 6.7$ eV was found to be appropriate in the examples of the Gd pnictides GdX (X = N, P, As, and Bi) compounds [15].

The calculated value of the band gap for the B-type Gd_2O_3 (monoclinic) from the LDA + U with the GGA method is 3.8 eV. This is much less than observed (5.4 eV) but typifies such estimates obtain by Density Functional Theory (DFT). The monoclinic Gd_2O_3 density of states (DOS), broadened with a Gaussian width 0.2 eV, is shown in [Figure 5.1.6](#). The total density of states has been projected onto each atomic species (gadolinium and oxygen) showing the strong Gd 4f character at the DOS peak around $E = -6.3 \text{ eV}$ and the major oxygen 2p character over the energy range of -5 to 0 eV . This calculation places the occupied Gd 4f levels are a binding energy slightly greater (by about 0.5 to 1 eV), relative to the valence band maximum, than is observed in experiment, even if only the major Gd 4f component is considered.

There are three different Gd sites Gd(1), Gd(2) and Gd(3) in monoclinic Gd_2O_3 , with different coordination numbers and neighboring atoms. To analyze the Gd 4f DOS peak, we calculated the contributions of crystallographically different Gd atoms to the DOS, as indicated by Gd(1), Gd(2), and Gd(3) in the inset of [Figure 5.1.6](#). While there are clearly differences between Gd(1) and Gd(3), there are some similarities. Each Gd atom site has seven oxygen neighbors, however, for Gd(3), the seventh oxygen neighbor is located farther away than for Gd(1) and Gd(2), so only 6 neighbor are included in the primary coordination shell. The coordination about Gd(3) is a distorted octahedron with the seventh oxygen atom along a three-fold axis. For Gd(1) and Gd(2), this is not the case, and both have the same 2mm symmetry and 7 oxygen neighbors within the primary coordination shell ([Figure 3.2.6](#)). The six oxygen about Gd(1), or Gd(2), form a trigonal prism and the seventh lies along a normal to a prism face. In considering the Gd-Gd

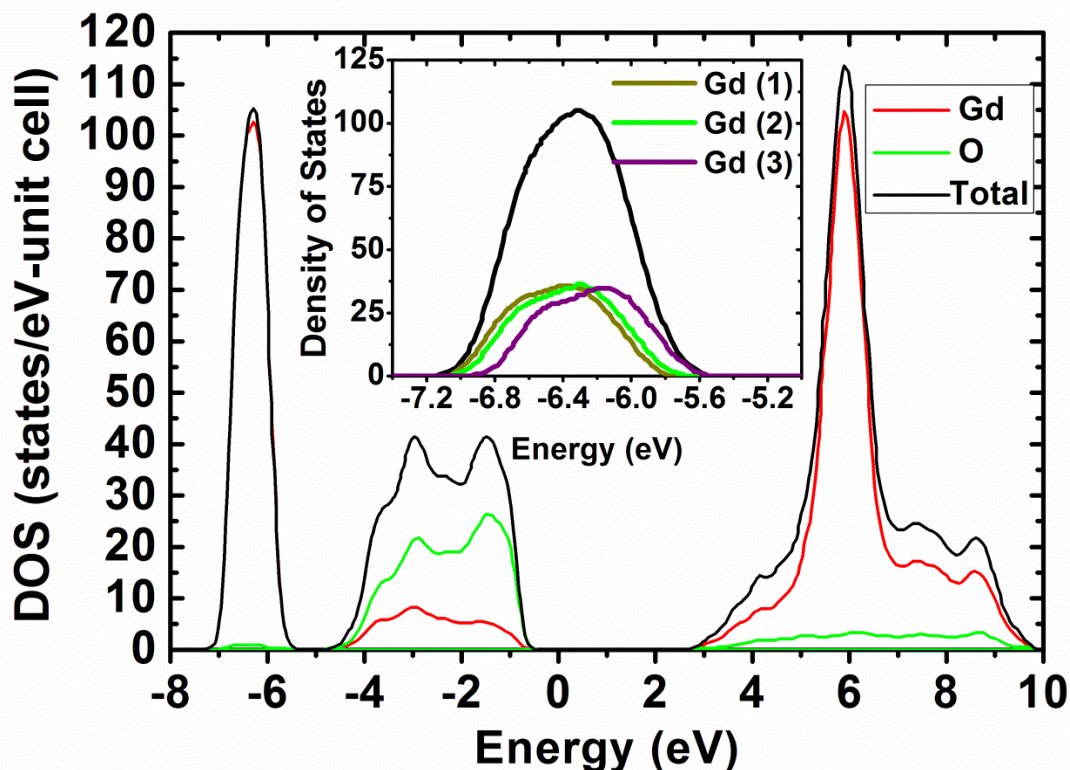


Figure 5.1.6. The calculated density of states for monoclinic (type B) Gd_2O_3 . The monoclinic Gd_2O_3 density of states (DOS) has been broadened with a Gaussian width 0.2 eV. The total density of states has been projected onto each atomic species (gadolinium and oxygen) showing the strong Gd 4f character at the DOS peak around $E = -6.3$ eV and the major oxygen 2p character hybridized with Gd 5d orbitals over the energy range of -5 to 0 eV.

distances, Gd(1) and Gd(2) are again similar, having 10 Gd neighbors at distances ranging from 3.28 to 3.98 Å and two more Gd atoms placed further away. On the other hand, Gd(3) has 12 gadolinium neighbors ranging from 3.58 to 3.87 Å. As a result, the Gd 4f DOS peak originates from the three distinct types of Gd atoms whose corresponding 4f energy levels are split by as much as approximately 0.5 eV due to the spin-orbit coupling but are rigidly shifted due to their crystallographic identities. The full linewidth of the Gd 4f DOS peak is about 1.3 eV.

Since the two components we have identified in photoemission of Gd_2O_3 (-402) as heavily Gd 4f, in weight or oscillator strength (on the basis of their photon energy

dependence at the $4d^{10}4f^7 \rightarrow 4d^94f^8 \rightarrow 4d^{10}4f^6 + e^-$ -super Coster-Kronig transition, shown in [Figure 5.1.5 \(a\)](#), are separated by slightly more than 2 eV, we must conclude that the higher binding energy component is, in fact, a consequence of the surface to bulk shift. The Gd occupied 4f surface to bulk shift is only about 0.4 eV for Gd metal, but is expected to be much larger with oxidation [[16](#)], with the surface component at the greater binding energy. Both exhibit very similar resonance, it is the larger intensity component, at 8.7 to 9.5 eV binding energy, associated with the bulk Gd 4f weighted bands of Gd_2O_3 , that are of interest in establishing the occupied Gd 4f band structure.

Because of the high degree of order and the strong texture growth along $(\bar{4}02)$, we have been able to measure the bulk band structure along $\langle \bar{4}02 \rangle$. Because the photoelectrons are collected along the surface normal in the sequence of photon energy dependent photoemission spectra ([Figure 5.1.4](#)), the binding energy shifts of many of the observed photoemission features is indicative of band dispersion along the electron wave vector normal to the surface, k_{\perp} . The value of k_{\perp} can be estimated from the photoelectron kinetic energy making some assumptions about the inner potential U_{in} :

$$k_{\perp} = \sqrt{\frac{2m_e}{\hbar^2} (E_k \cos^2 \theta + U_{in})} \quad (5.1.1)$$

Here E_{kin} is the photoelectron kinetic energy, U_{in} is the inner potential and θ is the emission angle with respect to the surface normal. The dispersion of the component we attribute to the Gd 4f level at 9 to 9.5 eV binding energies is summarized in [Figure 5.1.7](#).

The dependent on photon energy shows that the 4f band critical points repetition, whose spacing in wave vector suggests a periodicity of about $22 \pm 2 \text{ \AA}$ perpendicular to the film or along the surface normal, close to the value of 23.72 \AA expected from the crystallography.

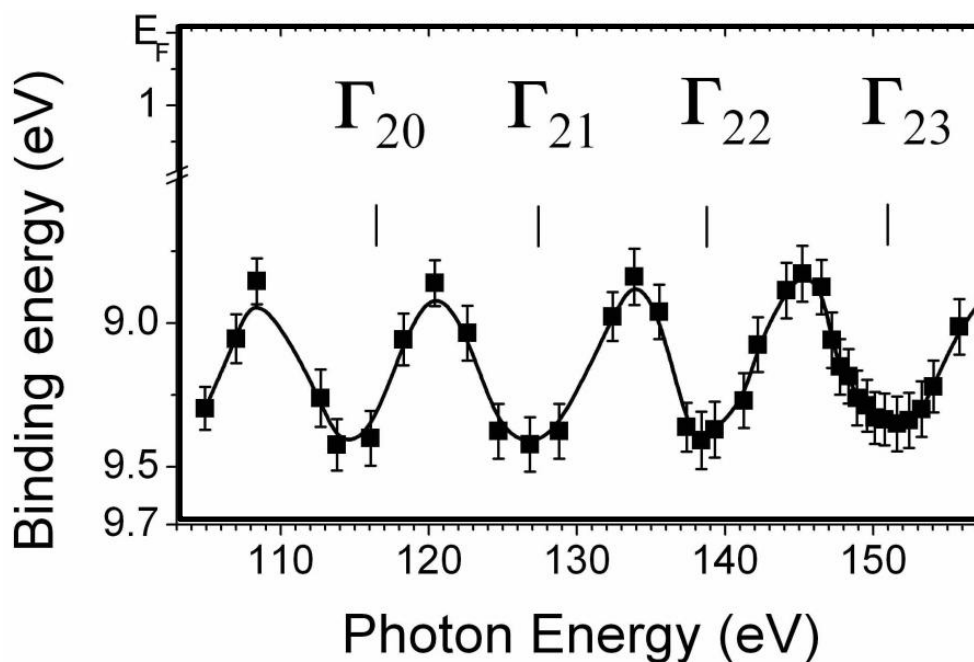


Figure 5.1.7 The dispersion of the Gd 4f component, with changing photon energy. The critical points are indicated, assuming no inner potential and the predicted lattice spacing of 23.7 \AA along $\langle 402 \rangle$.

For a dielectric insulator we would expect that the value of the inner potential to be effectively negligible, as seems to be the case here. We cannot establish that the inner potential to be zero, but from our measurements, that establishes the critical points for the 19th through to the 23rd Brillouin zone, the inner potential is quite small and is no more than 1-2 eV, at most. Assuming a value of zero for the inner potential, and a lattice constant of 23.72 \AA , the calculated critical points show very good agreement with the

experimental band structure, as indicated in [Figure 5.1.7](#).

What is clear is that we have strong Gd 4f hybridization with the oxygen in both Gd_2O_3 and Gd-doped HfO_2 films, and we have a small amount of band dispersion in the band strongly weighted with a Gd 4f contribution for Gd_2O_3 . The band dispersion is small (about 500 meV), but evident nonetheless, as in the case of Ce [[17](#), [18](#)] and Yb [[19](#)] compounds. The Gd 4f weighted bands exhibit band structure yet are placed well away from the Fermi level in the valence band of Gd_2O_3 .

The band width is about 0.5 eV, which is less than the full Gd 4f line width in Gd_2O_3 , but nonetheless about what is expected from the calculated band width from projected augmented wave method and the generalized gradient approximation (GGA-PBE). What is perhaps surprising is that that we are able to identify this band structure experimentally even though there are some 84 gadolinium bands. This implicates that photoemission selection rules play a role. Such selection rules are indeed likely.

The unoccupied 4f levels of Gd_2O_3 also have some band width. From the width of the resonant intensities due to the $4d^{10}4f^7 \rightarrow 4d^94f^8 \rightarrow 4d^{10}4f^6 + e^-$ super Coster-Kronig transition occurring at about 150-152 eV, we can see that the width of this resonant enhancement occurs for a far larger range of photon energies for Gd_2O_3 than is the case for 3% Gd doped HfO_2 ([Figures 5.1.5 \(a\)](#) and [Figure 5.1.5 \(b\)](#) respectively). Since Gd_2O_3 and HfO_2 have very similar band gaps (5.4 and 5.7 eV respectively), the pronounced differences in the position of the maximum resonance and the width of the resonance suggest that the unoccupied Gd 4f bands of Gd_2O_3 have greater band width than is the case for the unoccupied states of Gd in HfO_2 . As was noted for ErAs [[20](#), [21](#)], we expect the unoccupied 4f levels to exhibit dispersion and contribute to the band width

of the unoccupied states.

5.1.2 Heterojunctions using Silicon as a p-type or n-type Substrate

To illustrate the overcompensation of the Gd acceptor states by oxygen vacancies, several diodes were constructed. For 3 % Gd doping levels [2], the Gd acceptor states are overcompensated and doped hafnium oxide forms a rectifying diode on *p*-type silicon, this is not sustained at the higher Gd doping level of 10 % [1]. At this doping level Gd acceptor states are not compensated by oxygen vacancies, leading to a failure in obtaining an heterojunction diode when using *p*-type silicon as shown in [Figure 5.1.8 \(b\)](#). However, if the substrate is replaced by *n*-type silicon, a rectifying structure is recovered. One must keep in mind that this data do not conclusively show the dominant carrier. However, it suggest that oxygen vacancies can overcompensate the Gd acceptor states while retaining semiconducting properties as seen for 3% Gd doping levels.

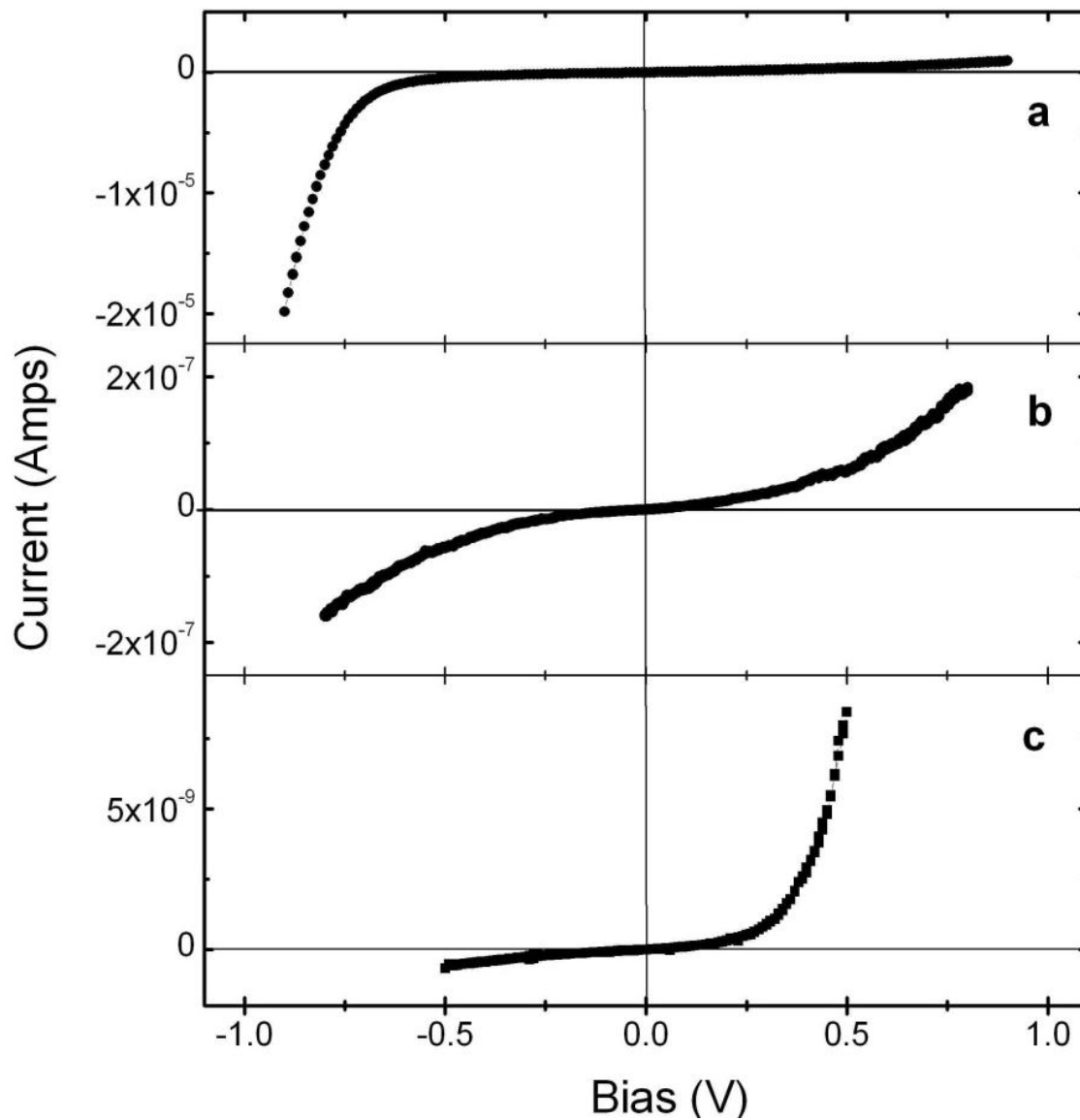


Figure 5.1.8 A heterojunction diode constructed from Gd-doped HfO_2 on silicon, for various Gd-doping concentrations. With oxygen vacancies, the Gd doping generated acceptor states, in 3% Gd-doped HfO_2 , are over compensated and doped hafnium oxide forms a rectifying diode on p -type silicon (a). The 10% Gd-doped HfO_2 is not overcompensated by oxygen vacancies and does not form a rectifying diode on p -type silicon (b) but does do so on n -type silicon (c). Taken from [28].

5.2 The Effect of Rare Earth Doping (Gd and Ce) in the Electronic Band Structure of EuO Films

Europium oxide is a well-known ferromagnetic semiconductor and a candidate for spin filter barrier materials. Stoichiometric EuO has a Curie temperature (T_C) of 69 K, which is strongly enhanced by electron doping via rare-earth substitution or oxygen vacancies. Furthermore, such doping can tune the conductivity of EuO to match that of silicon. Both oxygen deficiency and Gd doping are expected to introduce *n*-type donors in EuO, but their effects may be somewhat different.

5.2.1 The Valence Band, Conduction Band and Filling of Electron Pockets

The valence band photoemission (ARPES) spectra for both doped and undoped EuO films are shown in [Figure 5.2.1](#). These spectra exhibit photoemission features attributable to the Eu 4*f* states near the Fermi level and the O 2*p* states at about 4-6 eV below the Fermi level. The binding energy of the O states is consistent with GW calculations [22], while LSDA or LSDA+U calculations place the binding energy of the O states significantly closer to the Fermi level [23-30]. The binding energies of Eu 4*f* and oxygen 2*p* orbitals are also consistent with previous photoemission studies of undoped EuO films [31-33]. The splitting of the Eu 4*f* states in the photoemission spectra has been previously reported [39], and in those high resolution photoemission studies, the splitting was clearly resolved at the surface Brillouin zone center ($\bar{\Gamma}$) for undoped EuO(100).

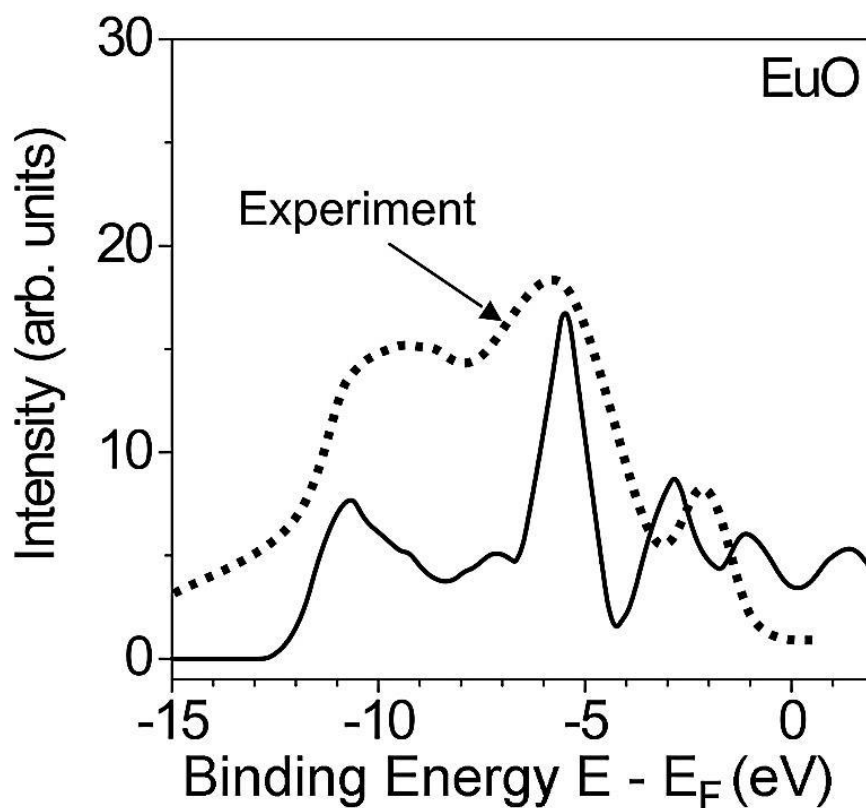


Figure 5.2.1. The simulated (solid line) and experimental (dashed line) photoemission spectra for undoped EuO, with corrections for the combined excited-state density of states. The DFT/GGA calculations of density of states (DOS) were performed with fixed occupancies for treating the excited states.

The features observed in photoemission spectra are usually wider than the corresponding peaks in the calculated density of states (DOS). The broadening of the photoemission features in the energy range corresponding to the valence band results from various solid state effects. Strong contributions have been generally attributed to final-state effects, such as (i) existence of several nearly degenerated excited states; (ii) presence of the OVV Auger peaks; (iii) shake-down satellites of the $5p$ line ("replicas") [34, 35]. In addition, for a $4f$ system, the relative heights of the f and d photoemission peaks strongly depend on the photon energy, so that for moderate photon energies 30-50

eV [36-38], when the cross-section for f electrons is relatively small, the height of the f -derived peak is also small. Thus there are a number of complications in making a direct comparison of the photoemission spectra with the calculated ground state DOS. Nonetheless, in most cases the main features of the calculated occupied DOS represent appropriate initial states generating the corresponding peaks in the photoemission spectra.

The broad feature in the photoemission spectra of EuO at binding energies of more than 8 eV below E_F cannot be explained as states originating from O $2p$ orbitals only. There are a number of possible explanations including photoexcitation of $5s$ or $5p$ electrons of Eu, which can be followed by the OVV Auger decay leading to the appearance of the $4f^6 5d^1 6s^2$ electronic configuration. Specifically, in the presence of the p hole, the $4f - 5d$ excitation and then the $5d - 5p$ Coster-Kronig transition can affect the emission of another $4f$ electron, which leads to formation of a $2+$ ion with the $4f^5 5d^0 6s^2$ electronic configuration, responsible for the multiplet structure of the photoemission spectra. Screening by itinerant electrons will result in the $4f^6 5d^1 6s^2$ configuration, thus providing the accumulation of excited atoms, which can give rise to the -8 eV or greater binding energy features in photoemission spectra.

The excited state spin-polarized calculations were carried out with ABINIT code [45], using norm-conserving Troullier-Martins pseudopotentials [46], with the Perdew-Burke-Ernzerhof (PBE) form of GGA exchange-correlation functional [47], in order to model the actual photoemission spectra. The f states, as well as semi-core or shallow core $5p$ states of Eu were treated as bands. The approximate 1×10^{-3} Hartree (Ha) convergence was achieved with the energy cut-off 40 Ha and $4 \times 4 \times 4$ Monkhorst-Pack [39] set of k

points. The DOS were calculated with the tetrahedron method. The estimated lattice period for fcc EuO (rocksalt structure) was $a = 5.24 \text{ \AA}$, in reasonable ($\sim 2\%$) agreement with experimental value 5.131 \AA [40, 41]. The formation of the peaks in DOS, induced by excitations, was addressed by using the method of self-consistent band structure calculations with fixed occupation numbers [42, 43]. Specifically, the spin-up and spin-down occupation numbers for each band at each k-point are given explicitly and remain unchanged. The fixed occupation numbers prevent interband transitions, which otherwise would unavoidably end with the electron distribution inherent for the ground state, and allows for estimates of excited states by means of routine self-consistent calculations. By adopting appropriate broadening of the DOS features (the widths of the spectral peaks are difficult to estimate rigorously because of unknown lifetimes of the excited states), it is possible to simulate the photoemission spectra, obtaining a reasonable agreement with experiment (Figure 5.2.1).

The normal configuration of the Eu atom is $4f^7 6s^2$, and, according to Hund's rule, all $4f$ electrons have a spin-up orientation, which leads to a ferromagnetic (FM) ground state also for EuO. Spin-flip transitions like the $4f \uparrow - 5d \downarrow$ transition in a Eu atom will result in the formation of the excited state. When the spin-flip transition ends with the occupation of the lowest spin-down band (vacant before the transition), the produced excited state will be metastable due to the spin-conservation rule.

In the excited state calculation, there are two features that originate from Eu $4f$ states: the one at 1 eV is mostly from the ground-state Eu $4f^7$ configuration, while the strong satellite feature is due to excited states as a result of two-hole bound states which

include spin-flip scattering. The feature at about 5.5 eV in [Figure 5.2.1](#) results from the oxygen O $2p$ states, while the features at 7 eV to 11 eV stem from a variety of multi-configurational excited states and satellite features. Thus, the peaks in the valence band photoemission spectra at binding energies of more than 8 eV away from the Fermi level can be explained by photoemission from excited states of EuO. An adroit choice of the pseudo-potential, in the excited state calculation, results in a placement of the O states with the binding energies in good agreement with experiment.

Although the $\text{Eu}_{0.96}\text{Gd}_{0.04}\text{O}$ films have only a small fraction of Gd in the lattice, there should be a strong Gd $4f$ contribution at a binding energy of about -9 eV [[33-35](#), [1](#), [55](#)]. This contribution becomes evident at photon energies corresponding to the $4d \rightarrow 4f$ super Coster-Kronig resonance, as in the case of 3% Gd doped HfO_2 [[33](#), [35](#), [55](#)], but with far less resonant enhancement in the case of $\text{Eu}_{0.96}\text{Gd}_{0.04}\text{O}$. Indeed, the Gd contribution to the bottom of the valence band, at photon energies off resonance in the case of $\text{Eu}_{0.96}\text{Gd}_{0.04}\text{O}$, is more difficult to discern.

The unoccupied spectrum in [Figure 5.2.2](#), dominated by Eu $5d$ states at the conduction band minimum, is consistent with the reported [[44](#)] oxygen K-edge absorption spectrum of EuO. Combined with the angle-resolved core-level XPS (not shown) this consistency confirms the stoichiometry of the EuO surface (IPES is extremely surface sensitive). The electronic band gap for the undoped EuO derived from the combined UPS/ARPES and IPES spectra is about 1.5 eV, slightly wider than the optical band gap of 1.1 eV to 1.2 eV [[45](#)]. Since EuO has an indirect band gap (see [[37](#)] and below), angle resolved photoemission and IPES, set up in a manner that

preferentially samples the center of the surface Brillouin zone, are expected to give a larger band gap corresponding to the band structure at $\bar{\Gamma}$. The placement of the Fermi level close to the conduction band minimum is consistent with an n-type surface, likely due to oxygen vacancies in the lattice.

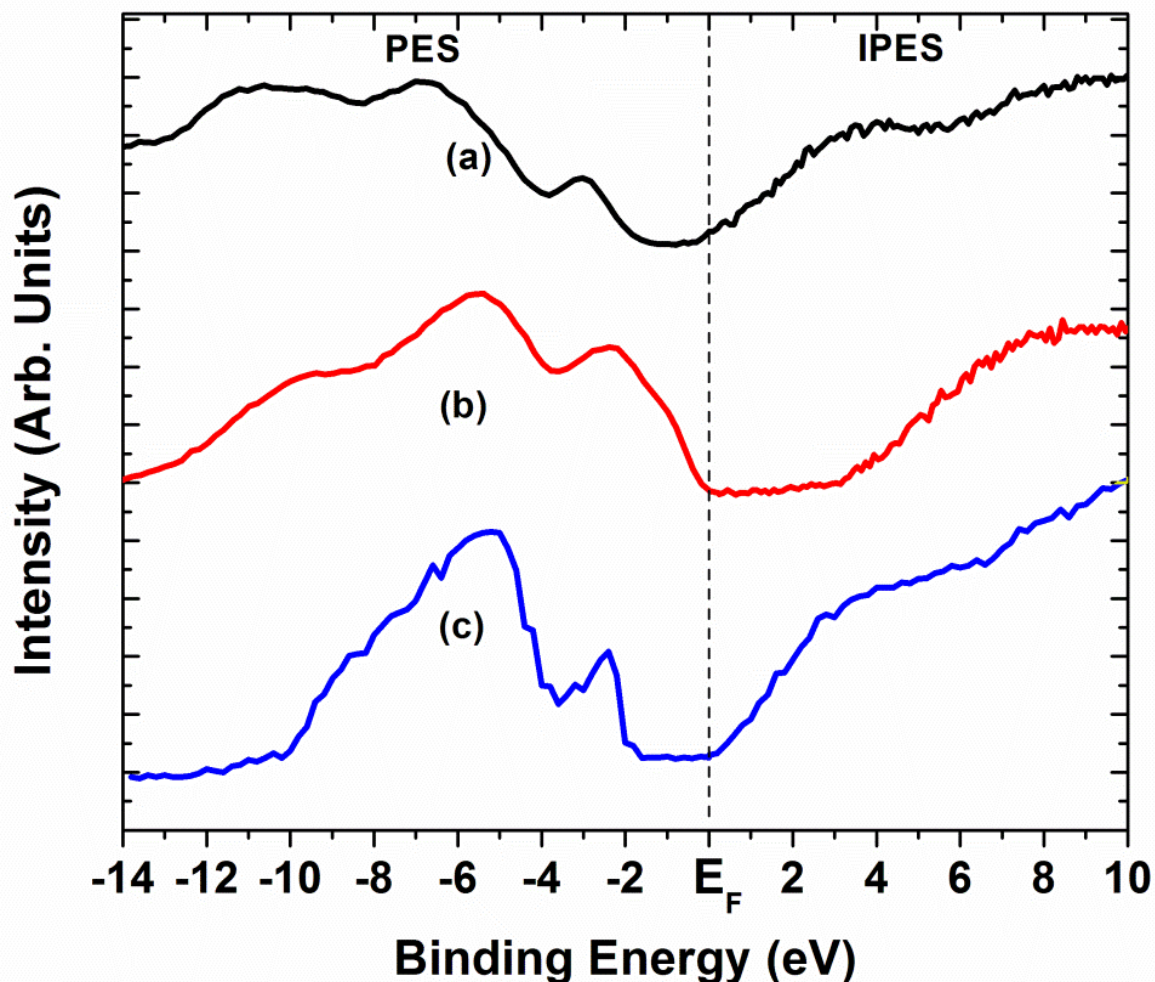


Figure 5.2.2 Combined ARPES and IPES spectra for (a) undoped EuO film, (b) $\text{Eu}_{0.96}\text{Gd}_{0.04}\text{O}$ (111) film, and (c) same as (b) but after sputtering. A photon energy of 60 eV was used, with light incident at 45° and photoelectrons collected along the surface normal. For the IPES spectra the electrons are incident along the surface normal.

The main effect of Gd doping is the appearance of new occupied states in the spectrum near the Fermi energy, as seen in [Figure 5.2.2](#). As long as the film is sufficiently crystalline, the ARPES measurements can be used to resolve the spectral intensity by the wave vector component normal to the surface k_{\perp} [[20](#), [21](#), [33](#), [35](#), [46](#), [47](#), [58](#), [59](#)], as in equation 5.1.1 and discussed above. Band structure calculations for EuO based on the highly reliable GW method [[37](#)] have shown that the conduction band bottom is at the X point, while the minimum at Γ is significantly higher. Therefore, we expect that under 4% Gd doping the extra carriers will go into the electron pockets at the X points. This expectation was previously confirmed with 2% cerium doping [[48](#)], and the present results provide further evidence for Gd:EuO, as we now explain.

The position of occupied states near the Fermi edge for the $\text{Eu}_{0.96}\text{Gd}_{0.04}\text{O}(111)$ deposited on Si(100) does show wave vector dependence. By varying the photon energy from 50 eV to 158 eV, significant dispersion with k_{\perp} (corresponding to the bulk [111] direction) was observed, as seen in [Figure 5.2.3](#). The spectral intensity at the Fermi level, which is plotted in [Figure 5.2.4](#), reaches a maximum at the photon energy corresponding to the bulk Γ point.

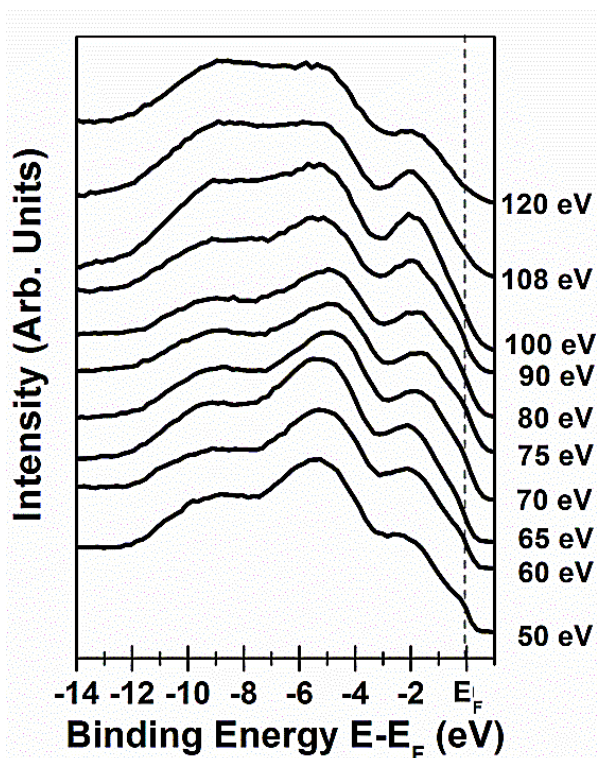


Figure 5.2.3 The photoemission spectra obtained for $\text{Eu}_{0.96}\text{Gd}_{0.04}\text{O}$ (111) films as a function of the photon energy. The angle of incidence was 45° and all photoelectrons were collected along the surface normal at $T = 300\text{ K}$.

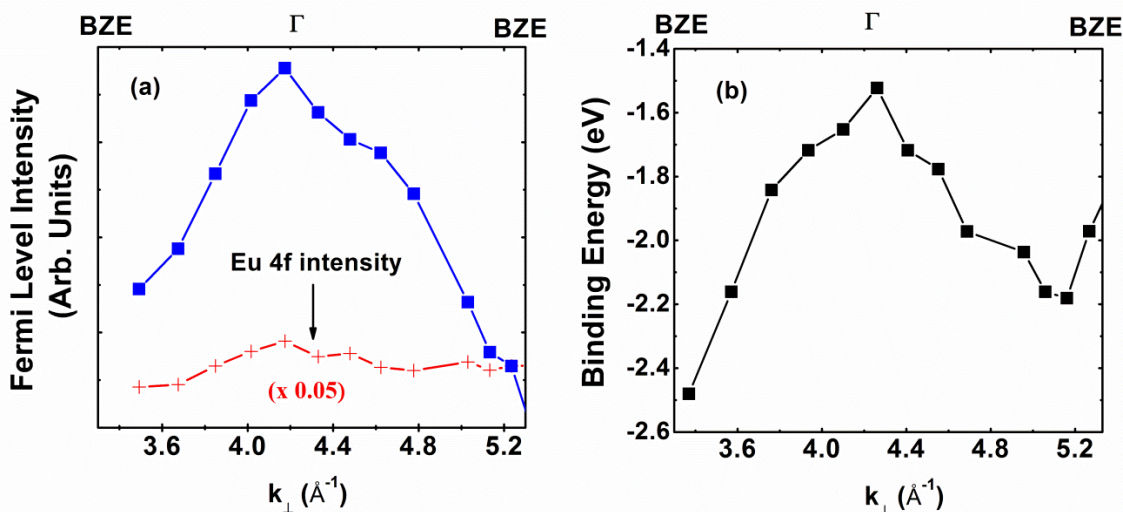


Figure 5.2.4 (a) The Fermi level intensity (*blue*) plotted as a function of k_{\perp} , along the [111] direction. (b) The dispersion of the Eu 4*f* weighted band at the valence-band maximum, along the (111) direction or wave vector normal to the surface, k_{\perp} . Both results were extracted from the photon energy dependent ARPES spectra. BZE indicates the Brillouin-zone edge. The intensity of the Eu 4*f* weighted band (+), at the valence-band maximum, along the k_{\perp} (111) direction, is also plotted in (a).

The measured values of k_{\perp} at the band structure critical points are consistent with the lattice constants corresponding to the (111) texture determined from XRD. This increase in the intensity at Γ near the Fermi level is consistent with the spectral "tail" extending from the states at the top of the valence band, which is at the Γ point. This is more evident in the analysis of the band dispersion parallel to the surface, discussed below. This band structure related effect occurs at photon energies corresponding to the Γ points at photon energies well below those that correspond to the $4d \rightarrow 4f$ super Coster-Kronig resonance [56].

Even though our Si(100)/Eu_{0.96}Gd_{0.04}O(111) films are not single crystals, they are sufficiently ordered to manifest band dispersion also parallel to the surface along the $\overline{\Gamma M}$ of the surface Brillouin zone. Indeed, high-resolution photoemission in the transmission mode (of the spectrometer) reveals a variation of the spectral intensity as a function of the parallel momentum component k_{\parallel} , which is given by [20, 21, 58-59]:

$$k_{\parallel} = \sqrt{\frac{2m_e}{\hbar^2} E_K} \sin \theta \quad (5.2.2)$$

The k_{\parallel} -resolved spectral intensity in the vicinity of the Fermi level is plotted in [Figure 5.2.5](#). The spectral intensity is seen to depend both on the photon energy and on the emission angle θ . This photon energy dependence at the surface Brillouin zone edge is consistent with the location of the electron pocket at the X point. At 40 eV photon energy the spectral intensity indicates a band crossing on both sides of the surface Brillouin zone edge. At slightly higher binding energies (~ 300 meV below the Fermi level) the intensity

maxima move closer to the X point, consistent with the parabolic dispersion of the electron pocket. The fact that the intensities sharply increase at the $\bar{\Gamma}_1$ points, as we move down from the Fermi level indicates that this intensity represents the spectral tail from the valence band maximum at Γ , rather than the conduction band states. At a photon energy of 25 eV, corresponding to a lateral shift from the X point along the face of the Brillouin zone, the cut through the bulk band structure has the electron pocket just touching the Fermi level.

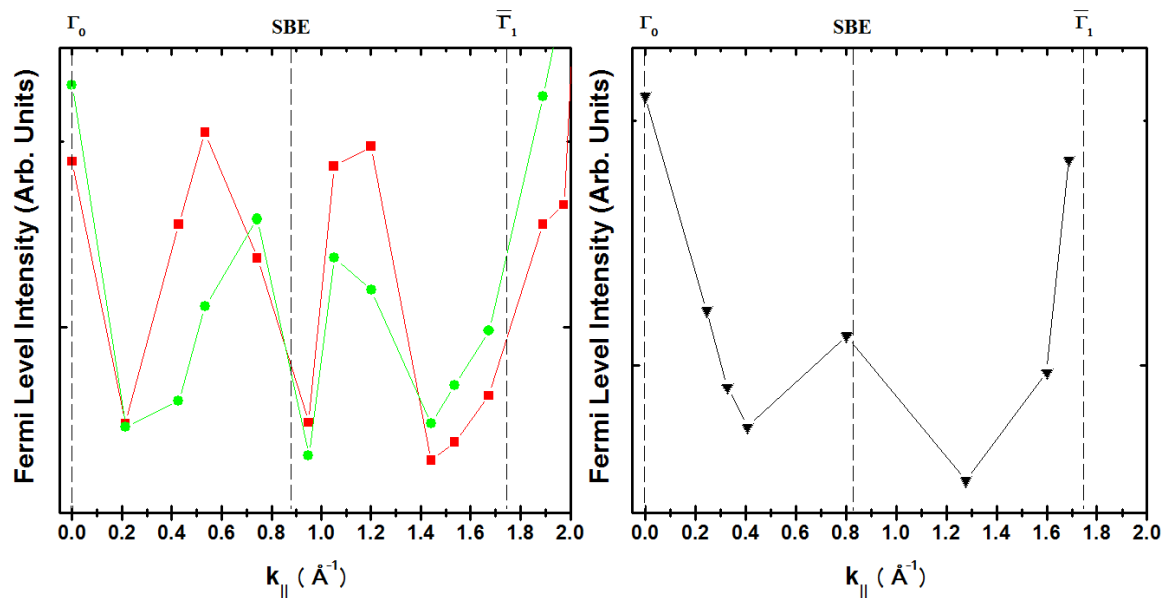


Figure 5.2.5 The Fermi-level intensity plotted as a function of the parallel momentum $k_{||}$ along the ΓM direction, for photon energies of (a) 40 eV and (b) 25 eV. For $k_{||}$ along the ΓM direction, the relative intensity has been also plotted 300–400 meV below the Fermi level (green) and at the Fermi level (red), to illustrate the roughly parabolic shape of the electron pocket about the surface Brillouin-zone edge at 40 eV.

5.2.2 Band Bending at the Gd:EuO (111) Polar Surface

In the combined ARPES and IPES spectra shown in [Figure 5.2.2](#) the $\text{Eu}_{0.96}\text{Gd}_{0.04}\text{O}$ (111) surface appears to be p -type. At first sight this feature contradicts the observation of filled electron pockets at the X point and the n -type character expected of

a material dominated by substitutional Gd dopants and oxygen vacancies, both of which are electron donors. The apparent *p*-type character of this electron-doped sample can only be explained by band bending near the surface, which reveals the presence of a volume charge there. Specifically, the electrostatic potential near the surface is lowered relative to the bulk, which means that the surface itself is negatively charged.

The presence of uncompensated charge at the (111) surface of a rocksalt oxide is not surprising, because this surface orientation is polar. Normally this orientation is unfavorable, because it requires extensive surface reconstruction or charged defects to screen the electric field in the bulk. However, in the metallic electron-doped sample the free carriers are available to screen the surface charge. It is possible that this screening explains the stabilization of the (111) surface orientation in our Gd-doped EuO samples relative to the (001) orientation preferred by the insulating EuO.

Negative charge of the (111) surface strongly suggests its over-oxidation. This is natural for EuO, which in the presence of sufficient oxygen readily oxidizes to Eu₂O₃. For undoped EuO this would result in a mixed 2⁺/3⁺ Eu valence at the surface accompanied by the appearance of unfilled 4*f* states. Since such unfilled states are absent in the IPES spectrum, we conclude that the band bending does not exceed the bulk band gap, and that the Eu 4*f* states are kept fully filled by the free carriers introduced by electron doping. To summarize, we argue that the moderately over-oxidized, negatively charged surface is accompanied by a positively charged subsurface depletion region. This conclusion is supported by the fact that sputtering of the surface results in a “normal” *n*-type spectroscopic pattern, as seen in [Figure 5.2.2 \(c\)](#). This shift can be explained by the removal of some of the excess oxygen from the surface.

Since the atomic structure of the (111) surface has not been determined, it is not possible to perform an accurate theoretical investigation of its electronic properties. However, in order to gain a crude understanding of the effects of over-oxidation, we first considered an extreme case of a fully O-terminated Eu (111) surface. We chose a 15-monolayer slab consisting of 7 Eu and 8 O monolayers, bisected by a Eu layer, and terminated by O layers on both surfaces. The equilibrium atomic configuration of this slab was found using the projected augmented wave (PAW) method [49, 50] implemented in the VASP package [51, 52]. For the exchange and correlation potential we used the generalized gradient approximation [50], adding the Hubbard U correction [53] for the Eu 4*f* orbitals ($U = 7.5 \text{ eV}$ and $J = 0.6 \text{ eV}$). During the otherwise unrestricted relaxation, the in-plane lattice constants were fixed to their bulk values.

Figure 5.2.6 shows the obtained equilibrium configuration of the slab. The lateral positions of the atoms are fixed by symmetry; the interlayer distances indicated in Figure 5.2.6 are listed in Table 5.2.1.

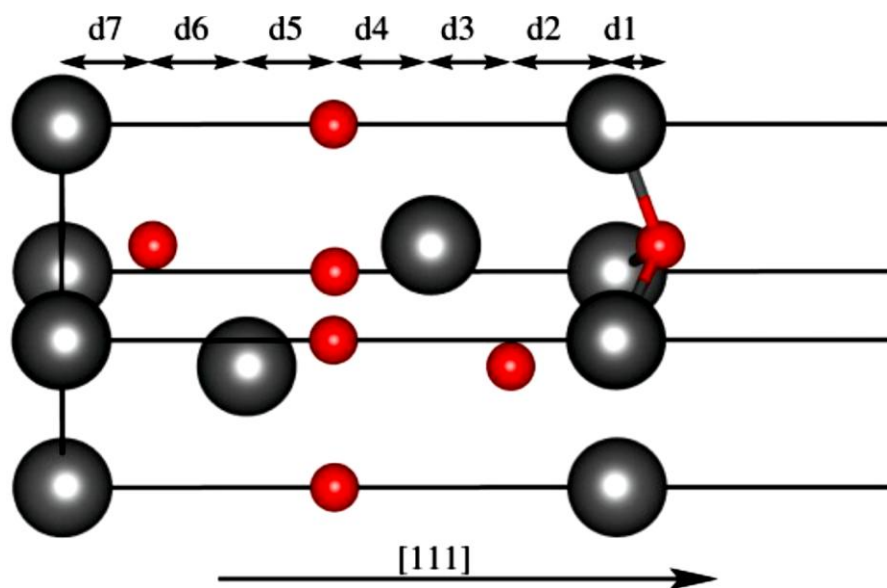


Figure 5.2.6 Calculated structure of the O-terminated EuO(111) surface. Only half of the slab is shown, the other half being symmetric. For interlayer spacings see Table 5.2.1. In the figure, large spheres are Eu atoms; small spheres: O atoms.

There is a very large inward relaxation of the surface O layer (reducing the interlayer distance by nearly a half), along with a significant outward relaxation of the subsurface Eu layer. Changes in the interlayer spacing propagate a few layers into the bulk, but the interlayer spacing in the middle of the slab already deviates by less than 1% from its bulk value. Such oscillatory interlayer spacings are common for polar oxide surfaces [55]

Layer	Labels in Figure 5.2.6	Interlayer Spacing (Å)
surface; Eu-O	d1	0.73
surface-1; O-Eu	d2	1.75
surface-2; Eu-O	d3	1.31
surface-3; O-Eu	d4	1.6
surface-4; Eu-O	d5	1.44
surface-5; O-Eu	d6	1.54
surface-6; Eu-O	d6	1.49

Table 5.2.1 The interlayer spacing calculated for EuO(111) as indicated in Figure 5.2.6. The layer spacings are oscillatory in the region of the surface, as indicated. The layers spacing are giving in units of Å.

To illustrate our interpretation of the band bending near the over-oxidized surface, we considered a somewhat arbitrary, but nonetheless suggestive model, using the tight-binding linear muffin-tin orbital (TB-LMTO) method. A 27-monolayer slab was chosen for this purpose, inserting bulk-like EuO layers in the middle of the relaxed 15-monolayer slab shown in Figure 5.2.6. The parameters of the calculation, such as the atomic sphere radii, the auxiliary empty spheres, and the U and J parameters, were adjusted to reproduce the correct band structure of bulk EuO, including the band gap and the character of the conduction band states. We also added a fictitious external potential of 1.36 eV to the oxygen sites in order to push the O $2p$ states to lower energies. The effect of Gd doping was included in the virtual crystal approximation (VCA), replacing Eu with fictitious atoms with nuclear charge $63.17e$ (corresponding to 17% Gd doping). Even at

this large doping level the negative charge on the O-terminated surface is unrealistically large and results in mixed-valent Eu at the surface. It is clear that the actual amount of surface over-oxidation in our experimental samples is much lower. In order to make our illustration more realistic without considering more complicated surface terminations, we reduced the amount of charge transfer to the surface O layer by replacing the oxygen atoms in this layer by fictitious atoms with nuclear charge $8.40e$.

The partial DOS for all Eu and O atoms of this slab are shown in [Figure 5.2.7](#). The upward band bending near the surface is clearly seen, which results in a structure similar to a p - n junction with a depletion region.

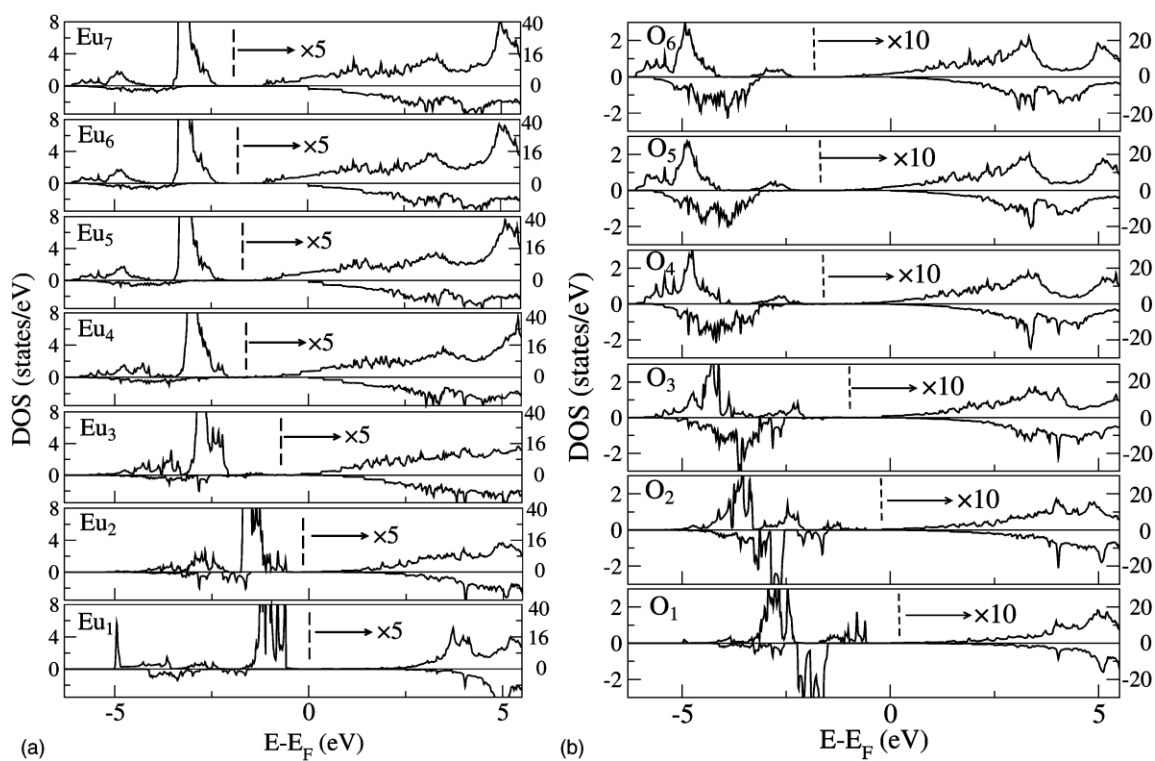


Figure 5.2.7 Site-projected DOS for all Eu and O atoms of the 27-monolayer slab of Gd-doped-EuO with (111) surfaces. A model with empirical adjustments is used (see text). (a) Eu site-projected DOS where the unoccupied DOS is multiplied by 5 (as indicated). (b) O site-projected DOS; unoccupied DOS is multiplied by 10 (as indicated). The numbering of the sites starts at the surface.

5.2.3 Magnetic Dependence in Heterojunction Structures

There is another indication of the band bending of the kind illustrated by [Figure 5.2.2](#). Evidence of the electron pockets at the Fermi level and absence of photovoltaic charging indicate that Gd-doped EuO is metallic. The energy band diagram with a narrow depletion region suggests that, with a suitable interface, the surface region may operate as a tunnel (Esaki) diode with the current flowing perpendicular to the surface (or to the interface with silicon, assuming similar band bending there). This independent signature of surface band bending in the $\text{Eu}_{0.96}\text{Gd}_{0.04}\text{O}(111)$ sample was indeed observed, as seen in [Figure 5.2.8](#). Although very far from ideal, the I-V curve shows a region of negative differential resistance close to a 3.0 V bias. Interestingly, the application of a magnetic field eliminates this region of negative differential resistance (see [Figure 5.2.8 \(b\)](#)). The origin of this effect is not clear, but it may be mediated by the induction of a small exchange splitting in the conduction band through partial ordering of Eu local moments induced by the magnetic field. These effects are not seen with undoped EuO(100) thin films on *p*-type silicon, as indicated in [Figure 5.2.8 \(a\)](#) for comparison, and thus the (111) texture growth and Gd (or similar) doping may be required for tunnel (Esaki) diode behavior. It should be noted that Gd_2O_3 is typically *n*-type in thin film form and forms a heterojunction diode with *p*-type Si(100), but no negative differential resistance has been observed with such structures [33]. Heterostructures of Gd_2O_3 with Si(100) show diode characteristics [19] more similar to undoped EuO/Si(100) heterostructure ([Figure 5.2.8a](#)) than those observed with $\text{Eu}_{0.96}\text{Gd}_{0.04}\text{O}(111)/\text{Si}(100)$ heterostructure ([Figure 5.2.8b](#)).

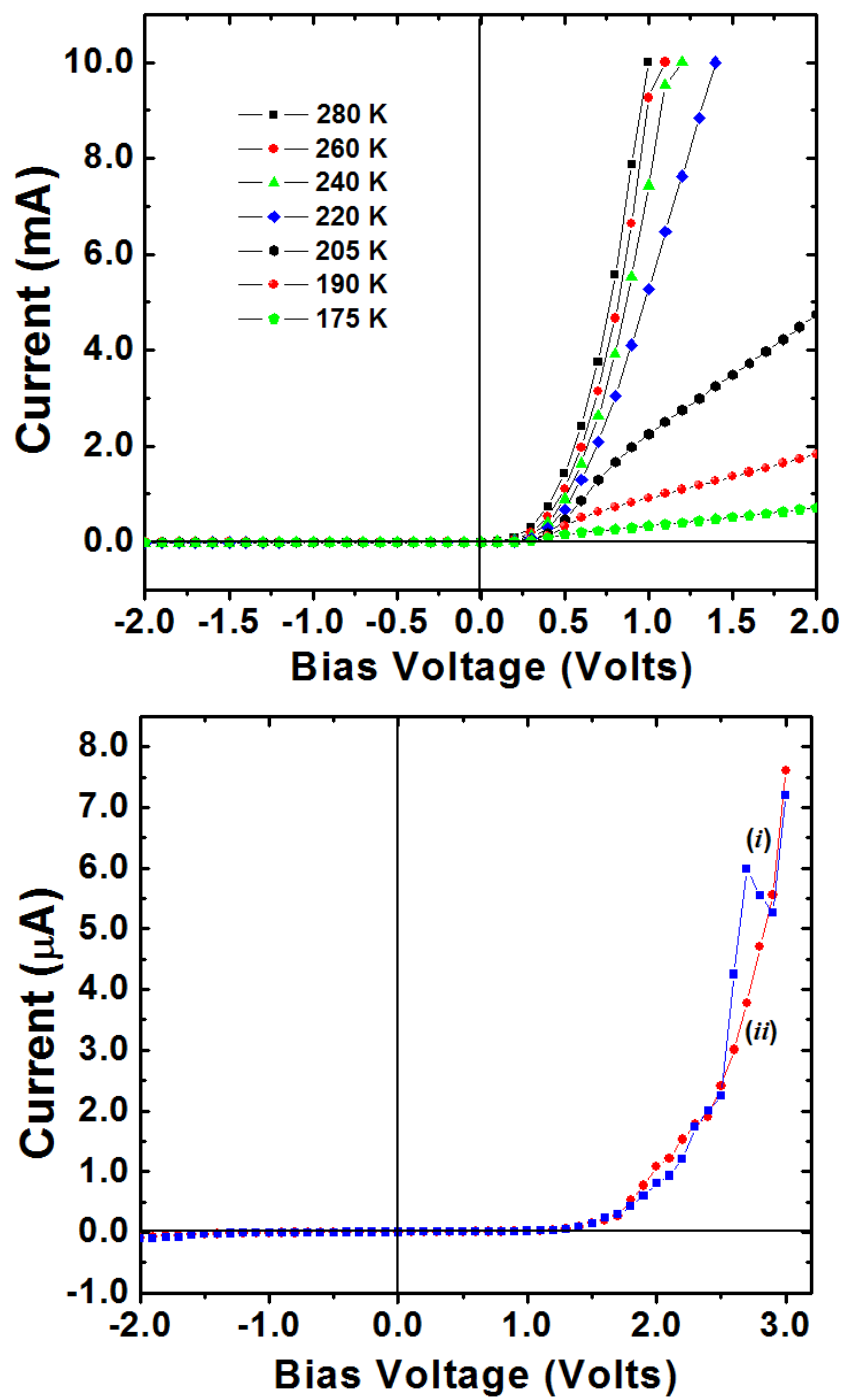


Figure 5.2.8 I-V curves for (a) undoped EuO(100) film as a function of temperature, (b) $\text{Eu}_{0.96}\text{Gd}_{0.04}\text{O}$ (111) film at room temperature. The curve marked (i) is for zero field; the curve marked (ii) is for an external magnetic field of 1000 Oe.

References

- [1] Ya. B. Losovyj, I. Ketsman, A. Sokolov, K.D. Belashchenko, P.A. Dowben, J. Tang and Z. Wang, “The electronic structure change with Gd doping of HfO₂ on silicon”, *Appl. Phys. Lett.* 91 132908 (2007)
- [2] I. Ketsman, Ya. B. Losovyj, A. Sokolov, J. Tang, Z. Wang, K.D. Belashchenko and P.A. Dowben, “The n-type Gd-doped HfO₂ to silicon heterojunction diode”, *Appl. Phys. A* 89 489–92 (2007)
- [3] M. Komatsu, R. Yasuhara, H. Takahashi, S. Toyoda, H. Kumigashira, M. Oshima, D. Kukuruznyak and T. Chikyow, “Crystal structures and band offsets of ultrathin HfO₂–Y₂O₃ composite films studied by photoemission and x-ray absorption spectroscopies”, *Appl. Phys. Lett.* 89 172107 (2006)
- [4] S. Suzer, S. Sayan, M.M. Banaszak Holl, E. Garfunkel, Z. Hussain and N.M. Hamdan, “Soft x-ray photoemission studies of Hf oxidation”, *J. Vac. Sci. Technol. A* 21 106 (2003)
- [5] S. Sayan, T. Emge, E. Garfunkel, X. Zhao, L. Wielunski, R.A. Bartynski, D. Vanderbilt, J.S. Suehle, S. Suzer and M.M. Banaszak Holl, “Band alignment issues related to HfO₂/SiO₂/p-Si gate stacks”, *J. Appl. Phys.* 96 7485 (2004)
- [6] S. Sayan, R.A. Bartynski, X. Zhao, E.P. Gusev, D. Vanderbilt, M. Croft, M.M. Banaszak Holl and E. Garfunkel, “Valence and conduction band offsets of a ZrO₂/SiO_xN_y/n-Si CMOS gate stack: A combined photoemission and inverse photoemission study”, *Phys. Status Solidi b* 241 2246 (2004)
- [7] Andreas Eichler and Georg Kresse, “First-principles calculations for the surface termination of pure and yttria-doped zirconia surfaces”, *Phys. Rev. B* 69, 045402 (2004)
- [8] N. V. Skorodumova, M. Baudin, and K. Hermansson, “Surface properties of CeO₂ from first principles”, *Phys. Rev. B* 69, p. 075401(2004)
- [9] P.A. Dowben, D. Li, J. Zhang and M. Onellion, “Resonant photoemission studies of the thickness dependence of the unoccupied Gd 5d bands”, *J. Vac. Sci. Technol. A* 13 1549 (1995)
- [10] Kachel T, Rochow R, Gudat W, Jungblut R, Rader O and Cabone C, “Spin-resolved-photoemission-spectroscopy study of the giant resonance in Gd overlayers on Fe(100)”, *Phys. Rev. B* 45, 7267–7271 (1992)

- [11] R.F. Sabirianov, W.N. Mei, J. Lu, Y. Gao, X.C. Zeng, R.D. Bolskar, P. Jeppson, N. Wu, A.N. Caruso and P.A. Dowben, “Correlation effects and electronic structure of Gd@C60”, *J. Phys.: Condens. Matter* 19 082201 (2007)
- [12] A.I. Liechtenstein, V.I. Anisimov and J. Zaanen, “Density-functional theory and strong interactions: Orbital ordering in Mott-Hubbard insulators”, *Phys. Rev. B* 52 R5467 (1995)
- [13] Kresse G and Joubert D, “From ultrasoft pseudopotentials to the projector augmented-wave method”, *Phys. Rev. B* 59 1758 (1999)
- [14] Duan C-G, Sabiryanov R F, Liu J, Mei W N, Dowben P A and Hardy J R, “Strain Induced Half-Metal to Semiconductor Transition in GdN”, *Phys. Rev. Lett.* 94 237201 (2005)
- [15] McIlroy D N, Waldfried C, Li D, Pearson J, Bader S D, Huang D-J, Johnson P D, Sabiryanov R F, Jaswal S S and Dowben P A, “Oxygen Induced Suppression of the Surface Magnetization of Gd(0001)”, *Phys. Rev. Lett.* 76 2802–5 (1996)
- [16] Schussler-Langeheine C, Meier R, Ott H, Hu Z, Mazumdar C, Grigoriev A Y, Kaindl G and Weschke E, “Magnetically ordered surface oxide on Gd (0001)”, *Phys. Rev. B* 60 3449–52 (1999)
- [17] ImH J, Ito T, KimH D, Kimura S, Lee K E, Hong J B, Kwon Y S, Yasui A and Yamagami H, “Direct Observation of Dispersive Kondo Resonance Peaks in a Heavy-Fermion System”, *Phys. Rev. B* 100 176402 (2008)
- [18] Andrews A B, Joyce J J, Arko A J and Fisk Z, “Momentum-dependent effects in 4f photoemission spectra from strongly correlated CeBe₁₃”, *Phys. Rev. B* 53 3317 (1996)
- [19] Vyalikh D V, Danzenbacher S, Yaresko A N, Holder M, Kucherenko Y, Laubschat C, Krellner C, Hossain Z, Geibel C, Shi M, Patthey L and Molodtsov S L, “Photoemission Insight into Heavy-Fermion Behavior in YbRh₂Si₂”, *Phys. Rev. Lett.* 100 056402 (2008)
- [20] Komesu T, Jeong H-K, Choi J, Borca C N, Dowben P A, Petukhov A G, Schultz B D and Palmstrøm C J, “Electronic structure of ErAs (100)”, *Phys. Rev. B* 67 035104 (2003)
- [21] Duan C-G, Komesu T, Jeong H-K, Borca CN, Yin W-G, Liu J, Mei WN, Dowben PA, Petukhov AG, Schultz BD and Palmstrøm CJ, “Hybridization between 4f-5d States in ErAs(100)”, 2004 *Surf. Rev. Lett.* 11 531–9

- [22] J.M. An, S.V. Barabash, V. Ozolins, M. van Schilfgaarde, and K.D. Belashchenko, “First-principles study of phase stability of Gd-doped EuO and EuS”, *Phys. Rev. B* 83, 064105 (2011)
- [23] M. Barbagallo, N. D. M. Hine, J. F. K. Cooper, N.-J. Steinke, A. Ionescu, C. H. W. Barnes, C. J. Kinane, R. M. Dalgliesh, T. R. Charlton, and S. Langridge, “Experimental and theoretical analysis of magnetic moment enhancement in oxygen-deficient EuO”, *Phys. Rev. B* 81, 235216 (2010)
- [24] P. Larson and W. R. L. Lambrecht, “Electronic structure and magnetism of europium chalcogenides in comparison with gadolinium nitride”, *J. Phys.: Condens. Matter* 18, 11333 (2006).
- [25] R. Schiller and W. Nolting, “Temperature-dependent band structure of bulk EuO”, *Solid State Commun.* 118, 173 (2001).
- [26] J. Kunes, W. Ku, and W. P. Pickett, *J. Phys. Soc. Jpn.* 74, 1408 (2005).
- [27] D. B. Ghosh, M. De, and S. K. De, “Electronic structure and magneto-optical properties of magnetic semiconductors: Europium monochalcogenides”, *Phys. Rev. B* 70, 115211 (2004).
- [28] N. J. C. Ingle and I. S. Elfimov, “Influence of epitaxial strain on the ferromagnetic semiconductor EuO: First-principles calculations”, *Phys. Rev. B* 77, 121202(R) (2008).
- [29] R. Schiller, O. Myrasov, A. J. Freeman, and W. Nolting, *J. Magn. Magn. Mater.* 226, 388 (2001).
- [30] H. Miyazaki, T. Ito, H. J. Im, S. Yagi, M. Kato, K. Soda, and S. Kimura, “Direct Observation of Momentum-Dependent Exchange Interaction in a Heisenberg Ferromagnet”, *Phys. Rev. Lett.* 102, 227203 (2009).
- [31] H. Miyazaki, T. Ito, S. Ota, H. J. Im, S. Yagi, M. Kato, K. Soda, and S.-I. Kimura, “Angle-resolved photoemission study on EuO thin films”, *Physica B* 403, 917 (2008).
- [32] P. Munz, “Photoemission Spectroscopy on Europium Chalcogenides, *Helv. Phys. Acta* 49, 281 (1976).
- [33] D.E. Eastman, F. Holtzberg, and S. Methfessel, “Photoemission Studies of the Electronic Structure of EuO, EuS, EuSe, and GdS”, *Phys. Rev. Lett.* 23, 226 (1969)

- [34] S. Haffner, C. G. Olson, and D. W. Lynch, “Evidence for replicate 5p core levels in photoelectron spectra of Eu metal due to nonconstant kinetic-energy resonant Auger decay”, *Phys. Rev. B* 60, 16346 (1999)
- [35] D.M. Wieliczka, C.G. Olson, and D.W. Lynch, “Valence-Band Photoemission in La and Pr: Connections with the Ce Problem”, *Phys. Rev. Lett.* 52, 2180 (1984).
- [36] X. Gonze, J.-M. Beuken, R. Caracas, F. Detraux, M. Fuchs, G.-M. Rignanese, L. Sindic, M. Verstraete, G. Zerah, F. Jollet, M. Torrent, A. Roy, M. Mikami, Ph. Ghosez, J.-Y. Raty, and D. C. Allan, “First-principles computation of material properties: the ABINIT software project ”, *Comput. Mater. Sci.* 25, 478 (2002).
- [37] N. Troullier and J. L. Martins, “Efficient pseudopotentials for plane-wave calculations 15”, *Phys. Rev. B* 43, 1993 (1991).
- [38] J. P. Perdew, K. Burke, and M. Ernzerhof, “Generalized Gradient Approximation Made Simple”, *Phys. Rev. Lett.* 77, 3865 (1996).
- [39] H. J. Monkhorst and J. D. Pack, “Special points for Brillouin-zone integrations*”, *Phys. Rev. B* 13, 5188 (1976).
- [40] X. Wang, P. Liu, K. A. Fox, J. Tang, J. A. Colón Santana, K. Belashchenko, P. A. Dowben, and Yu Sui, *IEEE Trans. Magn.* 46, 1879 (2010).
- [41] P. Wachter, in *Handbook on the Physics and Chemistry of Rare Earths*, edited by K. A. Gschneidner and L. Eyring (Elsevier, Amsterdam, 1979), Vol. 2.
- [42] N.Wu, D. LaGraffe, I. N. Yakovkin, and P. A. Dowben, “Localization and screening in GdNi alloy films”, *Phys. Status Solidi B* 248, 1253 (2011).
- [43] I. N. Yakovkin, “Valence of “divalent” rare earth metals”, *Appl. Surf. Sci.* 256, 4845 (2010).
- [44] P. G. Steeneken, L. H. Tjeng, I. Elfimov, G. A. Sawatzky, G. Ghiringhelli, N. B. Brookes, and D.-J. Huang, *Phys. Rev. Lett.* 88, 047201 (2002).
- [45] J. O. Dimmock, “Optical Properties of the Europium Chalcogenides ”, *IBM J. Res. Dev.* 14, 301 (1970).
- [46] E.W. Plummer and W. Eberhardt, “Angle-Resolved Photoemission as a Tool for the Study of Surfaces”, *Adv. Chem. Phys.* 49, 533 (1982).

- [47] N.V. Richardson and A. M. Bradshaw, in *Electron Spectroscopy: Theory, Techniques and Applications*, edited by C. R. Brundle and A. D. Baker (Academic, San Diego, 1984), Vol. 4, p. 153.
- [48] P. Liu, J. Tang, J. A. Colón Santana, K. Belashchenko, and P. A. Dowben, “Ce-doped EuO: Magnetic properties and the indirect band gap”, *J. Appl. Phys.* 109, 07C311 (2011).
- [49] P.E. Blochl, “Projector augmented wave method”, *Phys. Rev. B* 50, 17953 (1994).
- [50] G. Kresse and D. Joubert, “From Ultrasoft Pseudopotentials to the Projector Augmented-wave Method”, *Phys. Rev. B* 59, 1758 (1999)
- [51] G. Kresse and J. Hafner, “Ab initio molecular dynamics for open-shell transition metals”, *Phys. Rev. B* 48, 13115 (1993)
- [52] G. Kresse and J. Furthmüller, “Efficiency of ab-initio total energy calculations for metals and semiconductors using a plane-wave basis set”, *Comput. Mater. Sci.* 6, 15 (1996)
- [53] G. Kresse and J. Furthmüller, “Efficient iterative schemes for ab initio total-energy calculations using a plane-wave basis set”, *Phys. Rev. B* 54, 11169 (1996)
- [54] A. I. Liechtenstein, V. I. Anisimov, and J. Zaanen, “Density-functional theory and strong interactions: Orbital ordering in Mott-Hubbard insulators”, *Phys. Rev. B* 52, R5467 (1995)
- [55] C. Noguera, “Polar oxide surfaces”, *J. Phys.: Condens. Matter* 12, R367 (2000)

Chapter 6

The Local Metallicity of Gadolinium doped Compound Semiconductors

“Not everything that can be counted counts, and not everything that counts can be counted”

-Albert Einstein-

Evidence of the non-metal to metal transition was found on the electronic band structure mapping along both k_{\perp} and k_{\parallel} . However, constant initial state spectroscopy (CIS) measurements seem to suggest a correlation between the effective screening in the films and the resonant photoemission process. This chapter provides an overview of experiments made to determine differences in the local metallicity of $\text{Hf}_{0.97}\text{Gd}_{0.03}\text{O}_2$, $\text{Ga}_{0.97}\text{Gd}_{0.03}\text{N}$, $\text{Eu}_{0.97}\text{Gd}_{0.04}\text{O}$ and EuO films by characterizing the resonant enhancements in the photoemission features corresponding to the $4d \rightarrow 4f$ transitions in both Eu and Gd.

6.1 Resonant Photoemission as a Probe for Local Metallicity

Photoemission spectroscopy (PES) can provide compelling evidence regarding metallicity using criteria's based on density of states near or at the Fermi level. For instance, while angle resolved photoemission (ARPES) provide means of extending the electronic band structure mapping on reciprocal space, allowing for the detection of a Fermi level crossing (which is a characteristic feature of a metal), X-ray photoemission have been used indirectly as a probe for the metal to non-metal transition by means of the core level line shape and binding energy (but this is not always possible [1, 2]). The use of resonant photoemission has been proposed as a useful tool to probe metallicity in thin films [3], especially in films in which giant resonances are due to final state effects.

In the simplest description, it can be assume that for a lattice compose of simple metals, the electrons will be subject to a screened potential of the form

$$U(r) = -\frac{e^2}{r} e^{-l_s r} \quad (6.1.1)$$

as suggested by Mott [4]. It is the screening parameter l_s what plays an important role in determining the metallicity of a system. If the density of state at the Fermi level is small, the effective screening is weak and electrons are likely to remain in a bounded state near the ion site (localized), resulting in an insulating behavior. As the density of state increases, screening effects can eventually dominate the Coulombic interaction, leading to electron itinerancies in the film followed by an increase in metallicity.

In processes such as photoemission, excitons are formed and are expected to be affected by the screening at some extent. Once the insulating system makes the transition to the metallic phase, free carriers are expected to reduce the Coulomb field between the electron and the hole and to shorten the lifetime of the exciton [5, 6]. A core exciton formed by the removal of an electron in the photoemission process can be described qualitatively in the same way [7, 8]. Under this assumption, resonant photoemission can be used to probe the metallicity of a surface at some extent through the relation

$$\frac{1}{l_s} = \frac{I}{I_0} = \sqrt{\frac{m^*}{m_e}} \quad (6.1.2)$$

This suggests that an increased in screening can lead to a diminishing in the photoemission peak intensity. Although experimental data find agreement with the relation in equation 6.1.2, it must be point out that this relation is strictly empirical. Experimental complications are expected when using resonant photoemission to probe metallicity, mainly because of the lack of theoretical support. A metal to non-metal transition is not necessarily identified by the changes in the photoemission intensity. It is highly recommended to seek validation from another technique before attempting a conclusion. In [Section 5.2.1](#) it was recently proved that EuO undergo a non-metal to metal transition with the inclusion of 4% Gd as suggested by the band crossing the Fermi level. It is the intent of this work to provide evidence of the metallicity changes in EuO as compared to $\text{Eu}_{0.96}\text{Gd}_{0.04}\text{O}$ using resonant photoemission.

A major attribute of resonant photoemission is that it allows one to distinguish which valence bands of the semiconductor host have strong rare earth $4f$ and/or simply rare earth weight [9-16]. The $4d - 4f$ photoemission resonances for various rare earth doped GaN thin films (RE = Gd, Er, Yb) have now been reported [17-21], and like studies of Gd doped HfO₂ [16], permits a fairly definitive placement of the rare earth $4f$ states in the valence band. In fact this can be a local probe of charge localization [22]. Here we broaden the concept of screening and metallicity, as probed by resonant photoemission, by comparing the resonant photoemission enhancement of the valence band features of semiconducting Gd_{0.03}Ga_{0.97}N and Gd_{0.03}Hf_{0.97}O₂ to the more metallic Eu_{0.96}Gd_{0.04}O.

6.2 Resonant Photoemission in EuO Films

Core to this study are the valence band intensities of Eu_{0.96}Gd_{0.04}O through the $4d$ to $4f$ super Coster-Kronig photoemission resonance. The valence band photoemission features for both EuO and Eu_{0.96}Gd_{0.04}O contain a number of shake up features [23], so that off resonance, at photon energies well away from a Eu or Gd $4d$ core level binding energy, the spectra for both the doped and undoped samples are similar, as seen in [Figure 6.2.1](#).

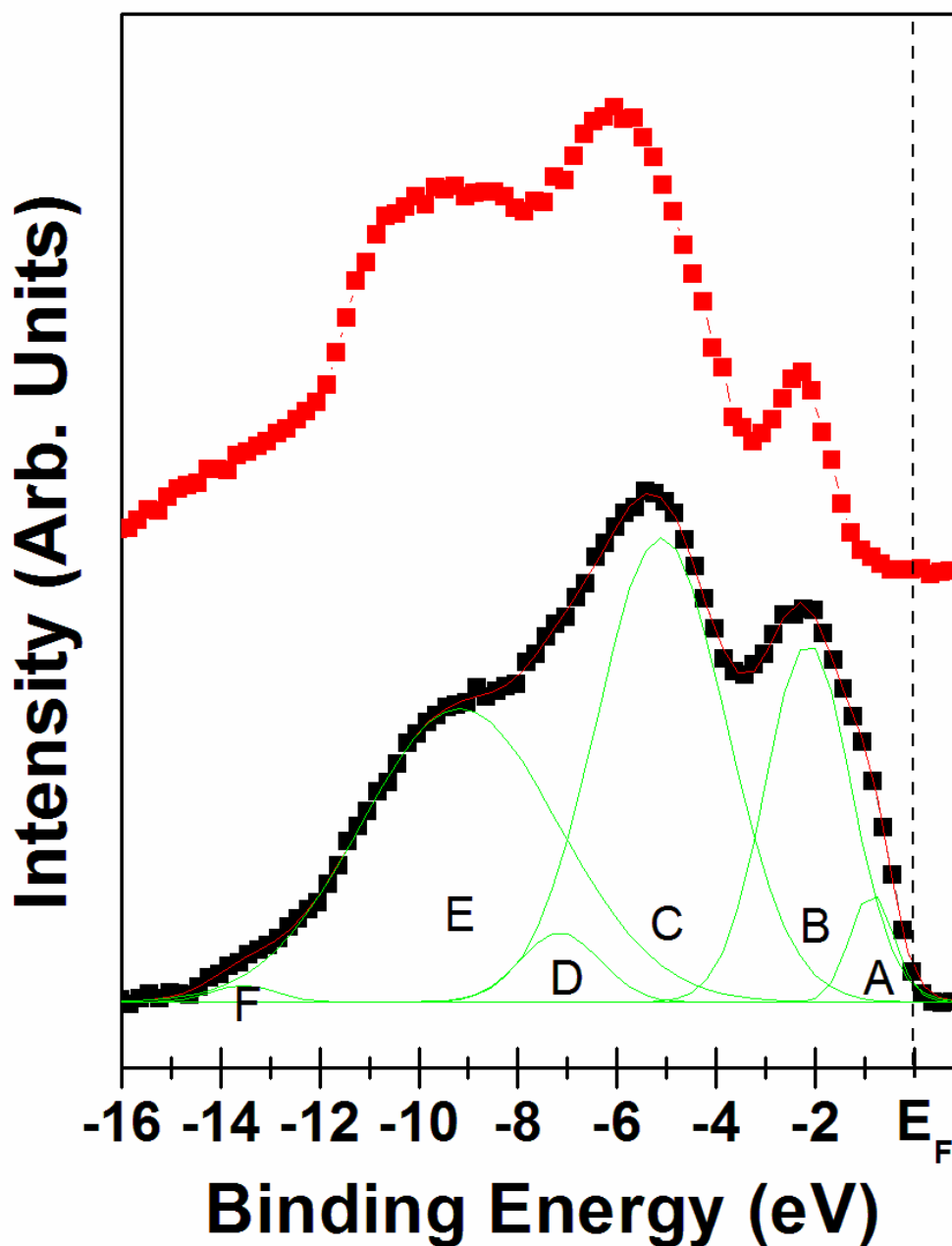


Figure 6.2.1 Valence band spectra obtained from the photoemission density of state for (a) EuO and (b) $\text{Eu}_{0.96}\text{Gd}_{0.04}\text{O}$ films grown on p-type Si (100). The composition of the spectra was determined by the Gaussian distributions and the photoemission feature were classified as arising from largely the (A) Eu $4d_{5/2}$ and electron pockets of the conduction band minimum, (B) Eu $4d_{3/2}$ (C) O $2s$, (D) O $2s$ and (E) Gd $4f$ and Eu $4f$ final state (satellite) contributions. Photoelectrons were collected along the surface normal. Measurements for both films were taken using synchrotron light with photon energy of 60 eV and incidence angle of 45° . Binding energy is denoted in terms of $E-E_F$.

Contributions corresponding to the Eu 4f final states in EuO are observed at a binding energy of -2.3 eV followed by a strong weighted O 2p features -4 to -6 eV, consistent with GW calculations [24]. The broad unresolved photoemission feature located at -7 eV to -11 eV stem from a variety of configurations of the final state excited state and Eu 4f satellite features [24, 25].

The inclusion of small amounts of gadolinium in the EuO lattice have little effect in the valence band structure, but changes near the Fermi level are also observed as suggested by the increase in the photoemission density of states. Increases in the photoemission density of states near the Fermi level in the doped films have been observed and are attributable to an increase in metallicity as demonstrated by mapping the electronic band structure near the Fermi level along both the crystallographic direction of the $\text{Eu}_{0.96}\text{Gd}_{0.04}\text{O}$ films and along the $\bar{\Gamma}\text{X}$ symmetry line in reciprocal space [24].

The contributions to the valence band region from the Gd 4f orbital in the valence band spectra are more transparent when the photon energies used corresponding to the 4d to 4f super Coster-Kronig photoemission resonance, as indicated in Figure 6.2.1 (a). The strongest enhancements in valence band region of the photoemission spectra occur in the photon energy range of 130 eV – 160 eV, but we find that the different photoemission features resonate at different photon energies (Figure 6.2.1 (b)), reflecting differences in the origin of their spectral weight.

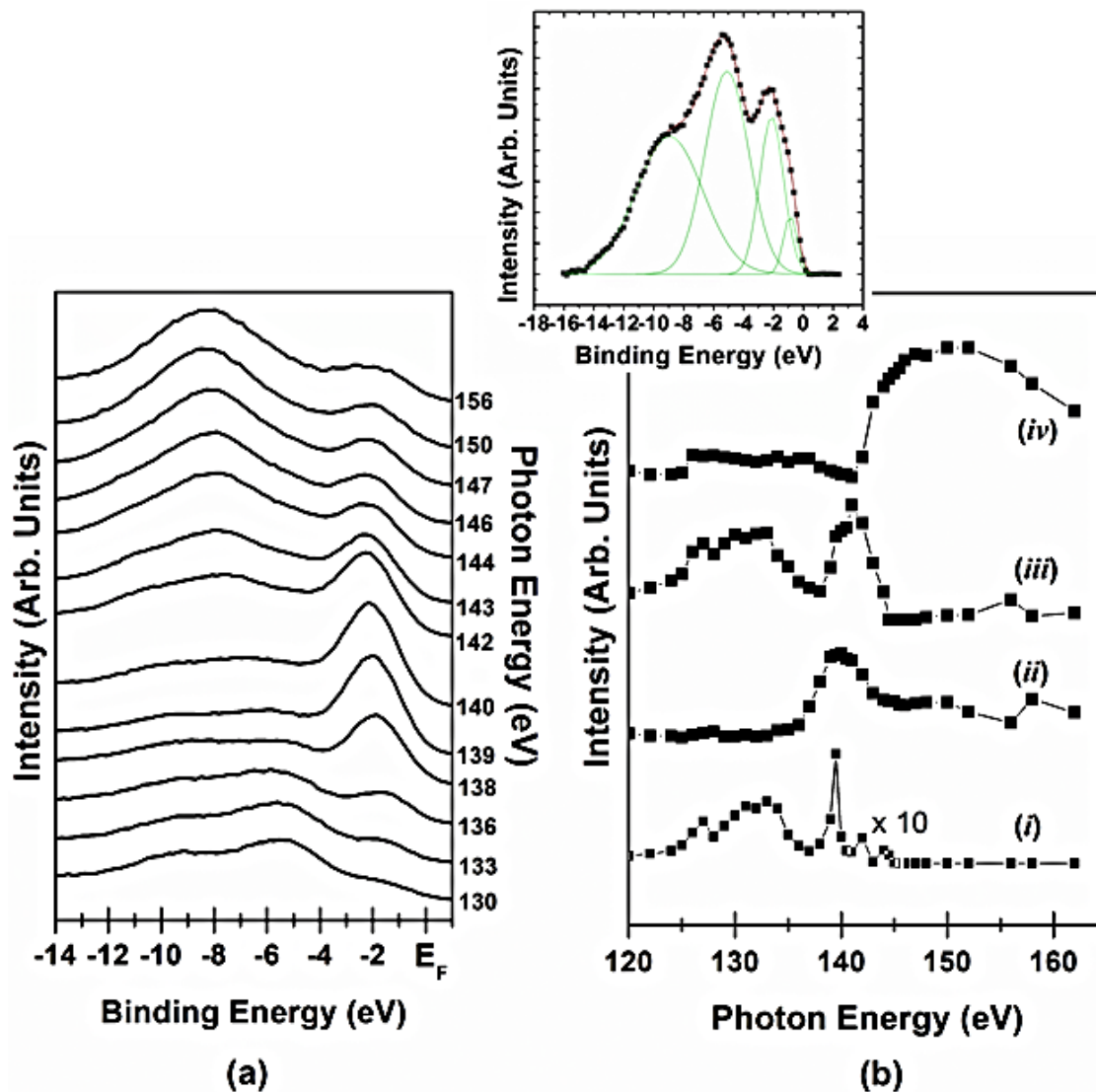
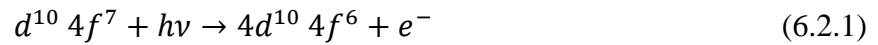


Figure 6.2.2 (a) The photoemission spectra for photon energies through the Gd and Eu 4d to 4f super koster Kronig photoemission resonance for $\text{Eu}_{0.96}\text{Gd}_{0.04}\text{O}$ films. (b) The resonant photoemission intensities, as a function of photon energy i.e. constant initial state spectra, for the valence feature at (i) 0.5 eV, (ii) 2.3 eV, (iii) 6.1 eV and (iv) 9.2 eV below the Fermi level. Light was incident at 45° . Photoelectrons were collected along the surface normal. Binding energy is denoted in terms of $E-E_F$.

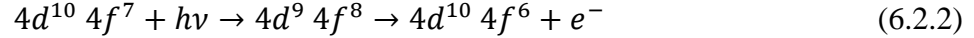
Because of the multi-configurational final states originating from EuO itself, a unique assignment of one feature to Gd alone is difficult, but we expect that the Gd 4f spectral

weight should be largely located in the region of -9 eV binding energy [10-16, 23], as discussed below.

The traditional $4d_{5/2}$ and $4d_{3/2}$ enhancements originating from the Eu $4f^6$ final state configuration are observed in the features near the Fermi level (i, in Figure 6.2.2 (b)) and at about -6 eV photon energy (iii, in Figure 6.2.2 (b)), in Figure 6.2.2 (b). Excitations involving a final state $4f^6$ are also evident as shown by (ii). In this case, the resonant process is described by resonant process that includes direct photoionization:



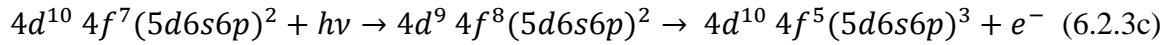
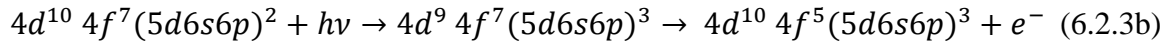
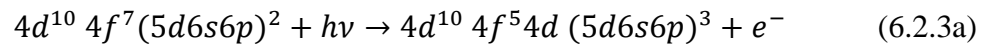
and a super Coster-Kronig transition of the form:



which result in the same final state. The resonant enhancement, seen in Figure 6.2.2, of the feature at about -6 eV binding energy (iii) at photon energies of 130 and 140 eV suggest strong hybridization of the europium atoms with oxygen. At photon energies near 130 eV, one expect contributions from the Eu $4d_{5/2}$ to dominate and no oxygen photoemission resonances occur near this photon energy. This enhancement provides a clear indication of the strong hybridization between the Eu $5d6s$ and oxygen $2p$ contributions.

Resonant enhancements of the feature at a binding energy of about -9.2 eV (iv, in Figure 6.2.2) occur at a photon energies close to the core threshold binding energy of the Gd $4d_{3/2}$ shallow core (about 147 eV), also as a result of a $4f^6$ final state, as again

dominated by excitations (equation 6.2.1) and (equation 6.2.2). This too leads to the classic Fano resonances seen in [Figure 6.2.2b](#) (iv). This feature in the region of -9 eV binding energy is not purely Gd in weight though, as seen in [Figure 6.2.1](#) and discussed above. Unlike the other semiconductors studied here contributions from Eu $4f^5$ final states are expected at similar binding energies (approximately -9 eV) via different excitation and decay channels [26]. In fact excitations of the form



are expected to contribute to the Fano-resonance seen ([Figure 6.2.2](#)) for the $\text{Eu}_{0.96}\text{Gd}_{0.04}\text{O}$ photoemission feature at -9.2 eV (iv), i.e. the multiconfigurational final state. The contributions from the various multiconfigurational final states is what provides the large width, in photon energy, of the resonance lineshape ([Figure 6.2.2 \(b\)](#) (iv)).

6.3 Comparing the Gd 4d to 4f Photoemission Resonance for Gd in various Host Semiconductors

In fact, in spite of the complications that arise from the Eu 4d→4f contributions to the Gd 4d→4f super Coster Kronig transition in the resonant photoemission processes for $\text{Eu}_{0.96}\text{Gd}_{0.04}\text{O}$, in fact the Gd 4d→4f transition resonance for $\text{Eu}_{0.96}\text{Gd}_{0.04}\text{O}$ is similar to that seen in $\text{Gd}_{0.03}\text{Ga}_{0.97}\text{N}$ and $\text{Gd}_{0.03}\text{Hf}_{0.97}\text{O}_2$. [Figure 6.3.1](#) show the valence band photoemission spectra for $\text{Eu}_{0.96}\text{Gd}_{0.04}\text{O}$, $\text{Gd}_{0.03}\text{Ga}_{0.97}\text{N}$, $\text{Gd}_{0.03}\text{Hf}_{0.97}\text{O}_2$ at the Gd 4d→4f photoemission resonance (“on” with $h\nu = 147$ eV) and away from the photoemission resonance (“off” with $h\nu = 140, 139.7$ and 132 eV for $\text{Eu}_{0.96}\text{Gd}_{0.04}\text{O}$, $\text{Gd}_{0.03}\text{Ga}_{0.97}\text{N}$, $\text{Gd}_{0.03}\text{Hf}_{0.97}\text{O}_2$ respectively). As expected [22-28], there is a big enhance of the photoemission in intensity at the Gd 4d→4f photoemission resonance (i.e. “on” resonance at $h\nu = 147$ eV), in the region of the Gd 4f binding energy at 8-20 eV below the Fermi level in the valence band photoemission spectra for $\text{Eu}_{0.96}\text{Gd}_{0.04}\text{O}$, $\text{Gd}_{0.03}\text{Ga}_{0.97}\text{N}$, $\text{Gd}_{0.03}\text{Hf}_{0.97}\text{O}_2$ ([Figure 6.3.1](#)).

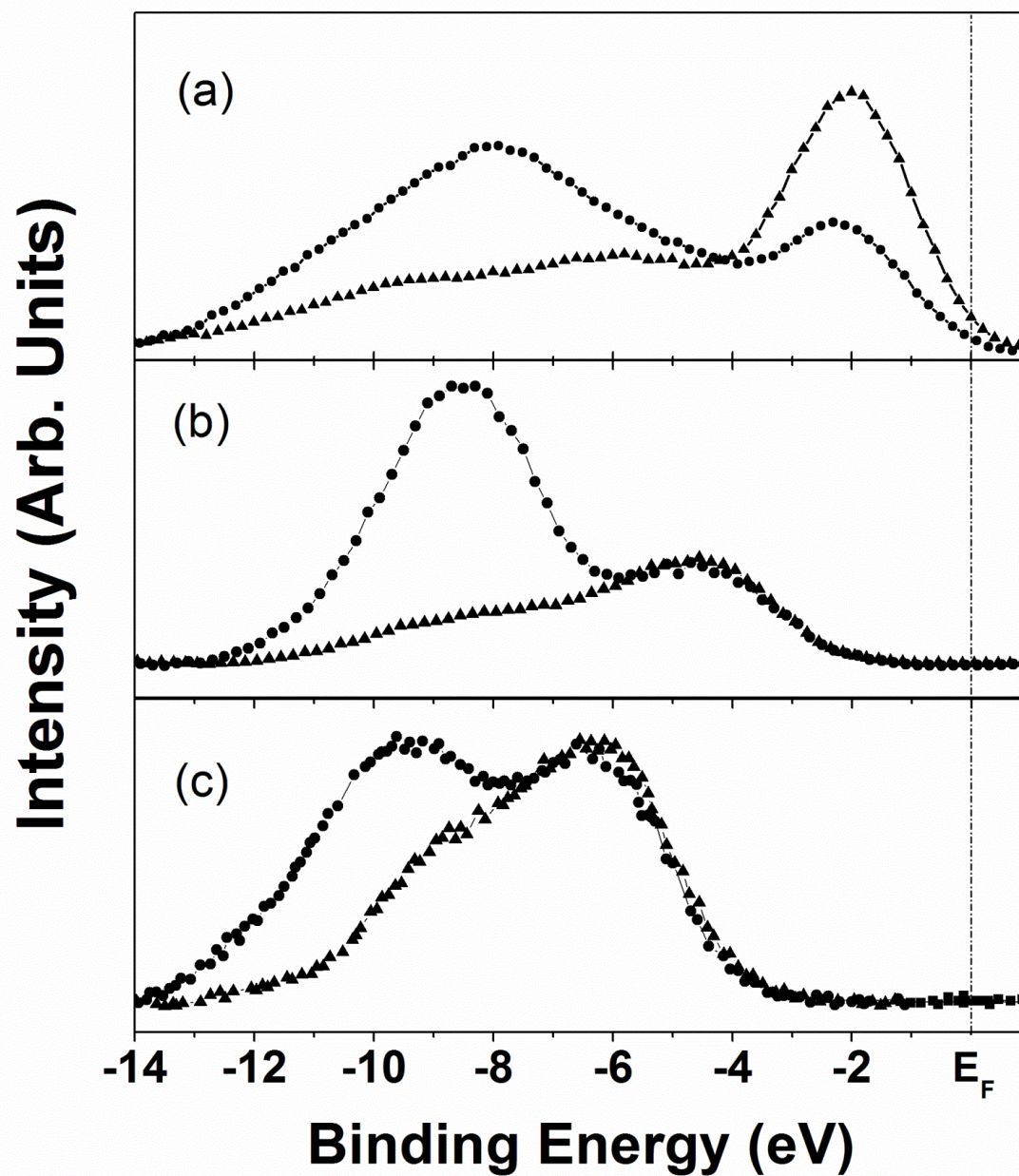


Figure 6.3.1 Valence band photoemission spectra “on” (photon energy of 147 eV) and “off” (photon energy of “off” with $h\nu = 140, 139.7$ and 132 eV for $\text{Eu}_{0.96}\text{Gd}_{0.04}\text{O}$, $\text{Gd}_{0.03}\text{Ga}_{0.97}\text{N}$, $\text{Gd}_{0.03}\text{Hf}_{0.97}\text{O}_2$ respectively) the Gd 4d to 4f resonant photoemission feature obtained for (a) $\text{Eu}_{0.96}\text{Gd}_{0.04}\text{O}$, (b) $\text{Gd}_{0.03}\text{Ga}_{0.97}\text{N}$ and (c) $\text{Gd}_{0.03}\text{Hf}_{0.97}\text{O}_2$. All photoelectrons were collected along the normal to the film surface. Binding energy is denoted in terms of $E - E_F$.

In the case of $\text{Gd}_{0.04}\text{Eu}_{0.96}\text{O}$, the Gd $4d \rightarrow 4f$ excitation results in the super Coster-Kronig transition and resonant photoemission (equation 3 and 4), the “on” versus “off” is much less pronounced than seen for $\text{Gd}_{0.03}\text{Ga}_{0.97}\text{N}$ and $\text{Gd}_{0.03}\text{Hf}_{0.97}\text{O}_2$, as visually seen in [Figure 6.3.2](#) and summarized in [Table 6.3.1](#).

Film	Peak Position (eV)	Width (eV)	On-Off Ratio
$\text{Gd}_{0.04}\text{Eu}_{0.96}\text{O}$	150.3	17.25	1.83
$\text{Gd}_{0.03}\text{Hf}_{0.97}\text{O}_2$	149.0	8.96	11.22
$\text{Gd}_{0.03}\text{Ga}_{0.97}\text{N}$	147.9	7.11	9.82

Table 6.3.1. Summary the photon energy for resonant photoemission intensity maximum, the width of the Gd $4d$ to $4f$ photoemission resonance, in photon energy and the intensity ration of “on” resonance at a photon energy of 147 eV to the “off” resonant intensity at a photon energy of eV.

This decrease in the resonant photoemission enhancement is seen to occur even though both Eu (equation 6.2.3) and Gd (equation 6.2.2) both contribute $\text{Gd}_{0.04}\text{Eu}_{0.96}\text{O}$, $4d \rightarrow 4f$ excitation resonant photoemission signal in the region of -9 eV binding energy. Thus without a doubt, $\text{Gd}_{0.04}\text{Eu}_{0.96}\text{O}$, is more metallic and better screened (more itinerant electrons) than either $\text{Gd}_{0.03}\text{Ga}_{0.97}\text{N}$ and $\text{Gd}_{0.03}\text{Hf}_{0.97}\text{O}_2$,

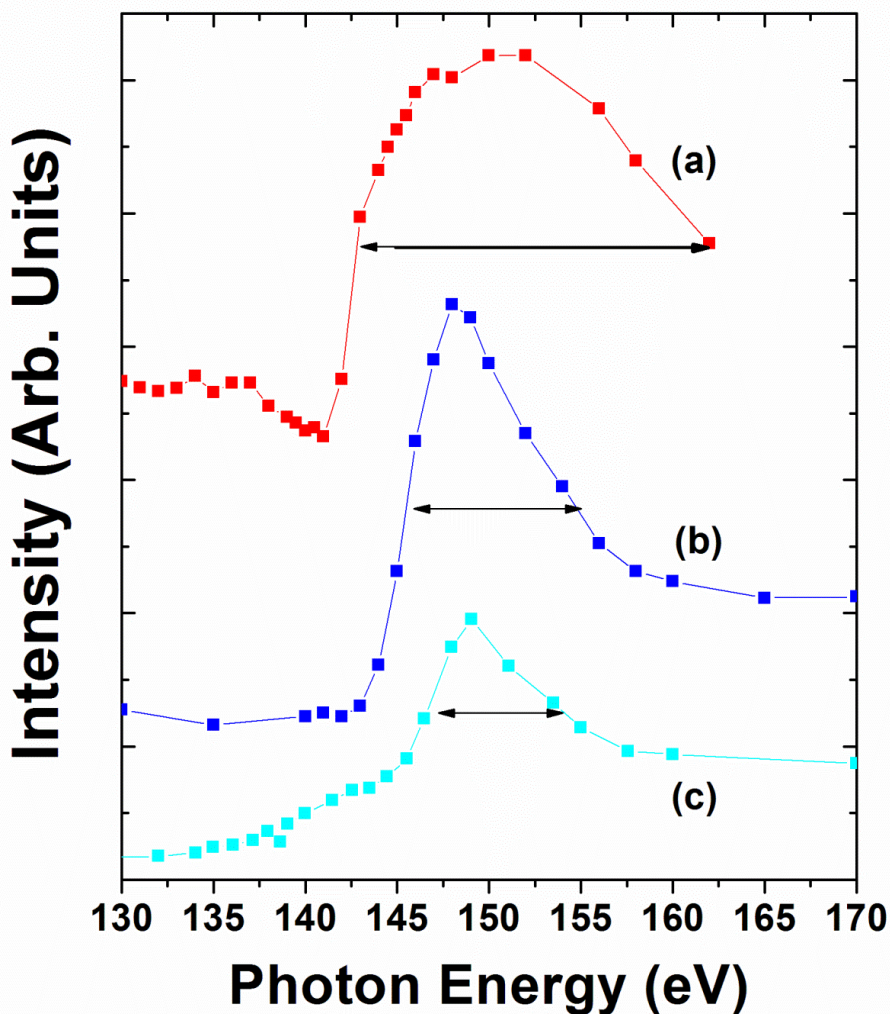


Figure 6.3.2 Constant initial state valence intensity as a function of photon energy in the region of Gd 4f contributions to the valence band (-9 eV binding energy, $E-E_F$) in Gd doped (a) GaN (3%), (b) HfO₂ (3%) and (c) EuO (4%) host systems.

6.4 Across the nonmetal to metal transition in Gd_{0.04}Eu_{0.96}O

Not only is the on-off ratio for the $4d \rightarrow 4f$ photoemission resonance much smaller for Gd_{0.04}Eu_{0.96}O, than for Gd_{0.03}Ga_{0.97}N and Gd_{0.03}Hf_{0.97}O₂, as visually seen in [Figure 6.3.1](#), we can also compare EuO and Gd_{0.04}Eu_{0.96}O $4d \rightarrow 4f$ excitation resonant

photoemission signal in the region of -2 eV binding energy, as seen in Figure 6.4.1. This resonant enhancement, as noted above, is almost entirely attributable to just the Eu 4d to 4f excitation and the valence band spectral weight is largely due to the Eu 4f [24, 25]. As with the comparison of the Gd 4d→4f photoemission resonance for $\text{Gd}_{0.04}\text{Eu}_{0.96}\text{O}$ versus $\text{Gd}_{0.03}\text{Ga}_{0.97}\text{N}$ and $\text{Gd}_{0.03}\text{Hf}_{0.97}\text{O}_2$, where $\text{Gd}_{0.04}\text{Eu}_{0.96}\text{O}$ differs significantly and has a far reduced photoemission resonance, $\text{Gd}_{0.04}\text{Eu}_{0.96}\text{O}$ also has a much reduced Eu 4d→4f photoemission resonance compared to EuO. This effect is consistent with our view of the metal to non-metal transition with increasing Gd concentration.

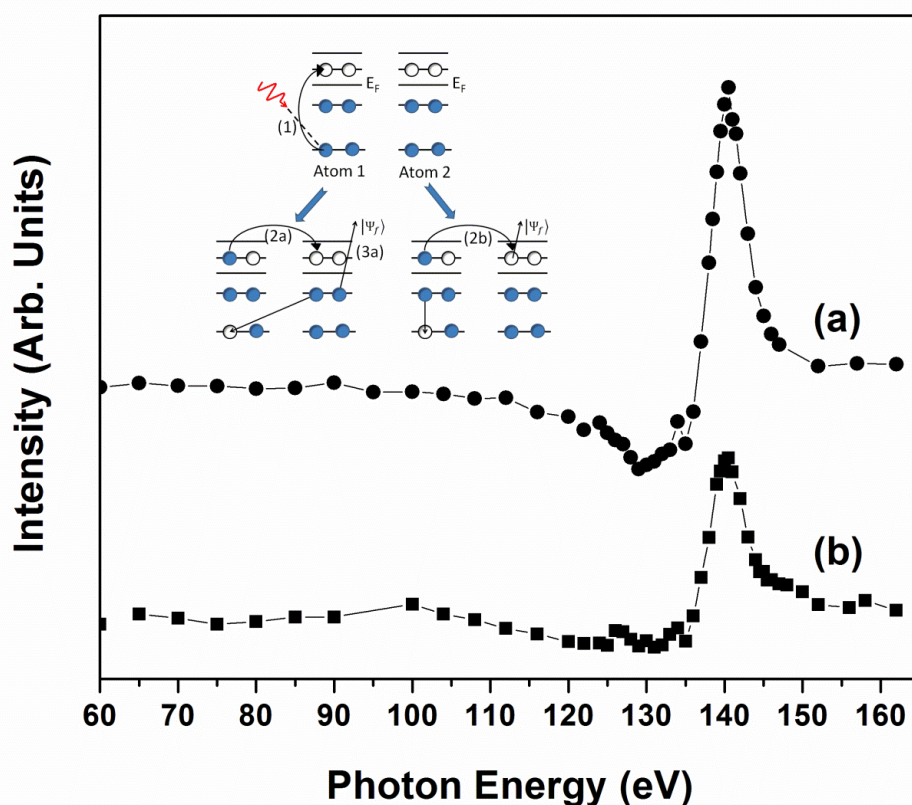


Figure 6.4.1 Resonant photoemission intensity as a function of photon energy for the Eu 4f weighted features in the valence band at about -2 eV binding energy ($E-E_F$) in (a) EuO and (b) $\text{Eu}_{0.96}\text{Gd}_{0.04}\text{O}$ films. The decrease in intensity suggests a major change in metallicity with the inclusion of 4% percent Gd.

References

- [1] D. Li, J. Zhang, S. Lee, P.A. Dowben, “Evidence for the formation of metallic mercury overlayers on Si(111)”, *Phys. Rev. B* 45 11876 (1992)
- [2] N.K. Singh, P. Dale, D. Bullett, R.G. Jones, “Mercury adsorption on Ni(111): III. Surface electronic structure”, *Surf. Sci.* 294 333 (1994)
- [3] J. Zhang, D.N. McIlroy, P.A. Dowben, S.-H. Liou, S.F. Sabiryanov and S.S. Jaswal, “The Valence-band Structure of $\text{La}_{1-x}\text{Ca}_x\text{MnO}_3$ ”, *Solid State Commun.* 97 39-44 (1996)
- [4] N.F. Mott, “Metal-insulator Transition”, *Rev. Mod. Phys.* 40, 677–683 (1968)
- [5] L.A. Turkevich, M.H. Cohen, “Is Expanded Fluid Mercury a Ferroelectric Excitonic Insulator?”, *Phys. Rev. Lett.* 53 2323 (1984)
- [6] L.A. Turkevich, M.H. Cohen, *J. Non-Cryst. Solids* 61±62 13 (1984)
- [7] P.A. Dowben, D. LaGraffe, “Coverage dependent changes in the barium overlayer electronic structure on Ni(111)”, *Phys. Lett. A* 144 193 (1990)
- [8] P.A. Dowben, D. LaGraffe, D. Li, G. Vidali, L. Zhang, L. Döttl, M. Onellion, “Probing the metal-nonmetal transition in thin metal overlayers using resonant photoemission”, *Phys. Rev. B* 43 10677 (1991)
- [9] G.J. Lapeyre, J. Anderson, P.L. Gobby, J.A. Knapp, “Photoemission Final-State Spectroscopy Applied to KClf”, *Phys. Rev. Lett.* 33 1290 (1974)
- [10] J. Shi, M. V. S. Chandrashekar, J. Reiherzer, W. Schaff, J. Lu, F. Disalvo, and M. G. Spencer, “High intensity red emission from Eu doped GaN powders”, *Phys. Status Solidi C* 5, 1495 (2008)
- [11] T. Thomas, X. M. Guo, M. V. S. Chandrashekar, C. B. Poitras, W. Shaff, M. Dreibelbis, J. Reiherzer, K. W. Li, F. J. DiSalvo, M. Lipson, and M. G. Spencer, “Purification and mechanical nanosizing of Eu-doped GaN”, *J. Cryst. Growth* 311, 4402-4407 (2009)
- [12] A.J. Steckl, J.H. Park, and J.M. Zavada, “Prospects for rare earth doped GaN lasers on Si” *Mater. Today* 10, 20-27 (2007)
- [13] G. H. Dieke and H. M. Crosswhite, “The Spectra of the Doubly and Triply Ionized Rare Earths”, *Appl. Optics* 2, 675-686 (1963)
- [14] S.R. McHale, J.W. McClory, J.C. Petrosky, J. Wu, R. Palai, Ya.B. Losovyj, and P.A. Dowben, “Resonant photoemission of rare earth doped GaN thin films”, *European Physical Journal: Applied Physics* 56 11301 (2011)

- [15] L. Wang, W.-N. Mei, S. R. McHale, J. W. McClory, J. C. Petrosky, J. Wu, R. Palai, Ya. B. Losovyj, and P. A. Dowben, submitted to the Journal of Alloys and Compounds
- [16] I. Ketsman, Ya. B. Losovyj, A. Sokolov, J. Tang, Z. Wang, K.D. Belashchenko and P.A. Dowben, "Resonant photoemission of rare earth doped GaN thin films", Appl. Phys. A: Mater. Sci. Process. 89 489-492 (2007)
- [17] J. Zhang, D.N. McIlroy and P.A. Dowben, "Changes in the Electron Effective Mass across the Nonmetal-Metal Transition in Magnesium Overlayers", EuroPhys. Lett. 29 469-474 (1995)
- [18] J. Zhang, D.N. McIlroy, and P.A. Dowben, "Correlation between screening and electron effective mass across the nonmetal-metal transition in ultrathin films", Phys. Rev. B 52 11380-11386 (1995)
- [19] D.N. McIlroy, J. Zhang, S.-H. Liou and P.A. Dowben, "Changes in screening and electron density across the coupled metallic-magnetic phase transition of La_{1-x}Ca_xMnO₃", Phys. Lett. A 207 367-373 (1995)
- [20] D.N. McIlroy, C. Waldfried, J. Zhang, J.W. Choi, F. Foong, S.H. Liou, P.A. Dowben, "Comparison of the temperature-dependent electronic structure of the perovskites La_{0.65}A_{0.35}MnO₃ A5Ca,Ba.", Phys. Rev. B 54 17438 (1996)
- [21] B.W. Chung, A.J. Schwartz, B.B. Ebbinghaus, M.J. Fluss, J.J. Haslam, K.J.M. Blobaum, J.G. Tobin, "Spectroscopic Signature of Aging in α -Pu(Ga)", J. Phys. Soc. Japan 75, 054710 (2006)
- [22] N. Wu, D. LaGraffe, I.N. Yakovkin, P.A. Dowben, "Localization and screening in GdNi alloy films", Phys. Status Solidi B, 248 1253–1257 (2011)
- [23] J. A. Colón Santana, J. M. An, Ning Wu, K. Belashchenko, X. Wang, P. Liu, J. Tang, Ya. Losovyj, I.N. Yakovkin, and P.A. Dowben, "Effect of gadolinium doping on the electronic band structure of europium oxide", Phys. Rev. B 85 014406 (2012)
- [24] J. M. An, S. V. Barabash, V. Ozolins, M. van Schilfgaarde, and K. D. Belashchenko, "First-principles study of phase stability of Gd-doped EuO and EuS", Phys. Rev. B 83, 064105 (2011)
- [25] W.D. Schneider, C. Laubschat, G. Kalkowski, J. Haase, A. Puschmann, "Surface effects in Eu intermetallics: A resonant photoemission study", Phys. Rev. B 28, 2017 (1983)

Chapter 7

Gd doped HfO₂ as a Neutron Detector

What instrument you would use to detect an atomic bomb? "A screwdriver," he quipped.

(Oppenheimer response in a closed congressional hearing room in 1946)

Although most of the focus throughout this work was on constructing devices with magnetic properties, the applicability of these devices can be extended to other type of devices such as neutron detectors. This chapter provides evidence of neutron capture detection using Gd:HfO₂ / p-type silicon devices. One must keep in mind that these results are still in an early stage of development, although these results are promising, refinement of the devices are still needed to make it competitive with the current detection technology.

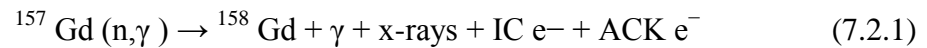
7.1 Why Building Neutron Detectors?

There is now a large demand and an increase in usage of radiation detection technologies for applications in homeland security, nonproliferation, and national defense. Significant advances have been achieved in radiation-detectors technology over the last decade, but still, nuclear radiation detection remains one of the most troublesome homeland security challenges. Indeed, this has long been recognized as major challenge: when Robert Oppenheimer was asked in a senate hearing, what instrument he would use to detect an atomic bomb. "A screwdriver," he replied, meaning you have to open every suitcase coming in to the country. The need for neutron detectors with higher efficiency and sensitivity play a huge role at the national defense level as well as in medical applications, as the current radiation detection technology is limited by several issues (such as distances between the nuclear material and detectors, background gamma rays and neutrons produce by cosmic rays, etc). Gammas and neutrons from cosmic rays tend to compete (even dominate) with the signal emitted from the nuclear material causing difficulties in the detection process. As a result, there has been a great demand for the development of next generation radiation detection materials with much better signal discrimination.

7.2 Neutron detection via Auger Electrons

The measurement of the K-shell Auger electrons in large Z elements is a challenge. These Auger electron lines fall well above 10 keV and as a result such experimental measurements are very rare or non-existent [1, 2]. Recent advances in the development of wide band gap rare-earth oxide semiconductor heterojunctions formed

with silicon [3–6] provide a new route to measurement of the K-shell Auger electron spectra, particularly in the case of gadolinium. Natural Gd has a thermal neutron capture cross-section of 46 000 barns, including a 15.65% abundance of the ^{157}Gd isotope with a thermal neutron capture cross-section of 255 000 barns [7–13]. The latter ^{157}Gd isotope cross-section neutron capture is over 60 times larger than the $^{10}\text{B}(n,\alpha)^7\text{Li}$ reaction. The Gd cross-section remains significantly higher than the thermal neutron capture cross-section of 10 B out to neutron energies of 200 meV. The absorption of the neutron leaves the ^{158}Gd in an excited state that releases energy through emission of high-energy gamma rays, low-energy gamma rays, x-rays, internal (IC) and Auger Coster–Kronig (ACK) conversion electrons as



with more detailed decay processes [12, 13], summarized schematically in [Figure 7.2.1](#). A similar result occurs with the neutron capture process $^{155}\text{Gd}(n,\gamma) \rightarrow ^{156}\text{Gd}$. The ^{156}Gd conversion electron contributions have weaker intensities owing to the ~25% lower thermal neutron capture cross-section for ^{155}Gd [14–16]. A gadolinium-based semiconductor heterojunction, nonetheless, can produce pulses characteristic of the K-shell Auger electron resonances, following neutron capture [12, 13, 17], provided the full energy of the Auger electron generated pulse can be captured. The resulting Auger

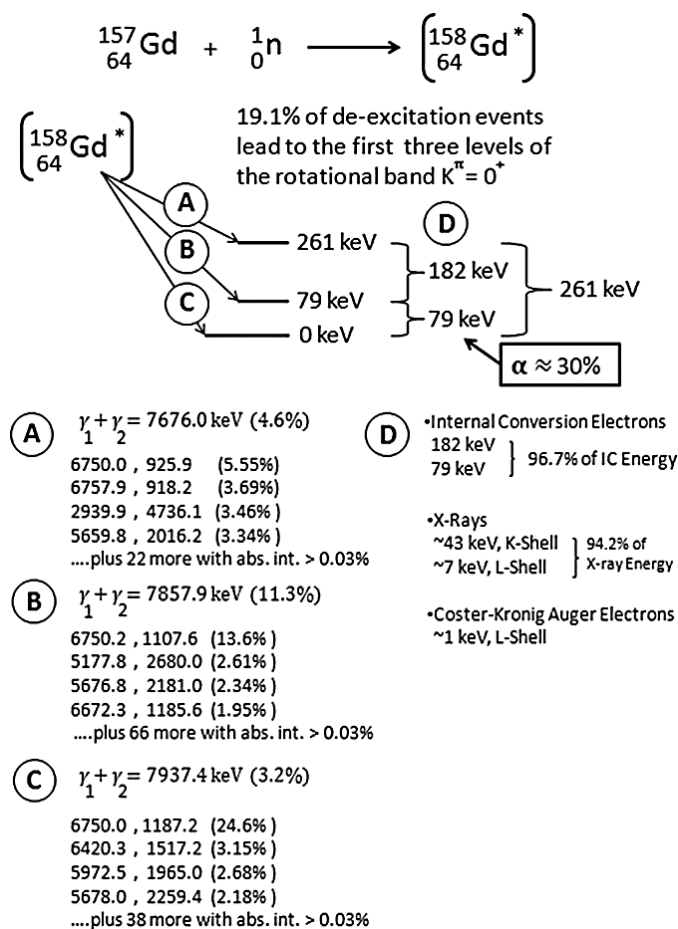


Figure 7.2.1. A summary of the major decay routes for ${}^{158}\text{Gd}$ in the excited state through emission of high energy gamma rays, low-energy gamma rays, x-rays, internal (IC) and Auger Coster–Kronig (ACK) conversion electrons as ${}^{157}\text{Gd}(n,\gamma) \rightarrow {}^{158}\text{Gd} + \gamma + \text{x-rays} + \text{IC } e^- + \text{ACK } e^-$, adapted from [12, 13].

electron spectrum is a characteristic of the atomic electronic transitions that include a Gd 1s (K-shell) hole, and is therefore not sensitive to the neutron energy, so long as there is neutron capture (as in Figure 7.2.1).

By fabricating a thin layer of semiconducting gadolinium in a diode heterostructure with silicon, the pulse collection following Gd neutron capture should produce a pulse height spectrum with features that are attributable to the Gd K-shell Auger electron resonances. To enhance the identification of such features in the neutron capture pulse height spectra in such a device, it is advantageous to choose a p-type layer

gadolinium semiconductor with a wide band gap, to suppress any plasmon excitations. The choice of a thin p-type layer, the large band gap of hafnium oxide, and the absence of plasmon excitations adds to the extensive electron mean free path of a 10–50 keV Auger electron. $\text{Hf}_{0.85}\text{Gd}_{0.15}\text{O}_{1.92}$ is just such a gadolinium rich semiconducting material and forms excellent heterojunctions with n-type silicon [3, 4]. This material adopts the cubic (fluorite) phase, not the monoclinic phase seen with much lower levels of Gd [3].

7.3 Single neutron capture detection

The p-type $\text{Hf}_{0.85}\text{Gd}_{0.15}\text{O}_{1.93}$ films deposited on n-type single crystal Si (100) substrates, using PLD [3, 4], routinely demonstrate rectification or diode-like characteristics, as shown in [Figure 7.3.1](#). The actual diodes that were used in this work are constructed with slightly less than 100 nm $\text{Hf}_{0.85}\text{Gd}_{0.15}\text{O}_{1.93}$ films on n-type Si (100). The $\text{Hf}_{0.85}\text{Gd}_{0.15}\text{O}_{1.92}$ is not overcompensated by oxygen vacancies and does not form a rectifying diode on p-type silicon but does do so on n-type silicon demonstrate rectification or diode-like characteristics, as shown in [Chapter 5](#). The measured neutron detection efficiency found using a PuBe neutron source for $\text{Hf}_{0.85}\text{Gd}_{0.15}\text{O}_{1.92}$ on n-type Si (100) samples was 6×10^{-3} or about a factor 5 times smaller than expected for these devices. This relative efficiency estimate does not include all the possible considerations for noise and dark current charge rejection and the values may in fact be slightly better than we estimate. Incomplete charge collection in this thin film geometry may also contribute to the decrease in measured efficiencies. Such thin film devices are likely to be gamma blind to normally incident fissile or actinide

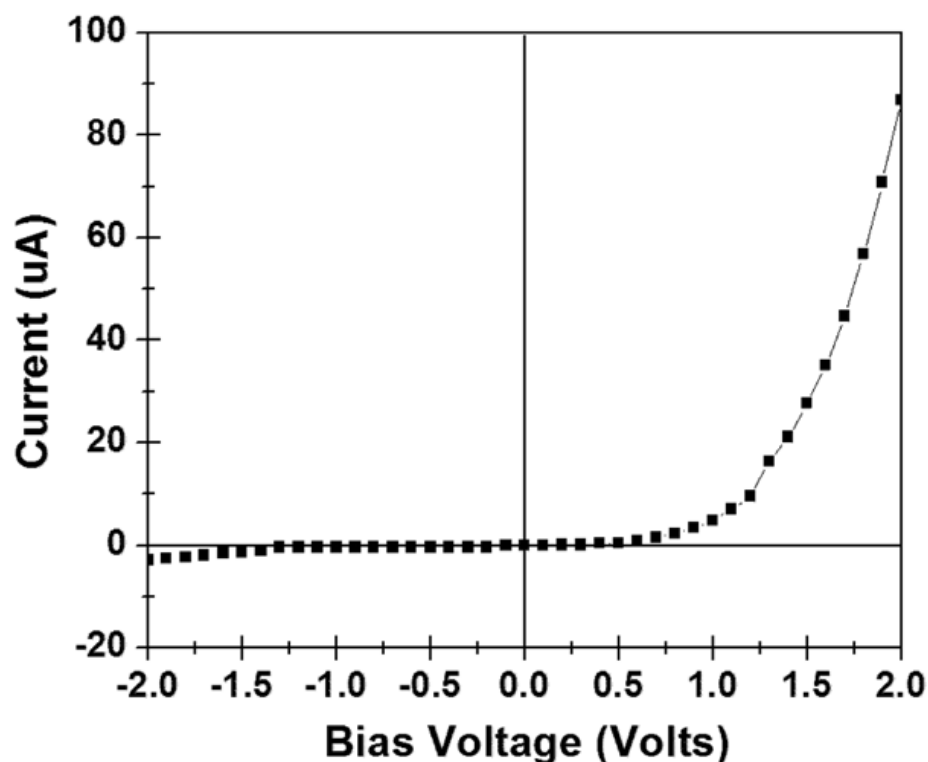


Figure 7.3.1 A heterojunction diodes constructed from $\text{Hf}_{0.85}\text{Gd}_{0.15}\text{O}_{1.92}$ on n-type silicon. The $\text{Hf}_{0.85}\text{Gd}_{0.15}\text{O}_{1.92}$ is not overcompensated by oxygen vacancies and does not form a rectifying diode on p-type silicon but does do so on n-type silicon.

material gamma radiation, because of the long attenuation length of gamma radiation (at energies of 1 MeV and above) compared to thermal and epithermal neutrons, but there is the distinct possibility that x-rays, caused by inelastic scattering processes in materials placed between the source and the detector, may cause K-shell Auger electron excitations in some devices as well [24]. Thus, we expect that the $\text{Hf}_{0.85}\text{Gd}_{0.15}\text{O}_{1.92}$ on n-type Si(100) heterojunction diodes neutron detectors (and similar structures) might reliably discriminate neutrons from gamma radiation emanating from fissile materials. In spite of the large Gd gamma absorption cross-section, the neutron capture cross-section is considerably greater. Consequently, there is a wide range of thicknesses where the Gd-doped film is opaque to neutrons and almost transparent to typical gamma rays, as is the

case of the heterojunction diodes studied here. For the devices we have measured, the high energy gammas have a mean free path much greater than the active region and can be ignored, not only on the basis of cross-section but because the experimental pulse height spectra (Figures 7.3.2 and Figure 7.3.3) are the characteristic of the expected electron energy spectrum [12] with multiple Gd atom electron scattering.

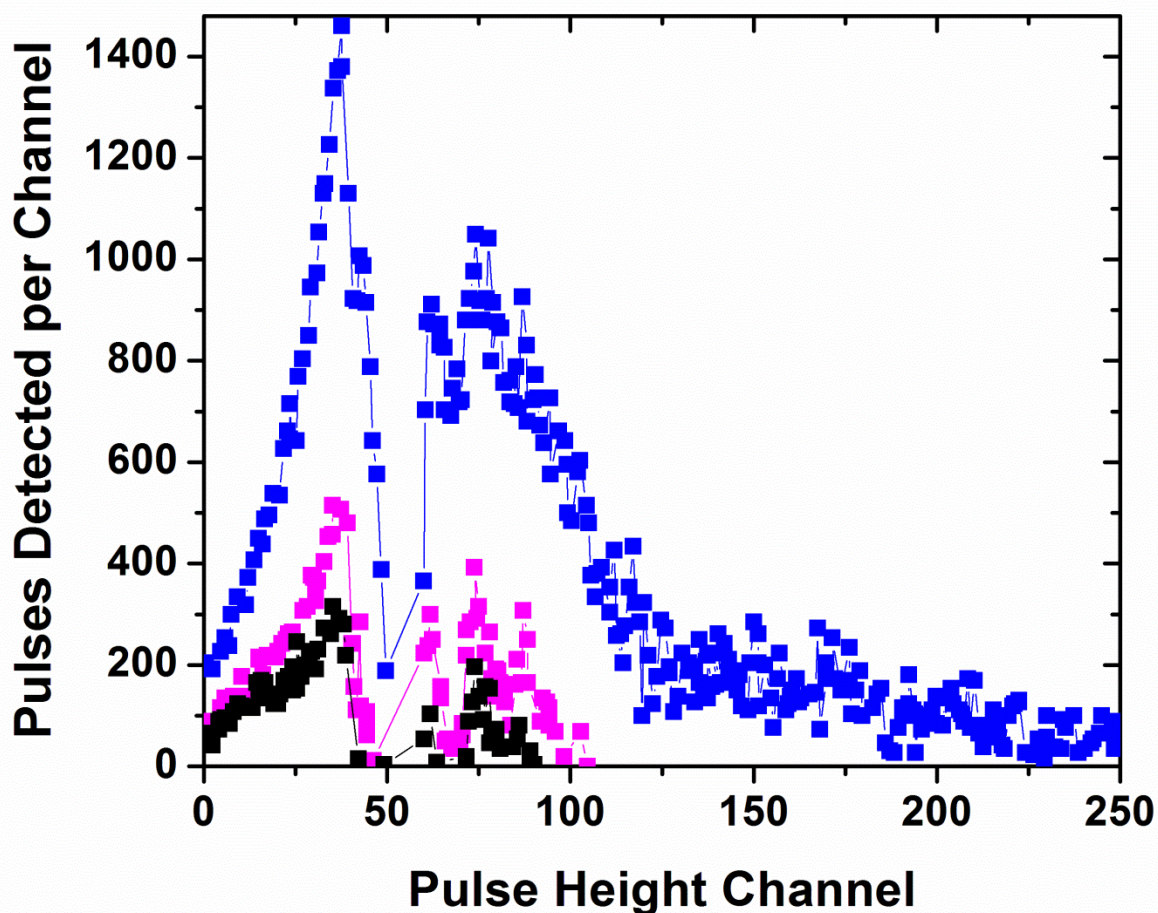


Figure 7.3.2 Pulse height spectra obtained using $\text{Hf}_{1-x}\text{Gd}_x\text{O}_{2-0.5x}$ combined contributions of Gd–O, and Gd–Hf single-scattering paths as well as several multiple-scattering (+MS) paths.

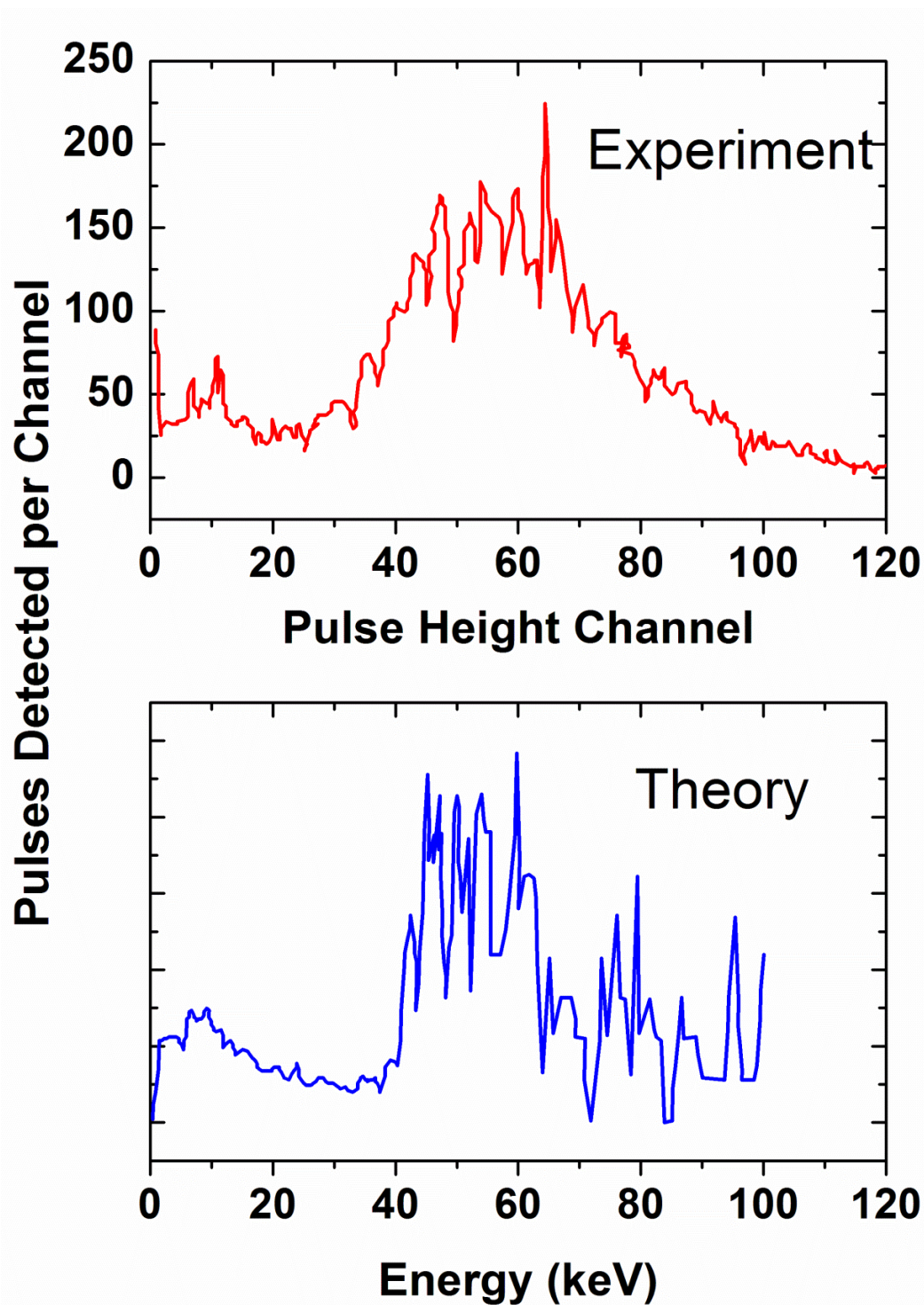


Figure 7.3.3. The pulse height spectra of $\text{Hf}_{0.85}\text{Gd}_{0.15}\text{O}_{1.92}$ on n-type Si(100) samples with thermalized neutrons from a PuBe source with a flux of $600 \text{ neutrons s}^{-1}$ incident on the diode, compared with an MCNP5.0 simulation, modified to account for suppression of the pulses of pulse height less than 200 mV in experiment.

The pulse train showed in [Figure 7.4.1](#) shows features that are thus solely due to neutron capture events. While the pulse rise time is less than 10 μs , the pulse decay time is 30 μs or more ([Figure 7.4.1](#)).

7.4 Fine Structure in the Neutron Capture Pulse Height Spectra

Experiments were carried out in both high and low neutron regimes. High neutron flux pulse height spectra experiments were carried out at the Ohio State University Research Reactor (OSURR) by the group of Professor James Petrosky and Professor John McClory. The OSURR is a pool type reactor for which the neutron flux is well characterized and is licensed to operate at continuously variable thermal power up to a maximum of 500 kW, and at maximum steady-state power, the average thermal neutron flux in the core is approximately $5 \times 10^{12} \text{ cm}^{-2} \text{ s}^{-1}$. The reactor is immersed in a pool of light water that provides full moderation and cooling by natural convective flow [25]. These experiments were conducted in the reactor horizontal beam port, which allows for direct access to the reactor neutron flux, while providing cable ports for making continuous in situ measurements. The reactor flux was further moderated by inserting a plastic plug between the reactor and the devices. For these OSURR experiments, the flux was varied so that the total thermal flux for 450 kW, 250 kW and 125 kW reactor powers was $2.57 \times 10^{12} \text{ cm}^{-2} \text{ s}^{-1}$, $1.48 \times 10^{12} \text{ cm}^{-2} \text{ s}^{-1}$ and $7.14 \times 10^{11} \text{ cm}^{-2} \text{ s}^{-1}$, respectively. Unlike in the PuBe experiments, described in the experimental section above, here the neutron detection instrumentation was standard analog pulse detection electronics. Because of the expected low pulse height from the 72 keV conversion electrons, low noise and good impedance matching were essential. A thermoelectrically cooled charge

sensitive preamp (Amptek A250CF CoolFET, 670 eV FWHM (Si)/~76 electrons RMS) was used for its low noise characteristics.

Because of the high neutron flux, these measurements were taken using $\text{Hf}_{1-x}\text{Gd}_x\text{O}_{2-0.5x}$ films ($x = 0.1$) deposited on n-type single crystal Si(100) substrates, samples with a lower concentration of Gd. [Figure 7.3.3](#) shows the results of neutron pulse counting detection for $\text{Hf}_{1-x}\text{Gd}_x\text{O}_{2-0.5x}$ films ($x = 0.1$) on the n-type single crystal Si(100) heterojunction diode. Between channel 50 and channel 100, there is clearly a fine structure in the pulse height spectra that is reproducibly observed. This fine structure is better resolved for pulse height spectra taken in the low flux regime. To better resolve this fine structure and aid in our electron energy assignment, the experiments were repeated in the extreme low flux regime using a PuBe source, with a data acquisition system with long integration times, as described in the experimental section.

The relatively low energy of the conversion electrons produced by ^{157}Gd (30–40 times less energetic than the daughter fragments of the ^{10}B nucleus) is the main drawback of using Gd as a neutron detector. This does not necessarily reduce detection efficiency, as long as the current pulses generated by 79.5 keV (and other) conversion electrons can be efficiently measured and reliably identified. Gd has a high internal conversion coefficient of nearly 39% for emitting a conversion electron. For ^{158}Gd formed following neutron capture, the K-shell binding energy is 50.2 keV with core ionization resulting in a variety of Auger electron resonances of decreasing kinetic energy, ending in the 29.3 keV conversion electron centered pulse residual [12, 13]. The L-shell transitions ($L_I = 8.3$, $L_{II} = 7.9$, and $L_{III} = 7.2$ keV) result in an ~7.2 keV Auger electron feature when averaged [12, 13, 16, 17]. The K-shell electron excitation is also accompanied by a 44 keV x-ray [12, 13, 16, 17], which in thicker films may result in

additional photoemission and Auger electron production. The M-shell binding energy is 1.8 keV, resulting in only a small reduction in the 79.5 keV conversion electron energy to about 77 keV. Again the $^{155}\text{Gd}(n,\gamma) \rightarrow ^{156}\text{Gd}$ transition is similar, with slightly higher resultant electron energies. This results in the creation of 33–80 keV pulses largely for $^{157}\text{Gd}(n,\gamma)$, but with a non-uniform distribution over this range [12, 13]. In the simulations of our devices, using the Monte Carlo N-Particle Transport Code (MCNP5.0), a planar source of 1011 neutrons was assumed and a model neutron spectrum calculated from 30 eV to 14 MeV, assuming natural abundance Gd in HfO_2 . The results follow expectation and prior studies [12, 13, 16, 17].

In fact, the expected non-uniform distribution of pulse heights is better observed in the experimental pulse height spectrum seen in [Figure 7.3.3](#). Following electronic suppression of pulses below 200 mV, which dominate the pulse height collection without electronic suppression (as indicated in [Figure 7.3.2](#)), the main contributions to the detection signal come from the conversion electron and the Gd K-shell Auger electron resonances. To better compare experiment with the model simulations, we made corrections at the low-energy end of the model pulse height spectra to account for the large number of counts rejected by electronic noise and signal suppression below a 200 mV pulse height in experiment. By incorporating these corrections to the model, there is considerable agreement between experimental and theoretical pulse height spectra. The deviations observed between simulation and experiment, at larger pulse heights, can be attributed to incomplete charge collection due to the fact that the $\text{Hf}_{0.85}\text{Gd}_{0.15}\text{O}_{1.92}$ film deposited on Si(100) is rather thin, although this heterojunction geometry does improve the pulse height resolution overall in experiment, particularly in the Gd K-shell Auger electron resonance region.

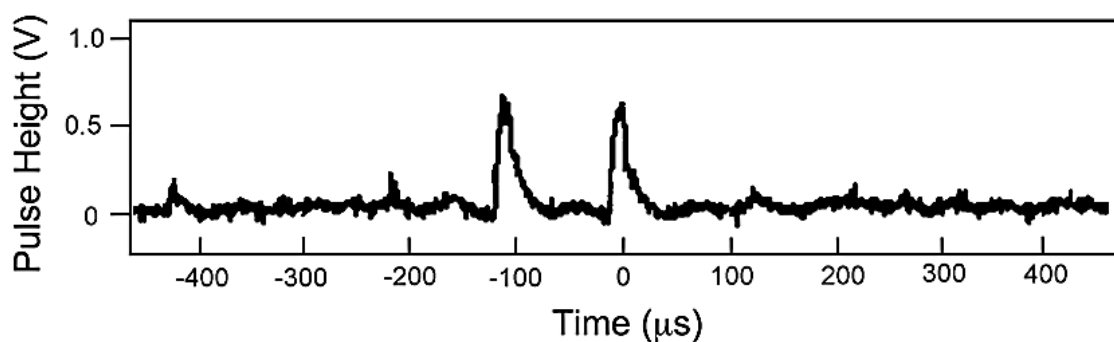


Figure 7.4.1. A sampling of a time domain pulse height spectra using $\text{Hf}_{0.85}\text{Gd}_{0.15}\text{O}_{1.92}$ on n-type Si(100) samples irradiated with thermalized neutron from a PuBe with a flux of $600\text{ neutrons cm}^{-2}\text{ s}^{-1}$. The offset of the baseline from 0 V is not meaningful, and a consequence of the display routine.

With thicker $\text{Hf}_{1-x}\text{Gd}_x\text{O}_{2-0.5x}$ films in the heterojunction structures, particularly with the lower Gd concentrations as in the $\text{Hf}_{0.9}\text{Gd}_{0.1}\text{O}_{1.95}$ films, the resulting devices exhibit inelastic loss increases. The result is that for the devices with these thicker $\text{Hf}_{1-x}\text{Gd}_x\text{O}_{2-0.5x}$ films in the heterojunction structure, there is a loss of the fine structure (as seen in [Figure 7.3.2](#) and [Figure 7.3.3](#)) in the pulse height spectra, leaving the expected ‘double bump’ pulse height spectra characteristic of other rare-earth (particularly Gd) based neutron detectors [26, 27]. From these results, it is clear that pulse counting will work with a gadolinium-containing semiconductor device, even though the pulses are some 20 or more times smaller than they would be in the case with ^{10}B capture. If further refinement of the heterojunction can improve the electron and hole collection efficiency equivalent to similar B capture related solid state devices, then the collection of the 79 keV electrons alone would result in a device that has an intrinsic efficiency similar to that of a boron-based semiconductor device or boron-based conversion layer device but with neutron capture and detection out to neutron kinetic energies 10–20 times that possible for boron semiconductor based devices.

The experimentally observed multiple Gd nuclear resonant decay channels and subsequent K-shell Auger electron resonances result in spectral features that align incredibly well with known energy spectra and support the premise that the $\text{Hf}_{0.85}\text{Gd}_{0.15}\text{O}_{1.92}$ film plays a key role not only in the neutron capture but also in the pulse height distribution. The optimization of both the materials and device structure is far from complete and the materials growth properties are not fully understood as yet, but successful solid state devices can be fabricated based on the concept.

References

- [1] Childs K D, Carlson B A, LaVanier L A, Moulder J F, Paul D F, Stickle W F and Watson D G 1995 Handbook of Auger Electron Spectroscopy 3rd edn, ed C L Hedberg (Eden Prairie, MN: Perkin Elmer Corporation, Physical Electronics Division)
- [2] CNRS on line data base at LaSurface.com:
<http://www.lasurface.com/database/elementaes.php>
- [3] Losovyj Ya B, Ketsman I, Sokolov A, Belashchenko K D, Dowben P A, Tang J and Wang Z , “The electronic structure change with Gd doping of HfO₂ on silicon”, 2007 Appl. Phys. Lett. 91 132908
- [4] Ketsman I, Losovyj Ya B, Sokolov A, Tang J, Wang Z, Natta M, Brand J I and Dowben P A , “Gd-doping of HfO₂”, 2008 Appl. Surf. Sci. 254 4308–12
- [5] Ketsman I, Losovyj Ya B, Sokolov A, Tang J, Wang Z, Belashchenko K D and Dowben P A , “The n-type Gd-doped HfO₂ to silicon heterojunction diode”, 2007 Appl. Phys. A 89 489
- [6] Ya.B. Losovyj, David Wooten, Juan Colón Santana, Joonhee Michael An, K.D. Belashchenko, N. Lozova, J Petrosky, A Sokolov, Jinke Tang, Wendong Wang, Navamoney Arulsamy and P.A. Dowben, “Comparison of n-type Gd₂O₃ and Gd-doped HfO₂”, J. Phys.: Condens. Matter 21 045602 (2009)
- [7] Gebauer B, Schulz Ch and Wilpert Th , “Novel large-area thermal neutron imaging detectors comprising and micro-strip gas detectors with low-pressure, two-stage amplification and delay line readout”, 1997 Nuc. Instrum. Methods Phys. Res. A 392 68
- [8] Miresghi A, Cho G, Drewery J S, Hong W S, Jing T, Lee H, Kaplan S N and Perez-Mendez V 1994, “High efficiency neutron sensitive amorphous silicon pixel detectors”, IEEE Trans. Nucl. Sci. 41 915
- [9] Garber D I and Kinsey R R 1976 BNL 325: Neutron Cross Sections vol 2, 3rd edn (Upton, NY: Brookhaven National Laboratory)

- [10] McLane V, Dunford C L and Rose P F 1988 Neutron Cross Sections vol 2 (San Diego, CA: Academic)
- [11] <http://atom.kaeri.re.kr/cgi-bin/endfform.pl>, Korea Atomic Energy Research Institute
- [12] Sakuri Y and Kobayashi T 2002 J. Nucl. Sci. Technol. (Suppl.) 2 1294
- [13] Ali M A, Khitrov V A, Sokhovoj A M and Vojnov A V 1994 "Properties of the ^{158}Gd compound state gamma-decay cascades", J. Phys. G: Nucl. Part. Phys. 20 1943–53
- [14] Shah K S, Cirignano L, Grazioso R, Klugerman M, Bennet P R, Gupta T K, Moses W W, Weber M J and Derenzo S E 2001: <http://breast.lbl.gov/~wwwinstr/publications/Papers/LBNL-50253.pdf>
- [15] Mughabghab S F 1981 Neutron Cross Sections vol 1 (New York: Academic)
- [16] Reeder P L 1994, "Thin GSO scintillator for neutron detection", Nucl. Instrum. Methods Phys. Res. A 353 134
- [17] Greenwood R C et al 1978 "Collective and two-quasiparticle states in ^{158}Gd observed through study of radiative neutron capture in ^{157}Gd " Nucl. Phys. A 304 327
- [18] Hayes T M and Boyce J B 1982 Solid State Physics ed H Ehrenreich et al (New York: Academic) vol 37 p 173
- [19] Schemm N, Balkır S and Hoffman M W 2008 IEEE Int. Symp. on Circuits and Systems (ISCAS) 2008(Seattle, WA, May 2008) pp 1866–9
- [20] Osberg K, Schemm N, Balkır S, Brand J, Hallbeck S, Dowben P and Hoffman M, "A Handheld Neutron-Detection Sensor System Utilizing a New Class of Boron Carbide Diode", 2006 IEEE Sensors J. 6 1531
- [21] Wang W, Hong Y, Yu M, Rout B, Glass G A and Tang J, "Structure and magnetic properties of pure and Gd-doped HfO₂ thin films", 2006 J. Appl. Phys. 99 08M117
- [22] Dole S L, Hunter O Jr and Calderwood F W 1980 "Elastic Properties of Stabilized HfO₂ Compositions", J. Am. Ceram. Soc. 63 136

- [23] Ushakov S V, Navrotsky A and Helean K B 2007, “Energetics of Defect Fluorite and Pyrochlore Phases in Lanthanum and Gadolinium Hafnates”, *J. Am. Ceram. Soc.* 90 1171
- [24] Young C, Colon Santana J, McClory J, Petrosky J, Brand J A and Molnar P in preparation
- [25] www-nrl.eng.ohio-state.edu/
- [26] Uozumi Y, Anami K, Nohtomi A, Sakae T and Matoba M 1997 *J. Nucl. Sci. Technol.* 34 80
- [27] Bell Z W et al 2005 “Neutron detection with cryogenics and semiconductor”, *Phys. Status Solidi c* 2 1592
- [28] Chung M F and Jenkins L H, “Auger electron energies of the outer shell electrons”, 1970 *Surf. Sci.* 22 479
- [29] Coghlan W A and Clausing R E , “Auger catalog calculated transition energies listed by energy and element ”, 1973 *At. Data* 5 317
- [30] Briggs D and Riviere J C 1983 *Practical Surface Analysis vol 1 Auger and X-ray Photoelectron Spectroscopy* 2nd edn (New York: Wiley)
- [31] Beardon J A and Burr A F 1967 *Rev. Mod. Phys.* 39 125

Chapter 8

Conclusions and Pending Future

“Now this is not the end. It is not even the beginning of the end. But it is, perhaps, the end of the beginning”

-Sir Winston Churchill -

8.1 What have we leaned?

Throughout this thesis I described the role of rare earth dopant in several high k -dielectric compounds materials. Cr-DLC and chromium carbide hydrogenated DLC alloys was introduced first as part of exemplary device that exhibit strong magnetoresistive effects. At low Cr content, the Cr dissolves in an amorphous DLC matrix forming an atomic-scale composite. At higher Cr content, Cr is present as nano-composite and chromium carbides precipitate. In the films of higher chromium concentration, a large coefficient of negative magnetoresistance was observed in heterojunction devices with n -type silicon as a substrate and the negative magnetoresistance of the I - V curve, which is ascribed to uncompensated spins at the surface of the antiferromagnetic chromium carbide clusters, indicated that the material might be suitable for spin-electronics applications.

The current success, device-wise, incorporated gadolinium and/or cerium dopants in dielectric films such as EuO and HfO₂ and made devices from heterojunctions with

silicon. Gd_2O_3 on silicon was also explored with the aim of obtaining similar effects. Interesting effects were introduced by the Gd doping in the HfO_2 compound and go beyond the simply change in structure, such as the structure goes from cubic to monoclinic with higher concentration of Gd dopant in HfO_2 . With increased Gd doping HfO_2 is seen to undergo an n-type to p-type crossover. The bulk conductivity nature was consistent with that of the surface as suggested by the device fabrication on both p-type and n-type silicon substrates. Although no magnetic properties were observed in these devices, the success in the construction of a heterojunction diode and the capability of gadolinium to detect neutrons led to the fabrication of several successful neutron detectors. Although the optimization of both the materials and device structure is far from complete and the materials growth properties are not fully understood as yet, solid state devices can be fabricated based on the concept.

Remarkable effects were also found on EuO films by the inclusion of Gd. With Gd inclusion at the level of 4%, changes in the texture orientation from (100) to (111) were observed, likely due to the availability of free carriers. This is supported by the observation of electron pockets filled under Gd doping, which confirmed the indirect character of the EuO band gap with the conduction-band minima at the X points, in agreement with GW calculations and prior data for Ce-doped EuO. The polar character of the (111) surface resulted in a significant band bending at the surface, which appears to depend on the degree of the surface overoxidation. In terms of devices, EuO resulted in a rectifying heterostructure with small magnetic dependence at low temperatures. However, the I-V curve obtained for the 4% doped films resulted in reminiscent of an Esaki diode behavior. This suggests the existence of a depletion region in the subsurface region, which is associated with this band bending.

There is a whole new future of designed semiconductors. Dielectrics turned into semiconductors and built into devices are just one of the few. What is of great advantage in this work is that all the materials are silicon compatible, which is valuable as silicon is still one of the most widely used semiconductors for technological applications. On the other hand, there is still a downside to the story, not all the materials that command attention are robust and stable (such as EuO) critical for the success of the application. Nonetheless, those that are stable and reliable; they may well be the future to a whole class of new devices.

8.2 What is next?

Several rectifying structure were presented throughout this study, but is not enough to just make a device that proves principle. The refinement of these devices is critical and one must implement a rigorous characterization; switching speed, device lifetime, device reliability, optimum dopant concentration, electrical mobility and reproducibility to name a few. Of key issue is the reliability of these materials in structures with reduce dimension. This kind of reduction in practice is well beyond the scope of this work and is a challenge in itself, but the emersion of a potential device must be part of the development.